RICE UNIVERSITY

Magnetic Confinement of an Ultracold Neutral Plasma

By

Grant Gorman

A THESIS SUBMITTED
IN PARTIAL FULFILLMENT OF THE
REQUIREMENTS FOR THE DEGREE

Doctor of Philosophy

APPROVED, THESIS COMMITTEE

Thomas Killian

Thomas Killian
Dean, Wiess School of Natural Sciences
E. Dell Butcher Professor in Physics and Astronomy

SJBradshaw
SJBradshaw (Apr 7, 2022 20:14 CDT)

Stephen Bradshaw
Associate Professor of Physics and Astronomy

Hanyu Zhu

Hanyu Zhu
Assistant Professor of Materials Science and NanoEngineering

HOUSTON, TEXAS
April 2022

ABSTRACT

Magnetic Confinement of an Ultracold Neutral Plasma

by

Grant Gorman

Ultracold neutral plasmas (UCNPs), created by the photoionization of a cold gas, have proven to be an excellent platform for studying plasmas in far more complex environments. Through their ultracold temperatures and dilute densities, UCNPs occupy an exotic regime of plasma physics where the Coulomb energy between neighboring ions exceeds the average thermal energy. Under such conditions of strong coupling, they display a rich assortment of physical phenomena in regimes that are challenging to model theoretically. The application of modern atomic physics techniques provides powerful diagnostics and a high level of control over the ion density, velocity, and internal-state distributions. This allows UCNPs to be sculpted in ways that induce and isolate a wide variety of phenomena, and makes these systems ideal for studies of fundamental plasma physics.

Over the last two decades, UCNPs have been on the forefront of experimental study of strongly coupled plasmas, however, recently there has been emerging interest in plasmas that are both magnetized and strongly coupled because the combined effects challenge our understanding of plasma equilibration and transport. Strong coupling introduces short-range spatial correlations between particles that invalidate closure schemes used to derive plasma kinetic equations, while strong magnetization frustrates the use of conventional collision operators because particle gyromotion

occurs on length scales relevant for collisions. In recent years, great progress has been made to develop kinetic theories that accurately describe plasmas in asymptotic regimes of either strong coupling or magnetization, but how these regimes merge is still an open question.

UCNPs occupy an interesting regime of density and temperature that makes them uniquely suited for the study of plasmas at the intersection of Coulomb coupling and magnetization. Despite this fact, rather few experiments have been conducted on UCNPs in external magnetic fields. This thesis describes the magnetic confinement of an ultracold neutral plasma created at the null of a biconic cusp (or quadrupole) magnetic field. This work utilized Doppler-sensitive laser-induced-fluorescence (LIF) images of the ions. LIF has long been used to probe the ions in UCNPs, but non-uniform magnetic fields complicate LIF due to the spatially varying Zeeman shifts and quantization axis of the ions. This thesis describes the development of a quantitative model of LIF imaging in a non-uniform magnetic field, which uses velocity-resolved rate equations to describe the transfer of ion population due to photon scatter and spontaneous emission. This probe also offers the new ability to measure the electron-spin polarization of the ions, which is inherited from the precursor atoms during photoionization, and should open new possibilities for studying plasma diffusion.

The magnetization and confinement of ultracold plasmas promises an open frontier for the UCNP research field. UCNPs confined within biconic cusp fields offer a platform for studying plasmas with changing length scales and dominant physical processes. Beyond fundamental interest, magnetic confinement should circumvent the limitations that the rapid plasma expansion imposes on laser cooling of the ions in a UCNP and magneto-optical forces should enhance plasma confinement, helping stretch the boundaries of Coulomb coupling strength available in UCNP experiments.

Acknowledgements

At the end of my journey through graduate school, I feel extremely grateful as I reflect on the many people that have supported me in both my personal and professional life. I have faced many challenges during my six years at Rice and without many of my friends, family, and colleagues I would not be where I am today.

I would like to start by thanking my advisor, Prof. Thomas Killian. Tom has taught me a great deal about scientific writing and managing research projects, but the thing that stands out most to me is how he taught me to think like a scientist - Tom has an uncanny ability to see through to the crux of an issue and find the optimal path forward. Most of all, however, I am grateful for how Tom has always supported me and challenged me to improve.

I would also like to thank all my fellow lab mates, both past and present. In particular, I would like to thank my lab partners Dr. Thomas Langin and MacKenzie Warrens. It was genuinely a pleasure to work alongside both of you in the plasma lab. Much of what I know about the experiment I learned from Thomas during my first few years at Rice. MacKenzie arrived a few years after myself and has been immensely helpful taking many of the measurements that were presented in this thesis.

I have been lucky to have made a very close group of friends while at Rice. To Brian Heckler, Magio Madjerec, and Nicholas Collett, thank you for the good times and solidarity. Lastly, I would like to thank my family. Mom and Dad, thank you for your unwavering love and support throughout all of my life. I can never repay you for all you have done for me. To my brother Zack, thank you for always being an inspiration; I am extremely proud of you for finishing your PhD and for bringing your lovely wife, Rachel, into our family.

Contents

Illustrations

Chapter 1

Introduction

Systems of charged particles, otherwise known as plasmas, are ubiquitous throughout the universe. Plasmas in nature tend to be hot because they are formed by the collisional ionization of neutral atoms or molecules, requiring temperatures $\sim 1\,\mathrm{eV}$ for collisions to be strong enough to liberate bound electrons. At lower temperatures, the plasma state is typically not stable because charged particles recombine into neutral atoms or molecules via a process called three-body recombination (TBR). However, ultracold neutral plasmas (UCNPs), formed in a laboratory by the photoionization of a cold gas [1], are an exception to these generalizations, and they are even colder than astrophysical plasmas formed in cold molecular clouds [2]. UCNPs occupy an exotic regime of plasma physics with ultracold ion temperatures $\sim 1\,\mathrm{K}$, tunable electron temperatures ranging from $1-1000\,\mathrm{K}$, and relatively dilute densities ranging from $10^6-10^{12}\,\mathrm{cm}^{-3}$ [3].

One important feature of UCNPs is that they are strongly coupled. The coupling strength of a plasma is characterized by the Coulomb coupling parameter, $\Gamma = E_c/k_BT$. A plasma is considered strongly coupled when the average Coulomb energy between neighboring ions ($E_c = e^2/4\pi\epsilon_0 a$, where $a = (3/4\pi n)^{1/3}$ is the average interparticle spacing) exceeds the average thermal energy (k_BT). In the strongly coupled regime, the microscopic collisional processes that determine macroscopic transport and equilibration are difficult to describe theoretically due to the development of strong, short-range correlations that are not captured by traditional plasma kinetic theory.

UCNPs have been on the forefront of experimental study of strongly coupled plasmas (SCPs) since their first experimental realization in 1999 [1] because of their well-controlled initial conditions and precise diagnostics. Most experiments to date have studied UCNPs in the absence of external magnetic fields. However, there has been emerging interest in magnetized and strongly coupled plasmas in general [4, 5, 6] and in the ultracold regime [5, 7, 8], driven in large part by new experimental capabilities in dusty [9, 10, 11] and laser-produced high-energy density (HEDP) plasmas [12, 13], but is also important in astrophysical systems such as white dwarf [14, 15] and neutron [16, 17] stars. The combined effects of magnetization and strong coupling modify collisional and transport phenomena in ways that are challenging to model theoretically [8, 18, 19], but recent developments suggest that a unified theory that bridges the gap between these two regimes is just over the horizon [20, 21].

The extension of the UCNP platform to probe plasmas in overlapping regimes of magnetization and strong coupling is important for the discovery of new phenomena and to aid the development of new theoretical and numerical models. This thesis describes our first efforts towards this end: the magnetic confinement of a UCNP created at the null of a biconic cusp (or quadrupole) magnetic field. The confinement was demonstrated using planar LIF images of the ions, which required the development of a quantitative model for LIF in the presence of non-uniform magnetic fields. An interesting byproduct of this model is the ability to measure the long-lived electron-spin polarization that the ions inherit from the precursor atoms, and this newfound ability should open new avenues for studying plasma flow and diffusion.

1.1 Ultracold Neutral Plasmas

UCNPs are formed by photoionizing a cold gas of atoms or molecules near the ionization threshold. They were first created in 1999 by photoionizing a laser-cooled gas of metastable Xe atoms in a magneto-optical trap (MOT) above threshold [1] and have subsequently been created this way using atomic gases of Rb [22, 23, 24], Ca [25], Yb [26], and Sr [27]. UCNPs have also been created by exciting atoms [28, 29, 30] or molecules [31] to highly excited Rydberg states that subsequently collisionally ionize into a plasma. For molecular UCNPs, the precursor cold gas is formed by seeding molecules in a supersonic molecular beam. In this thesis, we create UCNPs by singly ionizing a cold gas of laser-cooled, magnetically trapped ^{88}Sr atoms just above the ionization threshold using a 10-ns pulsed dye laser (to be discussed in more detail in Chap. 2).

Alkaline-earth atoms are well-suited for UCNP experiments because a single valence electron remains following photoionization, providing a relatively simple Alkali-like level structure with optically accessible electronic transitions. ^{88}Sr^{+} in particular lacks nuclear spin, so its level structure is further simplified by the absence of a hyperfine structure. The ability for the ions to interact with laser light forms the basis for the ability to laser cool the ions [32], diagnostics such as absorption [27] and fluorescence [33] imaging, and spin tagging techniques for studies of transport and equilibration [34].

The dynamics of ultracold plasmas following photoionization have been discussed in detail in review articles [3, 35] and theses [36, 37, 38]. The following discussion is intended to provide a brief overview of the important properties of UCNPs and their evolution. Immediately after photoionization, the electrons and ions inherit the density distribution (n) of the precursor atoms, which is typically either a spherically symmetric Gaussian distribution for atoms in a MOT [39] or an exponentially decaying distribution for atoms in a quadrupole magnetic trap [40]. The ions are created with extremely low kinetic energy, close to the temperature of the precursor atoms, but they possess significant excess electrical potential energy due to their initially uncorrelated state and undergo a process called disorder-induced heating (DIH) in the first few 100 ns, resulting in ion temperatures $T_i \sim 1\,\mathrm{K}$ [41]. Due to the extremely small electron-ion mass ratio (10^{-6}), essentially all of the excess photoionization energy is converted into electron thermal energy. Thus, the initial electron temperature (T_e) can be tuned with the wavelength of the photoionization laser and is typically set between $1 - 1000\,\mathrm{K}$, although there are external factors that limit the practical range for setting T_e. Lower electron temperatures are generally desired to ensure hydrodynamic conditions, higher plasma neutrality, and slower plasma expansion, but needs to be sufficiently high to avoid three-body recombination into neutral atoms.

TBR occurs when two electrons and an ion collide inelastically to form a Rydberg atom and an energetic electron, which carries away the Rydberg binding energy. This process results in depletion of the plasma density and heating of the electrons and occurs with rate

$$R_{TBR} = K_{TBR} n^2 T_e^{-9/2} = 7.28 \Gamma_e^{9/2} \omega_{pi}, \tag{1.1}$$

where $K_{TBR} = 2.77 \times 10^{-9}\,\mathrm{K}^{9/2}\mathrm{cm}^6\mathrm{s}^{-1}$ [42] and $\omega_{pi} = \sqrt{ne^2/m_i\epsilon_0}$ is the ion plasma oscillation frequency. Measurement of the TBR rate has been used as a probe of electron temperature in a UCNP previously [43], but three-body recombination is generally detrimental to UCNP experiments because the depletion can become prominent enough to limit the plasma lifetime, resulting in anomalous changes of n and T_e that can obscure phenomena of interest. Avoiding TBR is particularly important for experiments that do not probe the electrons directly because changes in T_e would not be observable. The scaling of R_{TBR} with ω_{pi} imposes a general restriction of $\Gamma_e \lesssim 0.1$ for experiments seeking to resolve ion dynamics, but this criteria can vary depending on the phenomenon of interest.

The time evolution of UCNPs can generally be broken down in three separate stages: electron equilibration, ion equilibration, and plasma expansion into the surrounding vacuum (Fig. 1.1). Another consequence of the small electron-ion mass ratio is the separation of the electron and ion equilibration timescales, which are closely related to their corresponding plasma oscillation frequency

$$\omega_{ps} = \sqrt{\frac{ne^2}{m_s \epsilon_0}}, \tag{1.2}$$

where m_s is the mass of species $s = e, i$. For typical experimental conditions, $\omega_{pe}^{-1} \approx 1\,\text{ns}$ and $\omega_{pi}^{-1} \approx 1\,\mu\text{s}$. On a much longer timescale, gradients in the electron thermal pressure drive plasma expansion into the surrounding vacuum with a characteristic hydrodynamic timescale of

$$\tau_{exp} = \sqrt{\frac{m_i \sigma(0)^2}{k_B T_e(0)}}, \tag{1.3}$$

where $\sigma(0)$ is the initial rms plasma size [39].

During the electron equilibration phase, the electrons equipartition the excess energy above photoionization to reach thermal equilibrium in a few 100 ns [44]. Throughout this process, hot electrons are able to escape from the plasma. However, as electrons escape, a potential well develops as a result of the growing net positive charge in the plasma that will eventually be sufficient to trap the remaining electrons. This process is known as ionic space-charge trapping and the fraction of captured electrons is given phenomenologically by

$$\frac{N_e}{N_i} = 1 - \sqrt{\frac{N^\star}{N_i}}, \tag{1.4}$$

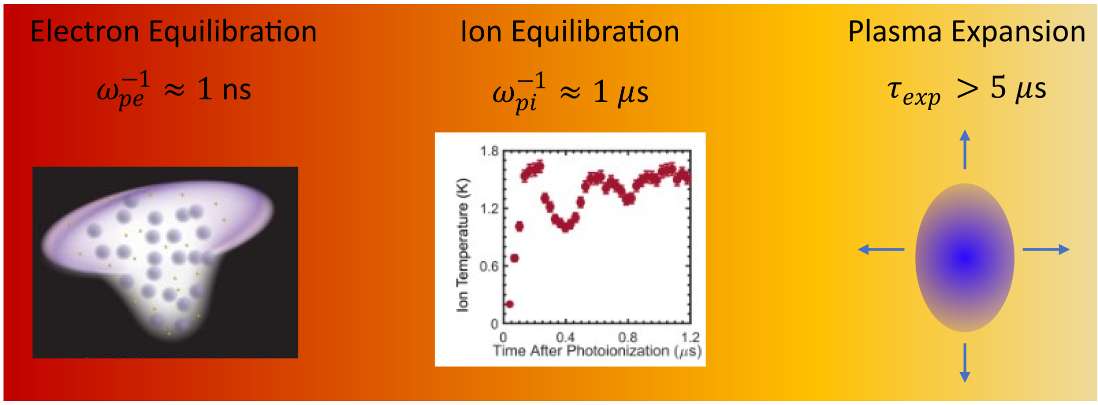

Figure 1.1 : Schematic showing the separation of fundamental timescales in a UCNP. Electron equilibration (left) occurs on the fastest timescale, during which the electrons become space-charge trapped by the potential of the ions. Ion equilibration then occurs, which sees the ions heat to $T_i \approx 1\,\mathrm{K}$ due to DIH. Following the equilibration of both species, the plasma expands into the surrounding vacuum due to gradients in the electron thermal pressure.

where $N^\star = E_{th}/\int V(r)n(\vec{r})dV$ is the number of ions with density distribution $n(\vec{r})$ that are required to trap a single electron with energy $E_{th} = 3k_BT_e/2$ through the Coulomb potential $V(r) = e^2/4\pi\epsilon_0 r$ [45]. For a plasma density distribution with rms width σ,

$$N^\star = C\frac{6\pi\epsilon_0\sigma}{e^2}k_BT_e, \tag{1.5}$$

where C depends on the geometry of the density distribution. Eqs. 1.4 and 1.5 have been verified experimentally for a spherically symmetric Gaussian distribution, for which $C = \sqrt{\pi/2}$ [45]. For typical experimental conditions, the vast majority of the electrons are trapped and the plasma is highly neutral. The plasmas described here are created by photoionizing atoms from a quadrupole magnetic trap and begin with an exponentially decaying density distribution (Eq. 2.8), for which $C \approx 1.65$. For a UCNP created in a quadrupole trap with peak density $10^9\,\mathrm{cm}^{-3}$, initial rms size of $1\,\mathrm{mm}$, and $T_e(0) = 20\,\mathrm{K}$, 98.4% of the electrons are trapped.

The initial ion equilibration is markedly different from that of the electrons. Immediately after photoionization, the ion temperature and spatial distribution are close to that of the precursor atoms. For typical UCNP densities, this would result in a very strongly coupled system with $\Gamma_i \gtrsim 100$. However, the ion positions are completely uncorrelated and there is significant excess potential energy in the system compared to one with equilibrium levels of spatial correlations that would nominally prevent ions from being close to one another. As a result, the ions undergo disorder-induced heating, where the excess energy is equipartitioned to thermal energy on a timescale of ω_{pi}^{-1} to reach an equilibrium temperature of

$$T_{DIH} = \frac{2}{3k_B} E_c \left| \tilde{U} + \frac{\kappa}{2} \right|, \tag{1.6}$$

where $\tilde{U}$ is the excess particle energy in units of E_c and $\kappa = a/\lambda_D$ is the plasma screening parameter for electron Debye length $\lambda_D = \sqrt{\epsilon_0 k_B T_e / ne^2}$. $\tilde{U}$ can be determined from tabulated values from [46]. During DIH, there is a rapid initial rise of the ion temperature that overshoots the equilibrium value and causes the system to undergo kinetic energy oscillations (Fig. 1.2), which are a characteristic of strongly coupled systems. The equilibrium ion temperature following DIH can range from $T_{DIH} \approx 0.25 - 3\,\mathrm{K}$ for typical UCNP initial conditions.

The longest of these timescales is that associated with the expansion of UCNPs, which is driven by electron thermal pressure and results in electron thermal energy being converted into directed ion motion. The expansion process can be viewed from the perspective of ambipolar diffusion, where the electrons and ions diffuse together at the ion acoustic velocity, $v_s \approx \sqrt{k_B T_e / m_i}$. Using a two-fluid treatment of the plasma, simple hydrodynamic arguments show that the acceleration of the ions is

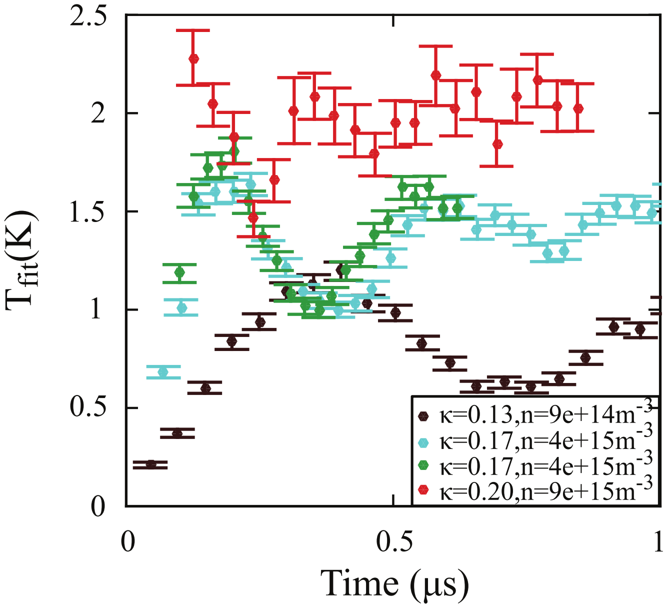

Figure 1.2 : Disorder-induced heating and kinetic energy oscillations in a UCNP with $T_e = 440\,\mathrm{K}$. Immediately after photoionization, the ions are very cold with temperatures near that of the precursor atoms. The ions subsequently heat rapidly in the first few 100 ns as excess potential energy is converted to thermal energy. The ion temperature overshoots the equilibrium value and undergoes kinetic energy oscillations. The equilibrium ion temperature following DIH can range from $T_{DIH} = 0.25 - 3\,\mathrm{K}$ for typical UCNP initial conditions. The legend indicates the plasma screening parameter (κ) and number density (n). Adapted from [41]. Copyright 2016 by the American Physical Society.

given by

$$\dot{\vec{v}} = -\frac{k_B T_e}{m_i}\frac{\nabla n}{n}, \tag{1.7}$$

where $\vec{v}$ is the hydrodynamic flow velocity of the plasma, the electron thermal pressure is given by the ideal gas equation of state, $P = nk_BT_e$ (valid for weakly coupled electrons), and T_e is assumed uniform [47]. This implies that the timescale for the expansion is given by

$$\tau \approx \frac{v_s}{\dot{v}} \approx -\frac{n}{\nabla n}\sqrt{\frac{m_i}{k_B T_e}}, \tag{1.8}$$

which is on the order of 10s of microseconds and sets the lifetime of the plasma. τ_{exp} is typically much longer than the ion/electron thermalization timescales, and as a result both species are considered in local thermal equilibrium (LTE) at the beginning of the expansion process.

The exact nature of the expansion depends on the geometry of the initial density distribution. In the special case of a quasi-neutral plasma ($n_e \approx n_i$) where the ions and electrons both maintain their own global thermal equilibrium and inelastic processes and electron-ion thermalization can be neglected, a plasma with a spherically symmetric Gaussian density distribution (Eq. 2.7), which occurs for UCNPs created by photoionizing atoms in a MOT [39] or atoms from a magnetic trap after ballistic expansion [36], realize a particular solution to the Vlasov equation where the plasma expansion is both adiabatic and self-similar, as described by the following set of rate equations:

$$\frac{\partial}{\partial t}\sigma^2 = 2\gamma\sigma^2 \tag{1.9}$$

$$\frac{\partial}{\partial t}\gamma = \frac{k_BT_e + k_BT_i}{m_i\sigma^2} - \gamma^2 \tag{1.10}$$

$$\frac{\partial}{\partial t}(k_BT_s) = -2\gamma k_BT_s, \tag{1.11}$$

where σ is the initial rms width of the density distribution, γ characterizes the local mean of the velocity distribution, and the last equation applies to both the electrons and ions. The self-similarity of the expansion arises because the gradient in the thermal pressure leads to a radial ion acceleration (i.e., $\vec{v} \propto \vec{r}$)

In addition to the conserved total energy $E_{tot} = \frac{3}{2}N_ik_B(T_e + T_i) + \frac{3}{2}N_im_i\gamma^2\sigma^2$, Eqs. 1.9−1.11 possess the integrals of motion $\sigma^2T_s =$const, reflecting the adiabatic cooling of both the electrons and ions during the plasma expansion [3]. These integrals of motion can be used to derive the following simple set of analytic solutions

$$\sigma(t) = \sigma(0)\sqrt{1 + t^2/\tau_{exp}^2} \tag{1.12}$$

$$\gamma(t) = \frac{t/\tau_{exp}^2}{1 + t^2/\tau_{exp}^2} \tag{1.13}$$

$$T_i(t) = \frac{T_i(0)}{1 + t^2/\tau_{exp}^2} \tag{1.14}$$

$$T_e(t) = \frac{T_e(0)}{1 + t^2/\tau_{exp}^2}. \tag{1.15}$$

The characteristic expansion time is given by

$$\tau_{exp} = \sqrt{\frac{m_i \sigma(0)^2}{k_B(T_e(0) + T_i(0))}} \tag{1.16}$$

and the hydrodynamic expansion velocity, which is the local mean velocity of the ions, is

$$\vec{v}(\vec{r}, t) = \gamma(t)\vec{r}. \tag{1.17}$$

The rate equations in Eqs. 1.9-1.11 are amenable to extensions that do not impact the self-similar nature of the expansion, which arises from the geometry of the density distribution. In [48], a hybrid kinetic and molecular-dynamic model was developed to incorporate the effects of correlations between the ions. This model provided a basis for further extensions, such as in [49] to include thermalization between the electrons and ions and most recently in [32] to treat laser cooling of the ions.

Recent UCNP experiments have transitioned to create the plasma by photoionizing atoms within a quadrupole magnetic trap [32, 50, 40], which have an exponentially decaying density distribution. One benefit of a purely magnetic trap is that significantly more atoms can be loaded compared to a magneto-optical trap. As a result, UCNPs can be created with larger initial plasma size without sacrificing plasma density and, therefore, with longer lifetimes. This was a crucial development for the first demonstration of laser cooling of ions in a neutral plasma [32], for which the plasma lifetime was the limiting factor for the time available for laser cooling.

The expansion of a UCNP with an exponentially decaying density distribution can generally be characterized with the same length (σ) and time (τ_{exp}) scales as their Gaussian counterparts, but the expansion is not self-similar and these scaling factors are only valid for short times after photoionization ($t \lesssim 2\tau_{exp}$) [40]. The dynamics also differ early in the expansion due to the sharply peaked cusp at the plasma center, where excess ion kinetic energy is observed following DIH. This deviation is likely due to local non-neutrality at early times and increases with the ratio of the electron mean free path to the length scale of the cusp. For lower electron temperature ($T_e \approx 20\,\mathrm{K}$) and higher plasma density ($n \approx 10^9\,\mathrm{cm}^{-3}$), kinetic effects are expected to be minimal, resulting in largely hydrodynamic conditions.

1.2 Connections to Plasmas in Far More Complex Environments

UCNPs are used to simulate a wide variety of plasmas ranging from fusion devices to dense astrophysical objects. These systems are generally very hot and exist under plasma conditions that are unfavorable for experimental study for one reason or another. Many are not able to be probed directly and those that can be, especially those that are strongly coupled, are complex systems with extremely high densities that result in experimentally inaccessible ion dynamical timescales, which scale closely with the inverse ion plasma oscillation frequency. UCNPs, on the other hand, are comparatively simple systems with highly controllable initial conditions, direct access via optical probes, and densities leading to $\omega_{pi}^{-1} \approx 1\,\mu\mathrm{s}$.

It is natural to wonder whether systems with such vastly differing density and temperature share the same physical properties. The connection between these systems stems from their mutual relation to the Yukawa one-component plasma (YOCP) model. The YOCP is commonly used to describe plasmas with one species of interest (i.e., ions) and another oppositely charged species (i.e., electrons) that provides a smooth and continuous neutralizing background. In this model, the electrons screen the ion-ion Coulomb interactions through the Debye-Huckle effect and the resulting interaction is characterized by a screened, repulsive $1/r$ potential

$$V_{ij}(r_i, r_j) = \frac{U_0}{r_{ij}} e^{-\frac{r_{ij}}{\lambda_D}}, \tag{1.18}$$

where $r_{ij} = |\vec{r}_i - \vec{r}_j|$ is the distance between particles i and j, U_0 is a measure of the interaction strength, and λ_D is the Debye length. The YOCP is valid when the neutralizing species is weakly coupled and equilibrates faster than the timescale for ion motion. The former is typically satisfied for UCNP experiments that operate under plasma conditions that avoid TBR, for which $\Gamma_e \lesssim 0.1$, and the latter is satisfied because of the small electron-ion mass ratio. The requirement for weak coupling of the electrons arises because the concept of Debye screening breaks down in the strongly coupled regime, where there is on average less than one particle per Debye sphere.

One important aspect of the YOCP is that only two parameters - κ and Γ_i - are required to uniquely define the plasma state in equilibrium [46, 41, 51]. This is made more clear by expressing the Yukawa potential in its natural units for time (ω_{pi}^{-1}), length (a), and energy (E_c)

$$\tilde{V}_{ij}(\tilde{r}_i, \tilde{r}_j) = \frac{\tilde{U}_0}{\tilde{r}_{ij}} e^{-\kappa \tilde{r}_{ij}}, \tag{1.19}$$

where the tilde indicates that quantities are normalized by the appropriate natural unit. The only free parameter in the potential is κ, which is solely dependent on the initial conditions, and Γ_i characterizes the kinetic energy of the system. Thus, any two plasmas characterized by the same value of κ and Γ_i will display universal behavior in natural units. This universality was confirmed experimentally using ultracold plasmas in [41] (Fig. 1.3(right)) and forms the basis for the generalization of experimental measurements of UCNPs with other systems of interest.

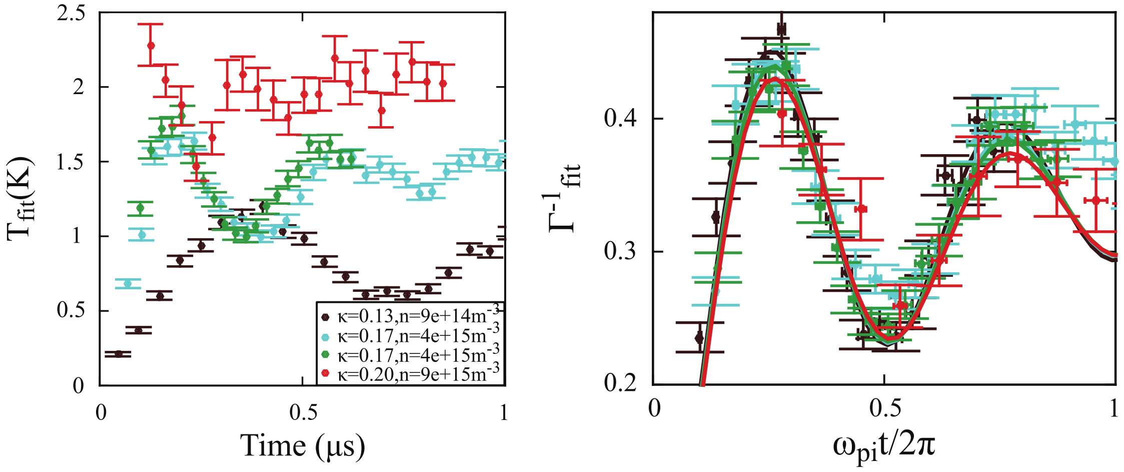

Figure 1.3 : Disorder-induced heating and kinetic energy oscillations in a UCNP with $T_e = 440\,\mathrm{K}$ in real (left) and scaled (right) units. Immediately after photoionization, the ions are very cold with temperatures near that of the precursor atoms. The ions subsequently heat rapidly in the first few 100 ns as excess potential energy is converted to thermal energy, overshooting and oscillating about the equilibrium value. The legend indicates the plasma screening parameter (κ) and density (n). DIH curves are shown for plasma density varying over one order of magnitude. In real units, the temperature evolution varies drastically, but in natural units they collapse onto a universal curve. Adapted from from [41]. Copyright 2016 by the American Physical Society.

Through the lens of the Yukawa model, the creation of a UCNP via photoionization can be thought of as a rapid quench from $\kappa = \infty$ (a gas of non-interacting atoms) to a value of κ set by the initial electron density and temperature. When viewed this way, it becomes clear that Γ_i after DIH is solely a function of κ because the ions always begin with the same initial conditions (i.e., negligible thermal energy and spatial correlations). One consequence of this is that ions in UCNP experiments will equilibrate in a narrow range of $\Gamma_i = 2 - 5$ for practical experimental conditions, which is just inside the strongly coupled regime [41, 52].

1.3 Excellent Platforms for Discovery

The combination of well-controlled initial conditions and precise diagnostics makes UCNPs an excellent platform for studies of fundamental plasma physics. Through control over the laser-cooling and trapping of the precursor atoms and the photoionization laser properties, the plasma density and electron temperature can be tuned across several orders of magnitude. The recent application of laser cooling/heating to the ions in a UCNP also allows the level of ion Coulomb coupling to be varied from $\Gamma = 0.1 - 11$. As a result, UCNPs can access conditions of weak or strong coupling and offer access to a wide array of plasma conditions that require hydrodynamic [53, 54], kinetic [53, 48, 55], molecular dynamic [48, 34, 52, 53, 41], and quantum descriptions [56, 57].

The UCNP platform is extremely versatile, due in part to the high level of control over the initial plasma density distribution, which is determined by the clean and highly reproducible density distribution of the precursor atoms and the intensity pattern of the photoionizing light. It is routine, for example, to trap atomic gases with Gaussian or exponentially decaying density distributions using magneto-optical or magnetic traps, respectively, and UCNPs can inherit these distributions directly by photoionizing the atoms with a uniform laser intensity. The plasma density distribution can also be sculpted through spatial modulation of the ionizing radiation [58] in ways that excite a variety of phenomena of interest. This technique is very flexible and has been used to realize plasma conditions that excite collective wave phenomena, such as the creation of ion acoustic waves (IAWs) using periodic spatial modulation onto the density distribution (Fig. 1.4). Studies to date have focused on IAWs in the linear regime [59, 60], but access to IAWs in the non-linear-dispersion regime of ion plasma oscillations should be possible by increasing the depth and lowering the length scale of the density modulation. Ion holes have also been created and studied in the hydrodynamic [54] and kinetic [55] regimes by creating UCNPs with a planar central density depletion.

Sculpting of the ion velocity distribution with optical pump-probe techniques has facilitated studies of Coulomb collision rates in the strongly coupled regime through the establishment of non-equilibrium velocity distributions. These experiments use counter-propagating beams of circularly polarized light to optically pump ions from one electronic ground state to another in a velocity-selective manner, resulting in skewed velocity distributions for the respective ground states that can be separately monitored using circularly polarized laser-induced-fluorescence imaging [61]. This technique was used in the first measurements of thermalization rates in strongly coupled UCNPs [34], and with improved time resolution it allowed for experimental measurement of the ion-velocity autocorrelation function and, thus, the self-diffusion constant [62]. These measurements provided important benchmarks for numerical models and kinetic theories attempting to capture the effect of strong coupling on collisional processes [63, 64].

1.4 Understanding Collisional Effects on Plasma Transport

A fundamental characteristic of plasmas is that their properties are influenced by magnetic fields at both the microscopic (collisional) and macroscopic (fluid) scale.

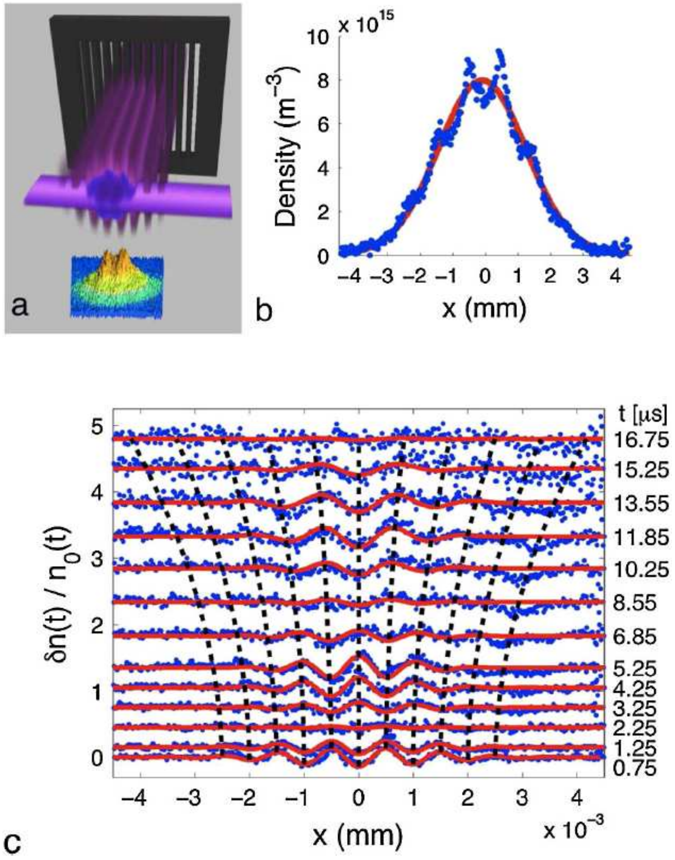

Figure 1.4 : Ion acoustic waves in an ultracold neutral plasma. (a) A small periodic density perturbation is imprinted onto the plasma by using a spatial mask on the ionizing radiation. (b) Laser-induced-fluorescence images of the initial plasma density distribution and (c) the evolution of the ion acoustic waves. Reused with permission from [59]. Copyright 2010 by the American Physical Society.

Consequently, magnetic fields can be used to control the transport of particles, energy, and momentum in plasmas, and this ability forms the basis for many experimental applications ranging from fusion devices to charged particle confinement. Most plasmas are magnetized in the sense that they exist within externally generated magnetic fields, but quantifying the strength of magnetization involves comparing the thermal gyroradius ($\rho = \sqrt{mk_BT}/eB$) to the characteristic length scale of the physical pro-

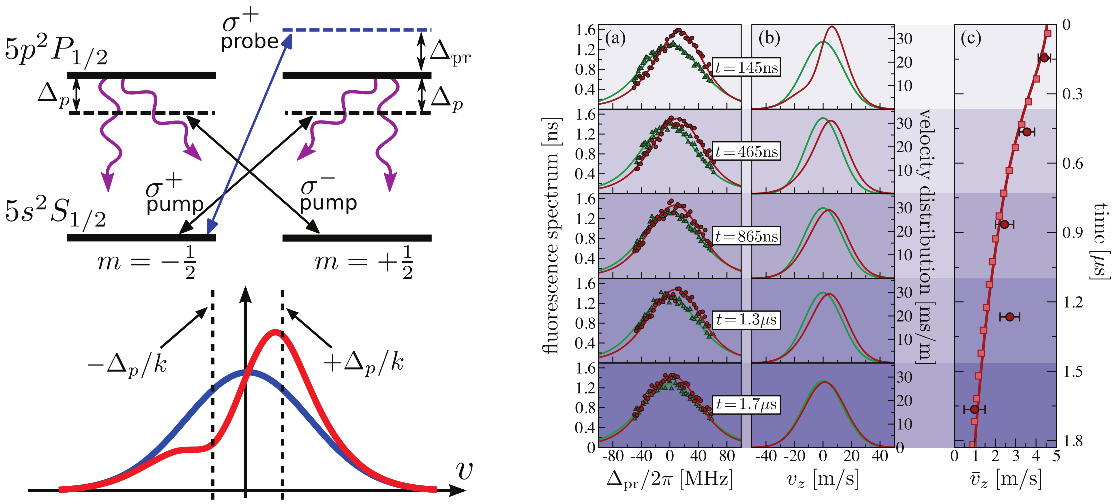

Figure 1.5 : Measurement of velocity relaxation using optical pump-probe techniques. (left) Two counter-propagating, cross-polarized laser beams optically pump the ions such that the velocity distribution of each ground state is non-Maxwellian. (right) Laser-induced-fluorescence measurements in panel (a) are recorded with circularly polarized imaging light to measure the velocity distribution of ions that occupy the $m_j = 1/2$ electronic ground state with (red) and without (green) optical pumping prior to imaging. The velocity distribution obtained by fitting the spectrum is shown in panel (b) and panel (c) shows the corresponding average velocity as a function of relaxation time. The left and right panels are adapted from [62] and [34], respectively.

cess being considered. With respect to bulk fluid motion, magnetization is quantified through the parameter $\delta = \rho/L$, where L sets the length scale for density variation within the plasma. With respect to collisions dynamics, magnetization is quantified through the parameter $\beta = \lambda_D/\rho$ because the Debye length sets the cutoff length for Coulomb interactions in neutral plasmas described by the OCP, although as we will see shortly, the collision mean free path (λ_{col}), Landau length (λ_L, i.e. the distance of closest approach), and the average interparticle spacing (a) are also important for characterizing varying degrees of magnetization.

The behavior of plasmas in magnetic fields is a tremendously broad and well-developed subject. Magnetohydrodynamic (MHD) models are often used to describe plasmas at the macroscopic scale and incorporate the influence of collisions on transport through a series of non-ideal terms with coefficients that describe processes such as diffusion, viscosity, and conductivity. Our understanding of plasma transport and our ability to model plasma dynamics hinge on obtaining accurate estimates of these coefficients, yet often times we must resort to computationally expensive particle simulations of the OCP to obtain estimates of these coefficients because conventional kinetic theories are invalidated by conditions of strong coupling or magnetization. The development of accurate kinetic theories is important because they shed light on the physical processes that undergird transport and provide an efficient means for estimating transport coefficients.

Traditional plasma kinetic theories use kinetic equations that incorporate collisions through a collision operator that is derived by obtaining closure to the Bogoliubov–Born–Green–Kirkwood–Yvon (BBGKY) hierarchy. There are several closure schemes that are valid for weakly coupled plasmas, but the simplest is that of Boltzmann. The Boltzmann equation, which describes binary collisions between particles, is derived by ignoring triplet correlations between particles and is popular because of the simplicity with which transport coefficients can be calculated. Once the interaction potential between particles is specified, Chapman-Enskog or Grad theories can be applied to obtain calculations of transport coefficients. In the case of the Coulomb potential, typical logarithmic divergences at close distances and due to the long-range nature of the Coulomb force can be avoided by truncating collision integrals at lengths shorter than the Landau length and longer than the Debye length, making the calculation of transport coefficients with Boltzmann theories relatively straightforward.

Unfortunately, traditional kinetic theories are not valid under conditions of strong coupling or magnetization, rendering MHD models and our understanding of these systems incomplete. Each condition presents its own challenge: strong coupling introduces spatial correlations that are ignored to obtain closure of the BBGKY hierarchy in Boltzmann theories, while strong magnetization complicates collision operators when particle gyromotion occurs on length scales relevant for collisions. Over the last decade, great progress has been made to extend Boltzmann-based theories to capture collisional dynamics in asymptotic regimes of either Coulomb coupling [20] or magnetization [21].

Boltzmann-based kinetic theories may operate under the binary collision approximation, but they can be extended to conditions where many-body effects are important through the introduction of an effective interaction potential that incorporates the averaged effects of spatial correlations [65, 20]. This concept is similar to accounting for electron screening effects through the use of the Debye-Huckle potential in place of the bare Coulomb potential. The effective potential - also known as the potential of mean force - consists of two terms: the bare interaction between two particles plus a term that uses the pair correlation function to average the effects of other surrounding particles [65]. Thus, once the pair correlation function is known for a given interaction potential, the effective potential may be derived and standard techniques can be used to derive transport coefficients. For the YOCP, MD simulations can be used to derive the pair correlation function, but there are also other avenues such as the hypernetted chain approximation [66]. This extension is very powerful because it does not require modification of the framework for the Boltzmann collision operator - only the interaction potential that is input to it - so it should in principle be compatible with other changes made to the Boltzmann collision operator that do not directly modify the interaction potential.

The primary issue with the Boltzmann collision operator with regards to magnetization is that its solutions rely on approximations that ignore changes of particle trajectory that are not derived from the specified interaction potential [5]. This presents problems for magnetized plasmas when particle gyromotion is significant on length scales associated with collisions (the Debye length for the YOCP). Novel methods have been developed recently to solve the generalized Boltzmann collision operator for particles colliding in the presence of a uniform magnetic field of arbitrary strength. This was recently demonstrated through calculations of the friction force for the YOCP [21], but there is nothing that precludes these methods from using an arbitrary potential, so the extension to the potential of mean force is promising.

1.5 Characterization of Plasma Magnetization Strength

Recent developments in plasma kinetic theory place us on the cusp of a unified kinetic theory that describes plasmas in overlapping regimes of strong coupling and magnetization. It is important now more than ever for experimental platforms to be capable of providing benchmarks for these theories. UCNPs happen to be uniquely suited to study strongly coupled plasmas across the full regime of magnetization of the Yukawa OCP. In addition to Γ and κ, the magnetized OCP model is characterized by the magnetization strength $\beta = \lambda_D/\rho$. The influence of magnetic fields on collisional transport generally increases with β, but identifying specific regimes of magnetization requires more careful consideration due to its interplay with Coulomb coupling.

MD simulations of the YOCP were used to identify four distinct regimes of magnetization with respect to collisional transport; the following discussion of these regimes follows closely to the discussion in [5] (Fig. 1.6). The longest length scale that is rele-

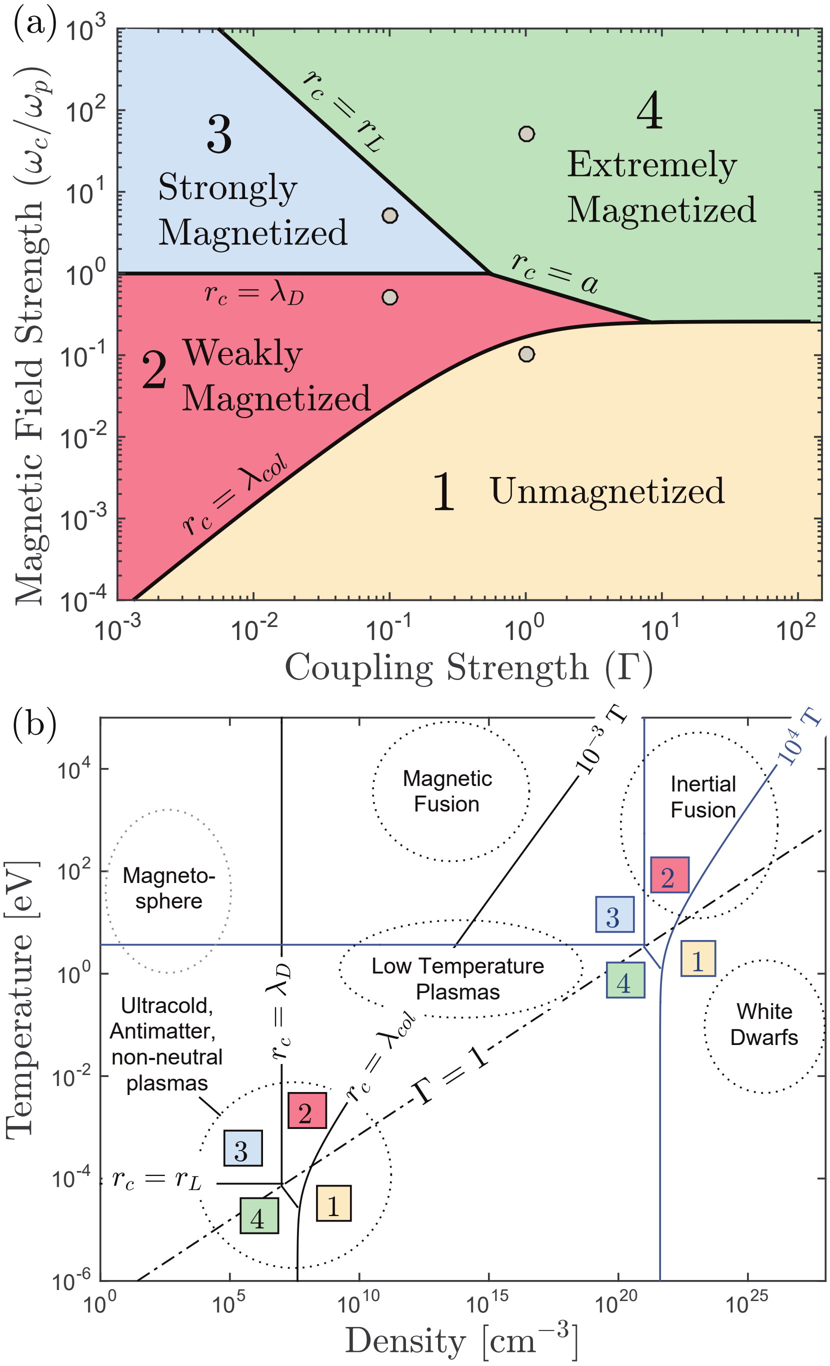

Figure 1.6 : Magnetization-coupling phase space for plasmas. Reused with permission from [5]. Copyright 2017 by the American Physical Society.

vant for collisions is the collision mean free path λ_{col}, because this sets the cutoff length for density variation for plasmas in the hydrodynamic regime. A plasma is considered unmagnetized when $\rho > \lambda_{col}$ because plasma transport has little to no dependence on the magnetic field strength. A plasma is generally considered magnetized when $\rho < \lambda_{col}$ and occupies the weakly magnetized regime when $\max(a, \lambda_D) < \rho < \lambda_{col}$, commonly referred to as the Braginskii regime. In this regime, magnetic fields are strong enough to influence macroscopic transport coefficients, but are weak enough that gyromotion is negligible during particle collisions. Thus, the magnetic fields are likely to influence the convection of particles but not the collision operator.

Magnetic fields begin to affect the collision operator in plasma kinetic theories when $\rho < \lambda_D$ and conventional kinetic theories cannot describe this regime. There are two separate regimes where this occurs: the strongly magnetized regime ($\lambda_L < \rho < \lambda_D$) and the extremely magnetized regime ($\rho < \min(a, \lambda_D, \lambda_L)$). In the strongly magnetized regime, particle diffusion along magnetic field lines and the relaxation of anisotropic temperature is relatively unaffected, but diffusion across magnetic field lines is significantly reduced. In the extremely magnetized regime, transport is heavily modified as particle motion becomes essentially one dimensional. Cross-axis thermalization and self-diffusion are generally severely inhibited.

1.6 Magnetization of UCNPs

The magnetization of UCNPs promises an open frontier for the UCNP research field. UCNPs have highly tunable density and electron temperature, allowing them to access the full regime of magnetization through the application of modest magnetic fields. Studies of magnetized UCNPs are of fundamental interest because the interplay of strong coupling and magnetization influence plasma transport and equilibration processes in ways that are difficult to describe theoretically and because this regime is important to other experimental applications such as dusty and high-energy density plasmas.

Beyond fundamental interest, UCNP experiments stand to benefit from magnetization from a practical standpoint. For example, the three-body recombination rate for magnetized plasmas is reduced by approximately an order of magnitude, which should allow for UCNPs to be created with lower electron temperatures [67]. Furthermore, disorder-induced heating is significantly decreased under strong magnetization, where particle motion becomes essentially one dimensional and collisional energy exchange in the plane perpendicular to the field line is significantly reduced.

The most important aspect, however, is the influence of magnetic fields on particle diffusion. Diffusion along magnetic field lines is most significantly impacted under extreme levels of magnetization, but particle diffusion across magnetic field lines is significantly reduced for both weakly and strongly magnetized systems [5]. A pioneering experiment demonstrated this by studying the expansion of a UCNP in a uniform magnetic field where the ions were weakly magnetized and the electrons were strongly magnetized [68]. The plasma expansion was found to be unaffected in the direction of the magnetic field, but the expansion across the field lines was significantly reduced and the peak fluid velocity was found to scale as $B^{-1/2}$.

A long standing goal in the field of UCNPs has been stretching the boundaries of possible Coulomb coupling that can be realized experimentally, which has traditionally been limited to $\Gamma \approx 2-5$. Recent experiments applying laser cooling to the ions in UCNPs has extended this range to $\Gamma = 0.1-11$, but limitations imposed by the rapid plasma expansion prevented this range from being extended further. The application of magnetic fields is a natural next step for improving the efficacy of laser forces. One reason for this is that spatially dependent magnetic fields can be used to manipulate the ion resonances in ways that expand the range where cooling is effective, but another is that magnetic fields in the proper configuration can be used for particle confinement, which should greatly extend the amount of time available for laser cooling ions at the field null.

The rest of this thesis is dedicated to describing the work that went into demonstrating the magnetic confinement of an ultracold neutral plasma created at the null of a biconic cusp (or quadrupole) magnetic field. Chapter 2 describes the creation of a UCNP by photoionizing spin-polarized atoms in a quadrupole magnetic trap with the use of a new pulsed dye laser system. The new laser system is also described in this chapter, including the use of iodine absorption spectroscopy to calibrate the laser frequency and the implementation of a multi-pass ionization scheme.

Chapter 3 will discuss the development of a quantitative model for LIF imaging of a UCNP in the presence of non-uniform external magnetic fields, which is validated using experimental data. This model uses velocity-resolved rate equations to account for ion population transfer between states coupled by the LIF laser and spontaneous emission to states involved in LIF and states dark to the imaging laser. A detailed characterization of this model is provided, including the ability to extract local measurements of plasma density, hydrodynamic flow velocity, ion temperature, and electron-spin polarization of the ions and its ability to capture pumping into off-resonant ground states throughout excitation.

Chapter 4 will discuss the time evolution of plasma density and hydrodynamic flow velocity distributions following plasma creation at the null of a biconic cusp field. The magnetized plasma evolution can be characterized by ambipolar-diffusion of a plasma in a magnetic field. Plasma expansion along magnetic fields is largely unaffected and leads to ions streaming out of the loss gaps along the symmetry (x) axis and the y-z plane. Plasma expansion across magnetic field lines is significantly reduced and long term trapping of these particles is facilitated by magnetic mirror trapping of the electrons. Chapter 5 discusses the interrelated dynamics of the plasma density and electron-spin polarization of the ions. Preliminary evidence suggests that the spin-flip rate in the plasma is low. Under these conditions, the ability to resolve the polarization could open up new avenues for measuring plasma diffusion.

Chapter 2

Creation of a UCNP in a Biconic Cusp Field

UCNPs have historically been created by photoionizing atoms from a seeded supersonic molecular beam or those trapped in a MOT, which yields a Gaussian plasma density distribution and a self-similar expansion that can be modeled with simple hydrodynamic equations [39, 48]. However, recent experiments have transitioned to photoionize atoms in a quadrupole magnetic trap to take advantage of the larger number of trapped atoms [32], the potential for confinement via the magnetic mirror effect [50], and the sharply peaked density distribution, which leads to plasma conditions where kinetic effects can be important [40].

This chapter describes the creation of a UCNP by photoionization of magnetically trapped atoms in a biconic cusp (or quadrupole) magnetic field. The discussion in this chapter begins with a review of the quadrupole magnetic field configuration, including a linear approximation to the field profile that is valid for small distances from the field null. The laser-cooling and magnetic trapping of metastable $^3P_2$ Sr atoms within this field configuration is discussed in Sec. 2.2. The magnetically trapped atoms are photoionized using a new pulsed dye laser in a multi-pass configuration. Sec. 2.3 provides a full characterization of this system, including measurement of the laser beam profile and calibration of its frequency using iodine absorption spectroscopy. Finally, this chapter concludes in Sec. 2.4 with a discussion of the plasma state following photoionization, including the electron-spin polarization of the ions.

2.1 Quadrupole Magnetic Fields

The quadrupole magnetic field configuration is formed between two current coils in the anti-Helmholtz configuration. The coils used in our laboratory consist of many turns of 4-mm-diameter wire around a cylindrical portion of the vacuum chamber that is 28 mm in diameter. Each coil is $\approx 36\,\text{mm} \times 28\,\text{mm}$ in a configuration depicted in Fig. 2.1. The coils can thus be characterized by a mean coil radius of 30 cm and a separation of 110 cm along the symmetry (x) axis.

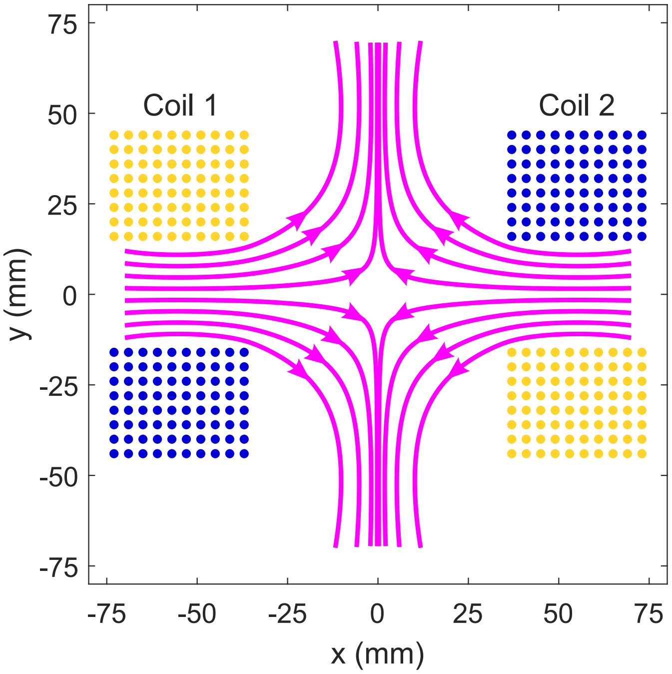

Figure 2.1 : Experimental schematic for the production of quadrupole magnetic fields using two sets of coils in the anti-Helmholtz configuration. The circular current loops are centered on the symmetry (x) axis of the laboratory coordinate system and the dot positions indicate where the circular current loops intersect the x-y plane (two dots for each loop: one below and one above the x axis). The dot coloring indicates current flow into (yellow) and out of (blue) the plane.

The magnetic field profile ($\vec{B}_{exp}$) for the experimental coils in Fig. 2.1 can be determined by treating the individual wraps of wire as a circular current loop and superimposing the respective fields. Simple analytic expressions exist for the magnetic field generated by a circular current loop [69]. The field components parallel ($B_\parallel$) and perpendicular ($B_\perp$) to the symmetry axis can be expressed in terms of complete integrals of the first (K) and second (E) kind as

$$\begin{aligned} B_\perp &= \frac{Cx}{2\alpha^2\beta\rho}\left[(a^2+\rho^2+x^2)E(k^2)-\alpha^2K(k^2)\right] \\ B_\parallel &= \frac{C}{2\alpha^2\beta}\left[(a^2-\rho^2-x^2)E(k^2)+\alpha^2K(k^2)\right], \end{aligned} \tag{2.1}$$

where $\rho = \sqrt{y^2+z^2}$ is the distance from the symmetry axis and $C = \mu_0 I/\pi$ is the constant of proportionality for current I. The modulus of the elliptic integrals, $k^2 = 1-\alpha^2/\beta^2$, is characterized by the parameters $\alpha^2 = a^2+\rho^2+z^2-2a\rho$ and $\beta^2 = a^2+\rho^2+z^2+2a\rho$.

For the work presented in this thesis, we are only interested in the magnetic field profile at small distances from the field null because the atomic gases trapped within this configuration have an rms radius of $\approx 1\,\mathrm{mm}$ and LIF measurements of the plasma dynamics are only captured within the camera field-of-view defined by $|x|, |y| < 5\,\mathrm{mm}$. At such small distances, the following linear approximation to the field profile is sufficient

$$\vec{B} = B'(-\vec{x}+\vec{y}/2+\vec{z}/2), \tag{2.2}$$

where B' is the linear magnetic field gradient along the symmetry axis for current I. All of the experimental data presented in this thesis uses $I = 80\,\mathrm{A}$, for which the field gradient was determined to be $B' = 151\,\mathrm{G/cm}$ by fitting the magnetized LIF model introduced in Chap. 3 to experimental data (Sec. 3.9). Fig. 2.2 plots the magnetic field amplitude (left) and direction (right) predicted by Eq. 2.2 for these conditions.

The linear field approximation is valid when the distance from the field null is much smaller than the radius of the coils generating the fields. Fig. 2.3 demonstrates

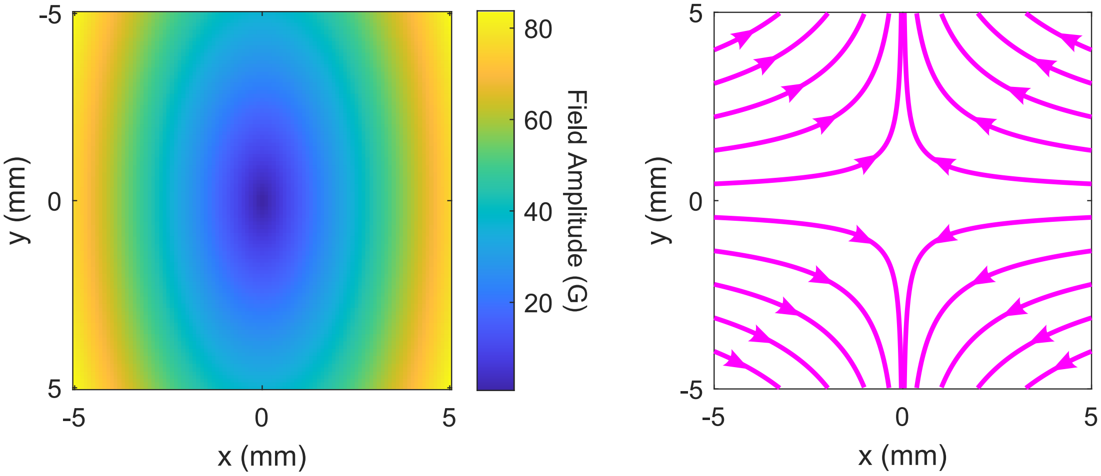

Figure 2.2 : Quadrupole magnetic field amplitude (left) and direction (right) near the field null, as predicted by Eq. 2.2.

this quantitatively by plotting the difference between the field magnitude (left) and direction (right) of the exact profile given by Eqs. 2.1 and the linear approximation given by Eq. 2.2. Throughout this thesis, the local field direction will be characterized by two angles: the angle that $\vec{B}$ subtends from the x-y plane ($\phi = \tan^{-1}(B_z/B_r)$, where $B_r = \sqrt{B_x^2 + B_y^2}$) and the angle that the projection of the field in the x-y plane subtends from the y axis, which is given by $\theta = \tan^{-1}(-B_x/B_y)$. For $|x|, |y| < 5\,\text{mm}$, the field amplitude and direction differ by less than 1 G and 1°, respectively, validating the use of the linear approximation.

2.2 Magnetic Trapping of Metastable $^3P_2$ Strontium Atoms

This section describes the magnetic trapping of laser-cooled $^3P_2$ strontium atoms within the quadrupole magnetic fields described in Sec. 2.1. A schematic of the levels and transitions that are relevant for the atom trapping and subsequent photoionization is provided in Fig. 2.4. The first step in this process is the laser cooling and

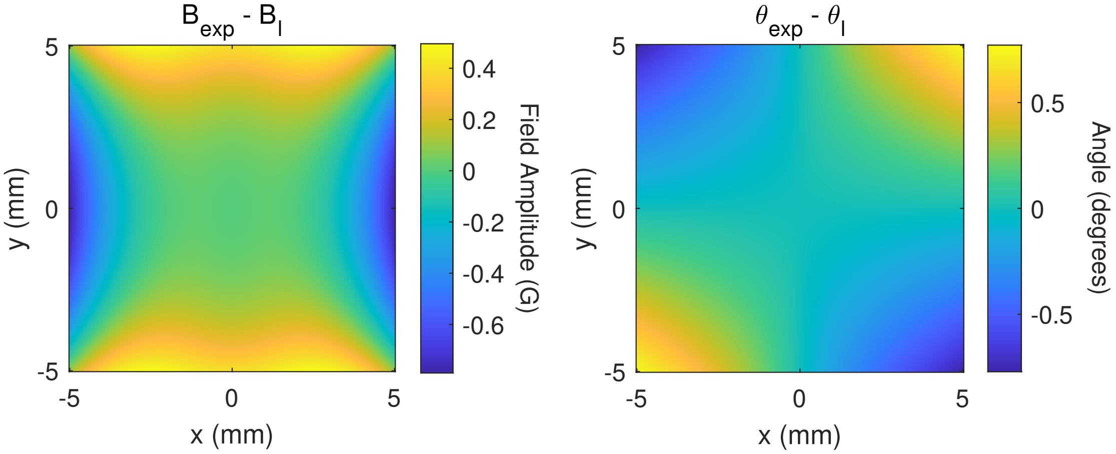

Figure 2.3 : Validating the linear approximation to the quadrupole magnetic field profile at distances from the field null that are small compared to the coil radius. The difference between the field amplitude (left) and direction (right) for the exact (B_{exp}, Eq. 2.1) and the linear approximation (B_l, Eq. 2.2) to the quadrupole magnetic field profile.

confinement of a Zeemann-slowed atomic beam of Sr atoms using a MOT that operates on the principal $5s^2\,{}^1S_0 - 5s5p\,{}^1P_1$ transition at 461 nm. Throughout the laser cooling process, atoms populate the metastable $5s5p\,{}^3P_2$ state through a weak decay path: $5s5p\,{}^1P_1 \rightarrow 5s4d\,{}^1D_2 \rightarrow 5s5p\,{}^3P_2$. Due to their large magnetic moment, low-field-seeking ${}^3P_2$ atoms ($m_j = +2, +1$) are then efficiently trapped in the quadrupole magnetic field of the MOT due to the interaction of the atomic magnetic dipole moment ($\vec{\mu}$) with the local magnetic field given by Eq. 2.2

$$U_B = \langle -\vec{\mu} \cdot \vec{B} \rangle = g_j m_j \mu_B B' \sqrt{x^2 + y^2/4 + z^2/4}, \tag{2.3}$$

where $g_j = 3/2$ is the Lande g factor for the ${}^3P_2$ state and μ_B is the Bohr magneton.

Magneto-optical trapping of the atoms is a necessary first step, rather than magnetic trapping, because strontium atoms in the electronic ground state do not possess a magnetic moment and the quadrupole fields would be too weak to trap Zeeman-slowed ${}^3P_2$ atoms directly. Thus, the laser cooling process serves both to pump the

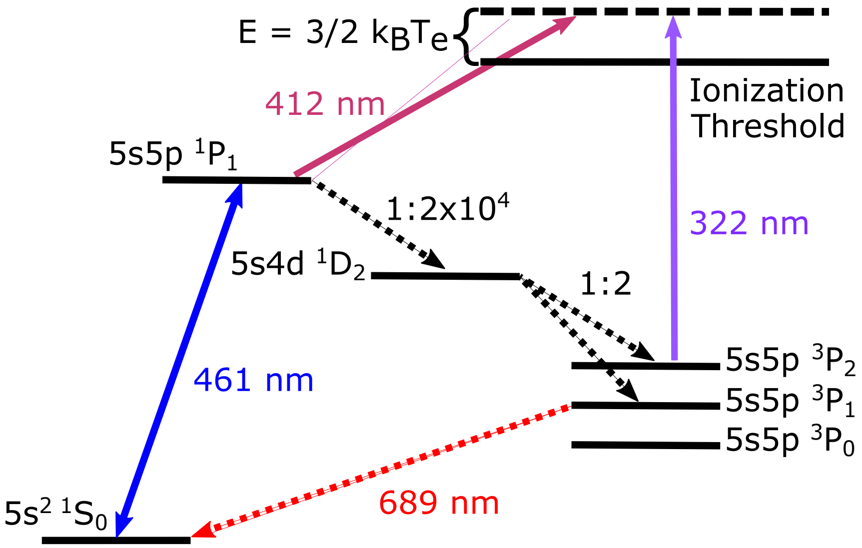

Figure 2.4 : Levels and transitions for laser cooling and magnetic trapping of strontium atoms and subsequent photoionization to form a UCNP. The principle transition at 461 nm is used for the initial laser cooling and magneto-optical trapping of Sr atoms. UCNPs can be created either by photoionizing $^1P_1$ atoms with a two-photon sequence (one from the continuous-wave MOT laser and another 412-nm photon from a pulsed dye laser) or $^3P_2$ atoms using a 322-nm photon from a pulsed dye laser.

the atoms into a magnetically trappable state and to cool them to temperatures that are suitable for magnetic trapping. A MOT operates using three pairs of red-detuned, counter-propagating laser beams - one pair for each spatial axis - in conjunction with with a magnetic field with strength that increases with distance from a central field null. The force that the MOT exerts on an atom can be expressed as

$$\vec{F}_{MOT} = -\alpha\vec{v} - \beta\vec{r}, \tag{2.4}$$

where α is the velocity damping rate and β is the strength of a spring-like restoring force [70]. The first term is responsible for laser cooling of the atoms. For a transition with natural linewidth γ, a simple expression for the damping rate can be obtained in the limit of small Zeeman shift ($\beta x \ll \gamma$) and low velocity ($kv \ll \gamma$):

$$\alpha = -\frac{8\hbar k^2 s_0 \Delta/\gamma}{(1 + s_0 + (2\Delta/\gamma)^2)^2}, \tag{2.5}$$

where $s_0 = I/I_{sat}$ is the saturation parameter for laser intensity I and saturation intensity I_{sat}, k is the photon wavenumber, and Δ is the laser detuning from atomic resonance. The second term in Eq. 2.4 leads to spatial confinement of the atoms when $\beta > 0$. For laser cooling on the 461-nm principle transition with red-detuned light, the atoms experience a spring-like potential of

$$U_{MOT} = \frac{4ks_0\Delta\mu_B B'\gamma}{(\gamma^2 + 4\Delta^2)^2} r^2 = \frac{1}{2}\beta r^2. \tag{2.6}$$

Despite the quadrupole magnetic field having cylindrical symmetry, the potential in Eq. 2.6 can be made spherically symmetric by modifying the saturation parameters for the respective axes. From equilibrium statistical mechanics, the density distribution for particles in a potential $U(r)$ is $n(r) = n_0 \exp(-U/k_B T)$. Thus, the density distribution for the potential in Eq. 2.6 is

$$n(r) = n_0 \exp\left(-\frac{r^2}{2\sigma^2}\right), \tag{2.7}$$

where n_0 is the peak number density and $\sigma = \sqrt{k_B T_a/\beta}$ is the initial rms plasma size for atom temperature T_a.

The number of atoms in a MOT saturates when the loading of atoms (i.e., the rate that atoms enter the trap with sufficiently low velocity) is balanced by loss from the trap due to collisions with hot background atoms or light-assisted collisions. Under typical conditions, the number of atoms saturates in 100 ms. Compared to other alkali-metal atoms, a rather large magnetic field gradient of ≈ 100 G/cm is required for the MOT to work effectively due to the large natural linewidth of $\gamma_{MOT}/2\pi = 30.5$ MHz and the large recoil momentum associated with the principle transition at

461 nm [71]. As a result, the magnetic fields used in the MOT are strong enough to trap the laser-cooled atoms that decay to the $^3P_2$ state through the interaction of the atomic magnetic dipole moment with the magnetic field. The density distribution for magnetically trapped atoms in the potential of a quadrupole magnetic trap (Eq. 2.3) is given by

$$n(\vec{r}) = n_0 \exp\left(\frac{-\sqrt{x^2 + y^2/4 + z^2/4}}{\alpha}\right), \tag{2.8}$$

where $\alpha = k_B T_a / 3\mu_B B'$ characterizes the plasma size along the x axis. In contrast to the MOT, magnetic traps can be loaded for much longer due to the long-lived nature of the $^3P_2$ state ($\sim 100\,\mathrm{s}$) and, therefore, significantly more atoms can be accumulated. The primary loss mechanism in a magnetic trap is non-adiabatic motion through the field null, which causes atom spins to flip to to the anti-trapped state, and the atom number saturates in $\approx 1\,\mathrm{s}$.

Atoms can be photoionized from either the MOT using a two-photon sequence consisting of one photon from the continuous wave MOT laser and another from a pulsed dye laser at 412 nm [3], for which the atom density distribution is a spherically symmetric Gaussian, or from the $^3P_2$ state using a single photon from a pulsed dye laser at 322 nm. The UCNPs described in this thesis used the latter method. Sec. 2.3 discusses the single-photon photoionization process in more detail, including the installation of a new pulsed dye laser system.

2.3 A Multi-Pass Photoionization Scheme

2.3.1 Installation of a New Pulsed Dye Laser System

The UCNPs described in this thesis were created by photoionizing magnetically trapped Sr atoms above threshold using a single 322-nm photon from a newly installed 10-ns pulsed dye laser system. Fig. 2.5 shows an experimental schematic of the new laser system, which consists of a ND6000 grating-tunable dye laser that is pumped by a Surelite II pulsed Nd:YAG laser. The production of 322-nm light begins with the Surelite II, which operates by pumping Nd doped YAG rods with a high-voltage Xenon flashlamp using a Q-switch to produce 10-ns pulses of 1064-nm light. This fundamental beam is then passed through a second-harmonic generating crystal (SHG) to convert the light to a wavelength of 532 nm and a dichroic mirror is used to remove any residual 1064-nm light. At normal operation, the Surelite II produces $\approx 250\,\mathrm{mJ}$ pulses of light.

The pulsed 532-nm YAG beam pumps the dye cells of the ND6000, which are filled with a solution of methanol and DCM dye. DCM is highly absorptive at 532 nm and has a wide emission band with a FWHM of $\approx 100\,\mathrm{nm}$ that is centered at 635.5 nm, making it possible to produce 322-nm light by passing the dye output beam through a SHG crystal. The ND6000 produces 50 mJ pulses of 644-nm light with a linewidth of $.08\,\mathrm{cm}^{-1}$ (3.3 pm) using a series of three dye cells that are transversely pumped by the YAG laser. The first cell is a rectangular Moya oscillator cell, which induces the dye to lase at a tunable wavelength using frequency-selective feedback from an adjustable grating.

The oscillator beam is amplified in to successive stages. In each stage, a dye cell is pumped transversely by the 532-nm pump beam and the oscillator beam stimulates emission from the excited molecules. The first amplification stage uses a rectangular dye cell and the second uses a capillary cell, which derives its name from its long and thin cylindrical nature. The preamplified beam is shaped to be slightly larger than the 5-mm-diameter capillary cell and expanding such that it is truncated upon entering and exiting the cell. This process ensures the capillary cell is filled uniformly, leading

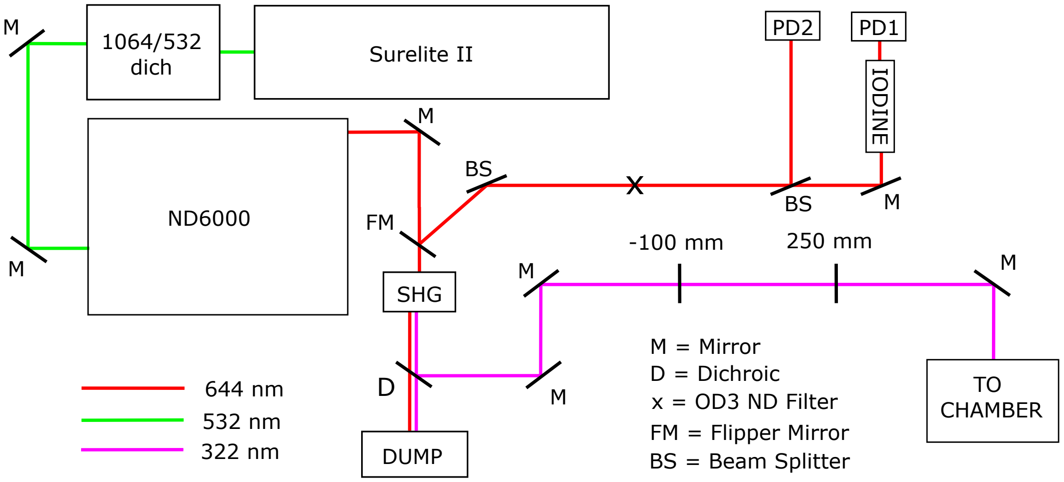

Figure 2.5 : Experimental schematic that describes the production of 10-ns pulses of 322-nm light for photoionizing Sr atoms in the $^3P_2$ state. The Surelite II Nd:YAG pulsed dye laser produces high-energy pulses of light at the fundamental YAG wavelength of 1064 nm and uses a second-harmonic generating (SHG) crystal to convert that light to 532 nm (green line). This beam passes through a dichroic to remove residual 1064-nm light and then pumps DCM dye within the ND6000 pulsed dye laser system to produce ~ 50 mJ pulses of 644-nm light (red line). The red dye output is then converted to 322 nm using an external SHG and is again cleaned up using a dichroic mirror. The 322-nm ionization beam is then passed through a 2.5× beam expander prior to being directed towards the chamber.

to an output beam that is highly collimated and circular with a uniform spatial distribution. The 644-nm dye laser output is then passed through a final external SHG crystal to obtain ≈ 10 mJ pulses of 322-nm light.

It is often desired for the ionization beam to be large compared to the size of the precursor atom cloud so that the ions directly inherit the atom density distribution. For the experiments presented here, the initial atom cloud is ≈ 1 mm, so to be safe we decided to expand the ionization beam from its nominal 5 mm size using a beam expander consisting of lenses with focal lengths -100 mm and 250 mm. The intensity distribution is measured using an Ophir SP298 Silicon CCD camera, which has a pixel size of 3.69 μm and an active area of 5.3 mm × 7.1 mm. UV radiation is typically poorly imaged with Silicon-based CCDs and the ionizing beam is too large for the active area, so a 4× UV image converter, which uses a fluorescent plate to convert the UV radiation to visible light with 50 um resolution, relays the beam onto the camera using a telescope. Fig. 2.6 shows the profile of the imaging laser with a 5-mm scale bar for perspective.

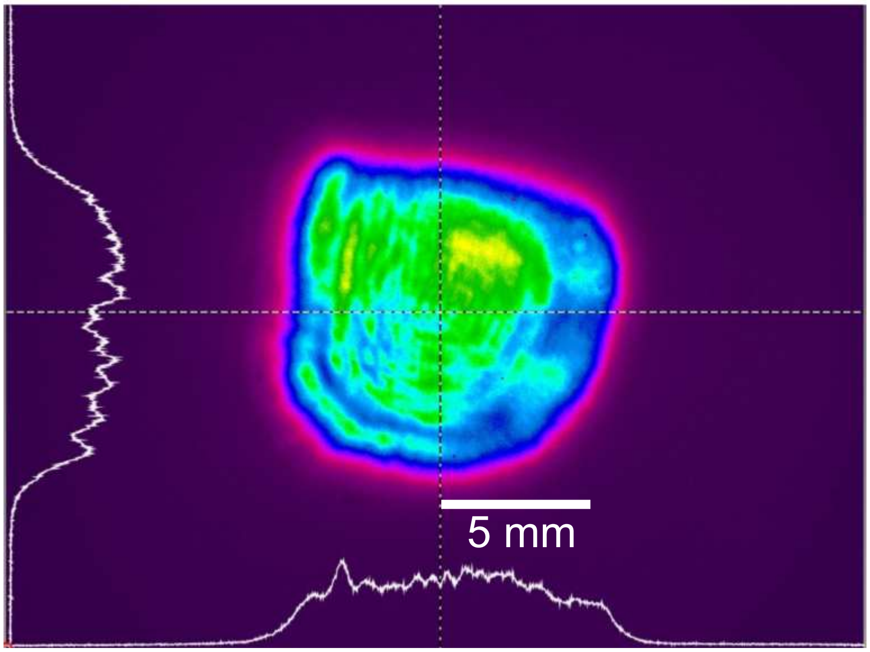

Figure 2.6 : Spatial profile of the 322-nm ionization beam.

One unfortunate consequence of the capillary amplification stage is circular diffraction patterns that arise due to truncation of the preamplifier beam on the capillary dye cell. The diffraction pattern is considerably more significant on the 644-nm dye beam (not shown here) with deeper and shorter length modulations compared to the 322-nm beam profile in Fig. 2.6. The diffraction on the ionization beam could be less significant due to saturation effects in the SHG conversion from 644 nm$-$322 nm or could be obscured by poor resolution in the 4× converter, but either way its existence is problematic because, if imprinted onto the plasma density distribution, could induce ion acoustic waves that heat the plasma [60]. This anomalous heating could limit the initial strength of Coulomb coupling in the plasma, but could also be problematic, for example, when using measurements of DIH in a UCNP as an absolute calibration of plasma density [41]. In the next section, a multi-pass ionization scheme is introduced, which should help mitigate the impact of the diffraction pattern through saturation of the ionization fraction.

2.3.2 Implementation of a Multi-Pass Ionization Scheme

The photoionization laser ionizes the atoms in a series of eight consecutive passes through the vacuum chamber, as depicted in Fig. 2.7, which provides a realistic model of the chamber with optical paths that are approximately to scale. This multi-pass ionization scheme is implemented through manipulation of the laser polarization to allow for several retro-reflections of the laser beam. The beam path begins in the upper left-hand side of Fig. 2.7 with the laser passing through a half-wave retardation ($\lambda/2$) plate that is rotated to maximize transmission through a polarization beam-splitting (PBS) cube. The beam then reflects off of mirrors M1-M3 to make two consecutive passes through the chamber and is then retro-reflected by mirror M4 to make two additional passes.

A quarter-wave retardation ($\lambda/4$) plate is attached to mirror M4, imparting a 90° phase shift to the laser polarization during retro-reflection. Following the first four passes through the chamber, the beam arrives back at the PBS cube, but this time is reflected by the cube due to the phase shift on the laser polarization. The beam is directed towards a second retro-reflecting mirror (M5) that directs the beam back onto its original path to complete an additional four passes through the chamber. Upon returning to the PBS cube for a second time, the laser polarization now has a cumulative 180° phase shift and transmits through the cube.

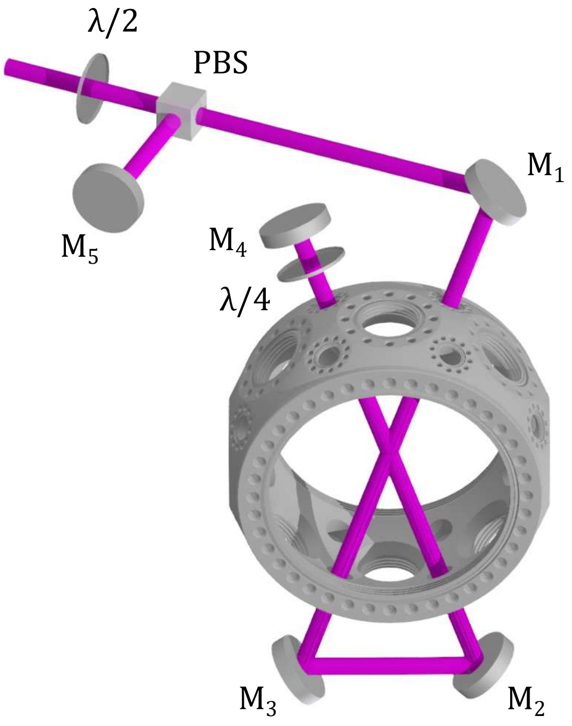

Figure 2.7 : Multi-pass ionization scheme. The pulsed 322-nm laser ionizes the atoms through a series of eight consecutive passes through the vacuum chamber, which is facilitated by polarization-selective retro-reflecting of the laser beam through four windows in the chamber using a polarization beamsplitting (PBS) cube and a quarter-wave ($\lambda/4$) retardation plate.

Recycling of the photoionization energy through the multi-pass scheme is generally helpful because it will increase the number of ions in the plasma, and along with it the plasma density and signal-to-noise ratio, but the primary benefit is that it will mitigate the impact of the diffraction patterns on the laser beam through saturation of the ionization fraction. The ionization fraction can be expressed in terms of the beam energy density ϵ and the ionization cross section σ_i as

$$N_i/N_a = 1 - \exp\left(-\frac{\epsilon\sigma_i}{E_p}\right), \tag{2.9}$$

where $E_p = hc/\lambda_p$ is the photoionization threshold. The energy density of the photoionization laser described in Sec. 2.3 can be approximated as $\epsilon = E/\pi r^2$, which is valid for a uniform pulse of light with total energy E and radius r. For typical pulse energies of 10 mJ, beam radius of 6 mm, and assuming an average power loss of 10% per pass through the chamber, the cumulative energy density would be $0.5\,\mathrm{J/mm^2}$. From the measurements in [36], which found $\sigma_i = 16.3 \pm 2.6\,\mathrm{Mb}$, this would suggest an ionization fraction of $\approx 65\%$, which is well into the saturation regime. The diffraction effects can be further be reduced through alignment of mirrors M_4 and M_5 in Fig. 2.3.2. By aligning the retro-reflected beams such that they do do not perfectly overlap with the original pass through the chamber, constructive interference of the diffraction pattern can largely be avoided.

Due to limited optical access to the vacuum chamber, the only viewports available for this configuration were the two pairs of mini (1.33 in.) ConFlat (CF) viewports shown in Fig. 2.7. At the time of implementation, the windows on these viewports did not possess anti-reflective (AR) coating and the recycling of the laser power would have been significantly limited by power loss through each pass. To prevent this, we constructed custom viewports that are AR-coated for the ionization wavelength of 322 nm. The construction of homemade viewports, as opposed to purchasing those that are commercially available, was motivated by several factors. Commercial viewports are often very expensive, but more importantly they tend to have limited optical quality near the edges. It is common, for example, for the edges of the substrate to not be optically flat and the coatings are often not effective near the edges due to a shadowing effect introduced during the coating process. This reduction of usable window area would limit the spatial size of UCNPs that could be created in the future.

Fig. 2.8 shows a schematic of our custom viewports, including a top-down view (left) and two section views labeled 'A' (middle) and 'B' (right). This design is based on the double-flange, solder-seal design from [72], which results in bakeable viewports that are robust under reattachment. A key aspect of this design was the decoupling of the substrate-flange seal from the high-stress sealing of the copper gasket. Each section view shows a (1) custom 1.33 in. CF flange, (2) indium o-rings, (3) AR-coated substrate, and (4) clamping flange, with the only difference being that section A shows the bolt holes for sealing the CF flange to the chamber and section B shows those for the substrate seal. Central holes were machined into the CF flange and clamping flange with diameter equal to the vacuum chamber's 16.5-mm aperture diameter.

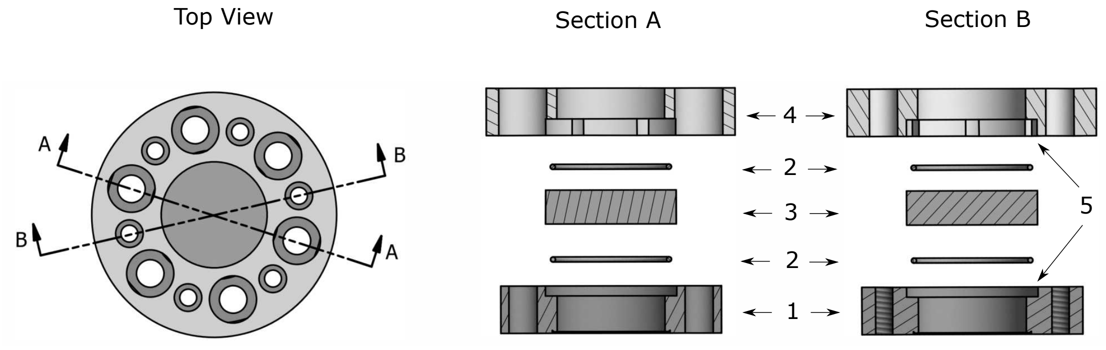

Figure 2.8 : Custom AR-coated viewports

Smooth edges (5) were machined into each flange to facilitate the substrate-flange seal with an indium o-ring on either side of the substrate. Indium was chosen as the o-ring material because it is relatively soft and serves to isolate the substrate from the sealing of the copper gasket while also being capable of providing a UVH seal. The o-rings are made of 99.99% pure indium solder wire with .03 in. diameter from Indium Corporation. Each o-ring was formed by cutting the solder wire to the length, wrapping it around an appropriately sized cylindrical piece of aluminum, and then joining the two ends by firmly pressing down on them.

Prior to assembly, all the components except for the indium solder were sonicated in successive baths of trichloroethylene, acetone, and methanol - each being rinsed off with the next chemical in the cycle prior to sonication - in order to prevent contaminants from entering the vacuum chamber. Ideally, the indium solder would have been sonicated as well, but unfortunately the sonication process made the indium brittle and formation of the o-ring was nearly impossible without it breaking into small pieces. To ensure cleanliness of the wire without degradation of the structural integrity, the wire was soaked for 24 hours in successive baths of acetone and methanol.

Four viewports were constructed according to Fig. 2.8 and leak-tested using a calibrated helium leak detector prior to attachment to the experimental vacuum chamber. The leak detector was important for determining how much pressure to apply to the substrate-flange seal. Too much pressure resulted in the indium being squished to the point that it leaked out into the visible portion of the glass, but too little pressure would result in an indium seal that was not robust under reattachment. The indium seal was made in three stages with the aid of the leak detector. The first seal was made prior to sealing of the copper gasket, with just enough pressure applied such that the indium o-rings could not move. Then, after the flange was sealed to the test setup using a copper gasket, the indium was tightened just enough for the roughing and mechanical turbo pump to establish a vacuum. Finally, the leak detector facilitated further tightening of the indium o-ring and each viewport was determined to be leak-free within the $4 \times 10^{-10}\,\mathrm{atm\,cm^3/s}$ noise floor of the detector. Each viewport was removed and reattached to the setup several times to ensure robustness of the substrate-flange seal prior to attachment to the vacuum chamber.

2.3.3 Frequency Calibration Using Iodine Absorption Spectroscopy

Precise control of the ionization laser's wavelength is important because essentially all of the excess photoionization energy above threshold is converted to electron thermal energy, effectively setting the initial electron temperature in the plasma. The energy required to ionize $^3P_2$ ^{88}Sr atoms can be determined from measurements of the atom energy levels, which are reviewed in [73]. The absolute energy of the $5s^2\,{}^1S_0$ ground state is $45925.6\,\mathrm{cm}^{-1}$ and the energy of of the $5s5p\,{}^3P_2$ state relative to the ground state is $14898.545\,\mathrm{cm}^{-1}$, so the ionization threshold corresponds to a wavelength of $\lambda_i = 322.2308\,\mathrm{nm}$. The electron temperature resulting from an ionizing photon with wavelength λ_p is given by

$$T_e = \frac{2hc}{3k_B}\left(\frac{1}{\lambda_p} - \frac{1}{\lambda_i}\right), \tag{2.10}$$

where h is Planck's constant and c is the speed of light.

The wavelength of the ionization laser is controlled using a computer program that tilts the grating within the Moya oscillator. The wavelength displayed within the control program $\tilde{\lambda}_N$, which is denoted with a tilde to distinguish the 644-nm photons from those doubled to 322 nm, is derived from an internal calibration that relies on linearity between the laser wavelength and the mechanism that tilts the grating relative to a precisely known reference point at $\tilde{\lambda}_N = 384.3295\,\mathrm{nm}$. This calibration is used to to characterize the wavelength across several 100s of nm, so slight non-linearity between the tilt and the wavelength is expected to introduce errors, especially at wavelengths far from the reference point.

To estimate the validity of the internal calibration, an external frequency calibration was conducted using iodine absorption spectroscopy. Spectroscopy on the $B-X$ iodine transition has historically provided a useful means for calibrating lasers in the visible and near-infrared due to extensive measurements of the absorption spectrum using Fourier transform (FT) interferometers. The iodine calibration described here compares experimental measurements of the absorption spectrum to those recorded from $14250 - 20100\,\mathrm{cm}^{-1}$ using a Doppler-limited FT interferometer with an instrument linewidth of $.02\,\mathrm{cm}^{-1}$ [74].

Fig. 2.5 shows a schematic for iodine absorption spectroscopy using the ND6000. The absorption spectrum is measured by recording the transmission of the 644-nm dye laser beam through a Thorlabs GC19100-I quartz iodine reference cell that is heated to $\sim 85°\mathrm{C}$ (similar to the temperature used in [74]) on a Thorlabs DET36A2 photodiode (PD1). To account for power fluctuations in the beam, a second photodiode (PD2) is used to record the power of a reference beam that does not pass through the iodine cell. The ratio of the integrated signals from PD1 and PD2 is proportional to the absorption spectrum. Prior to measurement, care was taken to ensure that the dye laser power was sufficiently small so as to not saturate the photodiodes. The power reduction involved operating the dye laser without pumping the amplifier cells and using a series of beam splitters and neutral density filters in the optical path.

To obtain a meaningful comparison of these measurements with the tabulated transmission results in [74], it was important to account for differences in spectral broadening introduced by the differing instrument linewidths. The spectra were both recorded with similar temperatures, but the lower bound on the linewidth of the ND6000 ($.08\,\mathrm{cm}^{-1}$) is larger than the FT interferometer ($.02\,\mathrm{cm}^{-1}$) from [74], so the tabulated results are convolved with a Lorentzian characterized by a FWHM of $.06\,\mathrm{cm}^{-1}$. It is also important to note that the procedure described above only provides a measurement that is proportional to absorption spectrum, not equal to it. At the time of recording, the signal on PD1 was not recorded at room temperature, so a conversion to an absolute measurement of the transmission is not possible. Thus, the spectra are only compared in arbitrary units where the vertical scales of each spectrum are adjusted to facilitate comparison.

Fig. 2.9 compares the experimental measurements with the tabulated data from [74] for two separate scans across the iodine cell, one from $\tilde{\lambda}_N = 643.8 - 644.45\,\mathrm{nm}$ (top) and another from $\tilde{\lambda}_N = 640.8 - 641.5\,\mathrm{nm}$ (bottom). In order to obtain good agreement with the reference measurements, a wavelength correction factor ($\Delta\tilde{\lambda}$) was applied to the experimental data, as indicated in the legend. A single value of $\Delta\tilde{\lambda}$ was not sufficient for the measurements to match the reference across the entire scan range, suggesting that the dye laser wavelength deviates from the linear approximation in the internal calibration. To estimate how much the correction factor changes with $\tilde{\lambda}_N$, each scan was broken up into two segments and a separate shift was applied to each - one to make the measurements match at low wavelength (blue) and the other at higher wavelength (purple).

Successive scans over the same wavelength ranges in Fig. 2.9 yield the same systematic behavior. In practice, the systematic errors are sufficiently small that the real dye laser wavelength ($\tilde{\lambda}_R$) can be determined using a wavelength-independent correction factor $\tilde{\lambda}_R = \tilde{\lambda}_N + \Delta\tilde{\lambda}$, where $\Delta\tilde{\lambda} = 0.3\,\mathrm{nm}$ is chosen to ensure agreement at wavelengths corresponding to $T_e \approx 10\,\mathrm{K}$. The electron temperature can be determined from Eq. 2.10 using $\lambda_p = \tilde{\lambda}_R/2$. At shorter wavelengths (higher T_e), the electron temperature will systematically be underestimated, but not by a significant amount. For example, at $\tilde{\lambda} = 640.8\,\mathrm{nm}$ ($T_e \approx 150\,\mathrm{K}$), the temperatures corresponding to $\Delta\tilde{\lambda} = 0.3\,\mathrm{nm}$ and $\Delta\tilde{\lambda} = 0.328\,\mathrm{nm}$ differ by less than 1%.

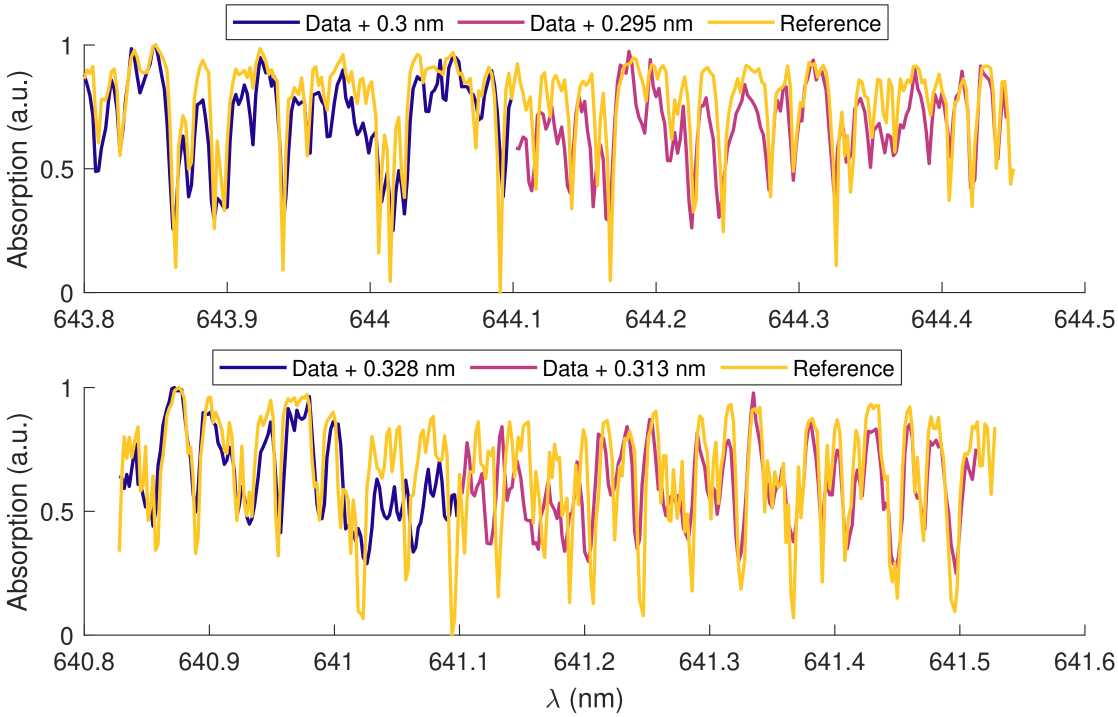

Figure 2.9 : Calibration of the dye laser wavelength with two separate scans of the iodine cell; one near the ionization threshold (top) and another near wavelengths corresponding to $T_e \approx 100\,\mathrm{K}$. Each scan is broken up into two segments, one with a wavelength correction chosen for agreement at the low (blue) and high (purple) ends of the wavelength range. Following the application of the correction factor, good qualitative agreement is found between experimental data and the reference measurements from [74].

2.4 Creation of a UCNP from Spin-Polarized Atoms

Following photoionization with the pulsed dye laser system that was introduced in Sec. 2.3.1, a single valence electron is liberated from a large fraction of the magnetically trapped ${}^3P_2$ atoms. The laser intensity is approximately uniform over the spatial extent of the precursor atom cloud and the liberated electron carries away the excess energy and angular momentum of the ionizing photon, so the photoionization process results in the ions inheriting the density, velocity, and internal-state distributions of the precursor atoms. UCNPs can be created within the biconic cusp field by leaving the fields on throughout ionization or the fields can be extinguished beforehand for studies without external magnetic fields. In either case, immediately after photoionization, the ion density distribution is given by the exponentially decaying distribution in Eq. 2.8 and the velocity distribution is close to that of the $T_a \approx 3\,\mathrm{mK}$ atoms.

When the fields are left on throughout ionization, the ions also inherit the electron-spin polarization of the atoms. The $^3P_2$ precursor atoms predominantly occupy the $m_j = +2$ magnetic sublevel because this state is the most efficiently trapped. In this state, both of the electrons are field aligned and the ions created this way are expected to be highly spin polarized because the remaining valence electron is unperturbed during photoionization. However, there are limits to the purity of the polarization when photoionizing magnetically trapped atoms because not all of the atoms in the trap occupy the polarized $m_j = +2$ state. For example, despite being less efficiently trapped, there will be a small population of atoms in the $m_j = +1$ state, in which only one of the electrons is field-aligned. Photoionization of these atoms will yield an imperfect ion polarization. A quantitative measurement of the relative population between the $m_j = +2$ and $m_j = +1$ states has not been done. Another source of impurity arises at the trap center where the atom spin states can change due to non-adiabatic motion through the field null. Atoms that flip into the anti-trapped $m_j = -1, -2$ states are not expected to remain in the in the trap for long periods of time, but it is possible for a significant number of unpolarized $m_j = 0$ atoms to accumulate, reducing the electron-spin polarization of the ions created near the field null.

The formation of polarized ions via photoionization is common for studies of various spin-dependent collision dynamics [75] and can be used for the characterization of magnetic and semiconductor materials [76]. This has been reported previously, for example, using laser-excited $^3P_1$ Sr atoms [76, 75]. Spin-polarized ions should also prove to be useful in the field of UCNPs because, as discussed in the next chapter, it is possible to directly measure the local ion polarization using laser-induced fluorescence. The global ion polarization is expected to be conserved because the ions are sufficiently cold and dilute that state-changing collisions are negligible and the plasma expansion occurs faster than spin-flips due to non-adiabatic motion through the field null. Thus, measurement of the electron-spin polarization in UCNPs should open up new avenues to study plasma flow and diffusion.

Chapter 3

LIF Imaging of a UCNP in a Magnetic Field

Application of LIF is widespread in many types of plasmas because of its power to resolve measurements of the density, velocity, and internal-state distributions of ionic and neutral species and measurement of electric and magnetic fields without perturbing the plasma. For example, LIF can be used to diagnose plasma processing sources [77], high-temperature plasmas such as in fusion research [78, 79, 80], and a large assortment of basic plasma configurations such as helicon plasmas [81], magnetron plasmas [82], magnetically confined pure ion plasmas [83], dusty plasmas [84, 85], and UCNPs [25, 33]. Compared to other applications, LIF in UCNPs is relatively straightforward because there is typically only one ion species, which occupies the ground electronic state in the absence of driving laser fields, and collision energies and densities are low enough to neglect state-changing collisions. This simplicity facilitates detailed, quantitative interpretation of experimental data.

Most experiments to date have been conducted in the absence of external fields, for which LIF in UCNPs is well characterized [33]. For Sr^+ ions imaged on the principle transition at 422 nm with linear laser polarization, the LIF spectrum consists of a single spectral feature that can be characterized as a Voigt profile, formed by convolving a power-broadened Lorentzian lineshape with the local velocity distribution. However, in the presence of external magnetic fields, this simplicity is lost due to Zeeman shifts of the LIF transitions and the varying direction of the magnetic field.

This chapter introduces a model for LIF in a magnetized UCNP that uses velocity-resolved rate equations (REs) to describe the transfer of ion population due to laser coupling and spontaneous emission. This description captures the optical pumping of ions into states that are not driven by the imaging laser and is validated with experimental data. The relative intensities of the resolved Zeeman components provide clear evidence that the ions are electron-spin polarized when created by photoionizing magnetically trapped ^{88}Sr atoms. The extension of this probe to the magnetized regime should open new avenues for studying thermal transport and the equilibration of plasmas in overlapping regimes of strong coupling and magnetization.

3.1 Experimental Details

In our experiment, the plasma is probed at an adjustable time after photoionization using LIF on the $5s\,^2S_{1/2} - 5p\,^2P_{1/2}$ transition of Sr$^+$ at 422 nm. The LIF laser, with detuning Δ from unperturbed resonance, propagates along the symmetry axis of the anti-Helmholtz coils to illuminate a $w \approx 1$ mm thick central slice of the plasma ($z \approx 0$) (Fig. 1a). A 1:1 optical relay is used to image scattered photons onto an intensified CCD camera over an excitation period with duration τ_E, which is set by CCD and LIF-laser gating, to obtain a spatially resolved LIF fluorescence spectrum, $F(x, y, \Delta)$, with 50 μm.

The four magnetic sublevels that are coupled by the LIF laser are shown in Fig. 3.1b. The unperturbed resonance of each level and Zeeman shifts for ions interacting with the quadrupole magnetic field in Eq. 2.2 are indicated by the dashed and solid lines, respectively (energies are not to scale). There are four possible transitions, with the photon polarization indicated in the figure. Each transition is associated with a unique line color, which will be used to refer to the transitions in subsequent figures throughout this thesis.

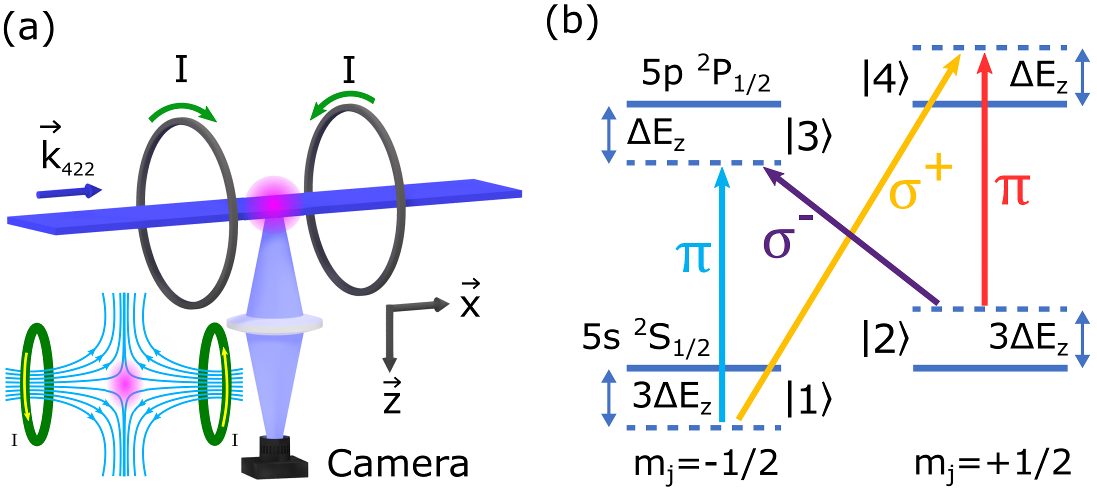

Figure 3.1 : (a) Experimental schematic for laser-induced-fluorescence (LIF) imaging and application of quadrupole magnetic fields using anti-Helmholtz coils (inset depicts field lines). The plasma is illuminated by a thin sheet of 422-nm light that propagates along the x axis. For the data described here, LIF polarization is linearly polarized along the y axis, left-hand circular, or right-hand circular. The ion fluorescence is imaged onto an intensified CCD camera using a 1:1 optical relay along the z axis. (b) Sr levels coupled by LIF laser with (dashed) and without (solid) Zeeman shifts, with the quantization axis taken to be along the local magnetic field. Reused with permission from [86]. Copyright 2022 by the American Physical Society.

The imaging transition at 422 nm is not closed, as ions can decay from the $^2P_{1/2}$ excited state into the $^2D_{3/2}$ state, which is dark to the imaging laser, with a rate of $\gamma_D = 9.5 \times 10^6\,\mathrm{s}^{-1}$ [87]. The decay rate from the $^2P_{1/2}$ excited state into the $^2S_{1/2}$ ground state is $\gamma = 1.26 \times 10^8\,\mathrm{s}^{-1}$ [87], so ions decay into the dark state 7% of the time. Decay into the dark state does not significantly impact most experiments because the laser intensity and excitation duration are sufficiently small that only one photon is scattered off of each ion, but the experiments described here use a relatively large exposure period of $\tau_E = 2\,\mu\mathrm{s}$, for which this process cannot be neglected.

3.1.1 Characterizing the LIF-Laser Intensity and Polarization

Precise knowledge of the LIF-laser intensity and polarization is important because it determines the strength of coupling to each of the imaging transitions shown in Fig. 3.1b. The imaging laser is a thin, collimated sheet of light that propagates along the symmetry (x) axis of the anti-Helmholtz coils (Fig. 3.1), such that the wavevector is given by $\vec{k}_{422} = k\hat{x}$, where $k = 2\pi/\lambda_{422}$. The beam is formed by passing a relatively symmetric Gaussian beam through a $12.5\,\mathrm{mm} \times 1\,\mathrm{mm}$ rectangular slit. An electro-optic gating system pulses the light on for imaging and supports pulses of duration $\tau_E = 50\,\mathrm{ns}$–$2\,\mu\mathrm{s}$.

The intensity distribution of the imaging sheet in the y-z plane is measured using an intensified CCD camera with a $6.6\,\mathrm{mm} \times 5.3\,\mathrm{mm}$ active area consisting of $10.4\,\mu\mathrm{m}$ pixels. The imaging sheet is larger than the active area on the camera, so multiple images were required in order to capture the full beam profile. To this end, the camera was mounted on a translation stage and five different images were taken at different positions along the y axis, as indicated in Fig. 3.2a. To a good approximation, the intensity distribution is separable and can be expressed as

$$I(y,z) = I_0 \tilde{I}_y(y) \tilde{I}_z(z), \tag{3.1}$$

where I_0 is the peak laser intensity and $\tilde{I}_y$ and $\tilde{I}_z$ are the relative intensity distributions along the respective axes, which are determined numerically by integrating over the other spatial coordinate.

Along the y axis, the beam largely retains its Gaussian character within the hard edges imposed by the slit (Fig. 3.1b). The data within the edges of the slit was fit to a Gaussian of the form

$$f(y) = f_0 \exp\left(-\frac{2(y-y_0)^2}{\sigma_y^2}\right), \tag{3.2}$$

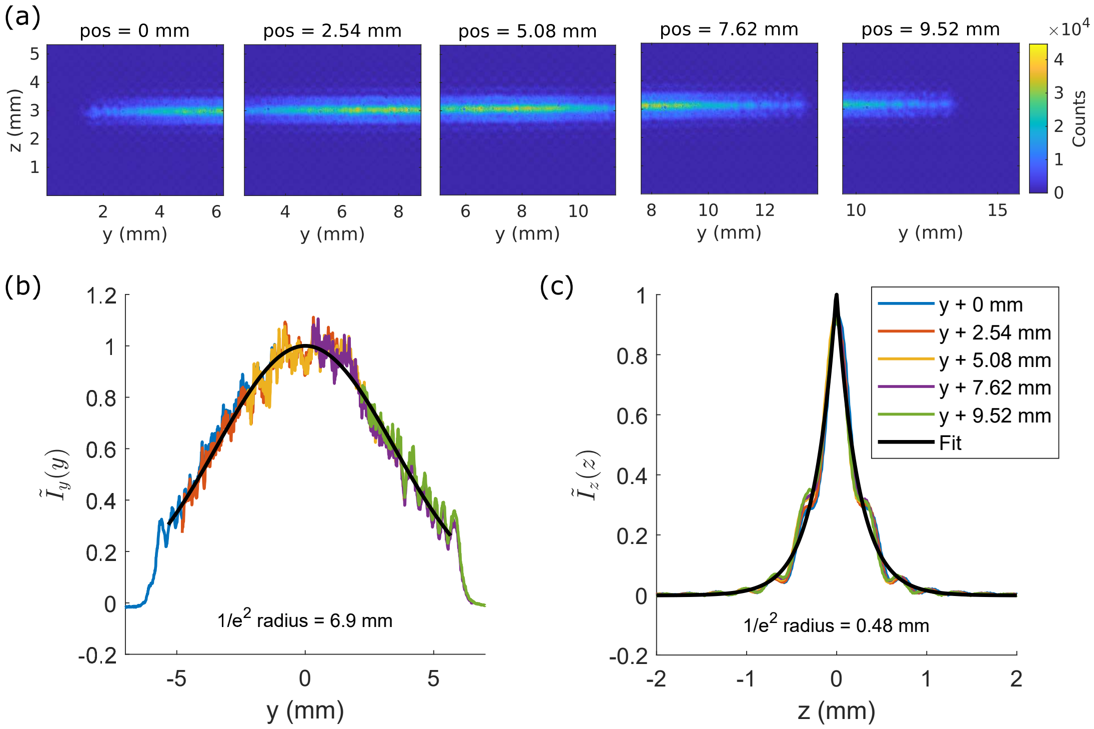

Figure 3.2 : (a) Images of the 422-nm imaging laser taken with an intensified CCD camera that is mounted to a translation stage. The y axis of each image has been shifted by the micrometer position indicated above each figure. (b) and (c) show the relative intensity distribution along the y and z axes, respectively. The $1/e^2$ radius along each axis is determined with a Gaussian ($\sigma_y = 6.9\,\mathrm{mm}$) and exponential ($\sigma_z = 0.48\,\mathrm{mm}$) fit, respectively.

which yielded a $1/\mathrm{e}^2$ radius of $\sigma_y = 6.9\,\mathrm{mm}$. The profile along the z axis is limited by diffraction from the slit (Fig. 3.2c) and is best characterized by an exponential of the form

$$f(z) = f_0 \exp\left(-\frac{|z - z_0|}{\sigma_z}\right), \tag{3.3}$$

which yields a $1/\mathrm{e}^2$ radius of $\sigma_z = 0.48\,\mathrm{mm}$.

An absolute calibration of the peak laser intensity (I_0) is obtained through an independent measurement of the pulse power (P). Due to the pulsed nature of the imaging beam, P is most accurately measured with a fast photodiode, rather than using a standard continuous-wave (CW) power meter to infer the laser power through a duty cycle measurement. A Thorlabs DET36A2 photodiode, which has a rise time that is smaller than the duration of the pulse, was used to measure the pulse height in voltage. Operating in the linear response regime of the photodiode, the photodiode was then calibrated to return power at 422 nm by measuring the voltage of a CW 422-nm beam of known power. The pulse power can be related to the peak intensity through the integration of Eq. 3.1:

$$P = I_0 \int dy \tilde{I}_y(y) \int dz \tilde{I}_z(z). \tag{3.4}$$

In practice, I_0 is determined through numerical integration of the measured beam profile, and the typical peak laser intensity used in this thesis is within the range $I_0 = 150 - 200\,\mathrm{W/m^2}$.

The imaging laser's electric field, $\vec{E}(\vec{r}, t)$, can be described as a monochromatic plane wave that propagates along the x axis and is polarized in the yz-plane:

$$\vec{E}(\vec{r}, t) = \frac{E_0(y, z)}{2} \left[\hat{\epsilon}(\eta, \phi)\, e^{i(kx - \nu t)} + c.c.\right], \tag{3.5}$$

where c.c. indicates the complex conjugate of the first term, the field amplitude is $E_0(y, z)$, and the laser polarization,

$$\hat{\epsilon}(\eta, \xi) = \eta \hat{y} + e^{i\xi} \sqrt{1 - \eta^2}\, \hat{z}, \tag{3.6}$$

is parameterized by $\eta \in [0, 1]$ and a phase shift ξ. Parameterized in this way, η and ξ can be chosen to represent any polarization in the y-z plane. For the measurements presented in this thesis, the LIF-laser is linearly polarized along the y axis ($\eta = 1$) or left or right-handed circular polarization (LC/RC: $\eta = 1/\sqrt{2}$, $\xi = \pm\pi/2$). The amplitude of the electric field is related to the laser intensity distribution as $I(y, z) = \frac{1}{2} c\epsilon_0 \left|E_0(y, z)^2\right|$.

3.2 Modeling the Capture of Laser-Induced Fluorescence

Laser-induced-fluorescence imaging works by relaying spontaneously emitted photons from a particle onto a camera. The rate of fluorescence emanating from any point in space after an excitation of duration τ is proportional to the local ion density n, the ensemble-averaged fraction of those ions $\bar{p}_e(\tau)$ that occupy an excited state $|e\rangle$, and the rate γ_{eg} with which the ions decay back into ground state $|g\rangle$. A main focus of this chapter is the calculation of $\bar{p}_e(\tau)$, which contains the physics of the ion's interaction with the optical and magnetic fields and plasma characteristics such as the local density, velocity, and internal-state distributions prior to excitation.

The level of sophistication required to model $\bar{p}_e$ depends on the excitation conditions at hand, and this topic is discussed in detail in Sec. 3.4. However, for the present discussion, lets assume that we know $\bar{p}_e$ for all τ and position relative to the plasma center, $\vec{r} = (x, y, z)$. The LIF signal collected by the camera from an area $A = \delta x \delta y$ centered at position $(x,\, y)$ arises from a volume element $V = Aw$ centered at $z = 0$. Assuming negligible variation of plasma properties over this volume, the signal during an excitation period of duration τ_E with detuning Δ is given by

$$F(x, y, \Delta) = V C_{p\rightarrow s} \int_0^{\tau_E} d\tau \sum_{e,g} n \bar{p}_e \gamma_{eg} \xi_{eg}, \tag{3.7}$$

where $C_{p\rightarrow s}$ is a photon-to-signal conversion factor, which is determined by an independent density calibration that relies on the density dependence of DIH [41]. The sum runs over the magnetic sublevels of the excited ($|e\rangle = |3\rangle, |4\rangle$) states and the ground ($|g\rangle = |1\rangle, |2\rangle$) states in Fig. 3.1b, where $|1\rangle$ and $|3\rangle$ correspond to $m_j = -1/2$. ξ_{eg} is the fraction of emitted photons that are relayed onto the camera due to decay from excited state $|e\rangle$ to ground state $|g\rangle$ and accounts for the dipole radiation pattern and collection solid angle of the optical relay. The decay rates between states coupled by the LIF laser are $\gamma_{41} = \gamma_{32} = 2\gamma/3$ and $\gamma_{31} = \gamma_{42} = \gamma/3$ (see Sec. 3.2.1).

Equation 3.7 makes the simplifying approximation of evaluating all quantities at the center of the volume V, which greatly reduces computational overhead compared to integrating and accounting for the variation of $\vec{B}$ and I across the local volume element. δx and δy are chosen to be sufficiently small such that the spatial variation of all quantities in the x-y plane can be neglected. However, significant variation of I over the camera line of sight along the z axis cannot be avoided. The most important impact of this variation is on the amount of optical pumping of ions into off resonant states. Computationally expensive calculations of spectra were performed, explicitly integrating over the z axis. It was found that the simple calculation (Eq. 3.7) with an effective laser intensity $\bar{I} = 0.45 I_0$ accurately matched the results of the more expensive calculation over a wide range of conditions (Sec. 3.7). This effective value and Eq. 3.7 were used for all results presented in this thesis.

3.2.1 Spontaneous Emission

Spontaneous emission occurs due to coupling of a particle's internal states with fluctuations in the vacuum field. This phenomenon is inherently quantum mechanical, and was first described by Dirac's quantum theory of radiation [88] and later by Weisskopf and Wigner within the framework of quantum electrodynamics [89]. These models captured the physics associated with spontaneous emission for the first time, and proved that Einstein's intuitively based semi-classical treatment from years prior also provides an accurate emission rate in the electric dipole approximation, where the wavelength of light is significantly larger than the size of the particle. The spontaneous emission rate from excited state $|e\rangle$ to ground state $|g\rangle$ in the electric dipole approximation is given by

$$\gamma_{eg} = \frac{4}{3}\frac{\alpha\omega^3}{c^2}|\hat{r}_{g\leftarrow e}|^2, \tag{3.8}$$

where α is the fine-structure constant, $\hbar\omega$ is the energy of the emitted radiation, and $\hat{r}_{g\leftarrow e} = \langle g|\hat{r}|e\rangle$ is the expectation of the position operator $\hat{r}$ [90].

The total decay rate, γ, from one manifold to another can be obtained by averaging over the possible initial (excited) states and summing over the possible final (ground) states and is given by

$$\gamma = \frac{1}{2j_e + 1}\sum_{e,g}\gamma_{eg}, \tag{3.9}$$

where j_e is the total angular momentum of the excited state. It is often useful to invert this relation because γ is typically quoted in the literature. The Wigner-Eckart (WE) theorem facilitates this inversion and describes the decomposition of a matrix element for a spherical tensor T^k_q with respect to an upper state $|u\rangle = |n'j'm'\rangle$ and a lower state $|l\rangle = |njm\rangle$ in terms of the double-bar (reduced) matrix element and either the Clebsch-Gordan coefficient (first line) or the 3-j symbol (second line):

$$\begin{aligned}\langle n'j'm'|T^k_q|njm\rangle &= (-1)^{2k}\frac{\langle jmkq|j'm'\rangle}{\sqrt{2j'+1}}\langle n'j'||T^k||nj\rangle \\ &= (-1)^{j'-m'}\begin{pmatrix} j' & k & j \\ -m' & q & m \end{pmatrix}\langle n'j'||T^k||nj\rangle,\end{aligned} \tag{3.10}$$

where the Racah and Wigner normalization convention has been used for the reduced matrix element [91, 92]. The 3-j symbol, now being abbreviated as J_{ul}, satisfies the relation

$$\sum_{u,l} J^2_{ul} = 1, \tag{3.11}$$

where u and l index the upper and lower states, respectively.

The position operator is a rank 1 spherical tensor and its components are given by $r_q = rC^1_q$, where $q = 0, \pm 1$ and $C^l_m = \sqrt{\frac{4\pi}{2l+1}}rY^l_m$ is the normalized spherical harmonic function. Eqs. 3.8−3.11 form a closed set of equations that can be used to express the reduced matrix element for $\hat{r}$ in terms of the total decay rate as

$$\langle n'j'||rC^1||nj\rangle = (-1)^{j+j_>}\sqrt{2j'+1}\sqrt{\frac{3\pi c^3\epsilon_0\hbar\gamma}{\omega^3 e^2}}, \tag{3.12}$$

where $j_>$ is the greater of j and j'. Finally, γ_{eg} can be related to γ by inserting Eqs. 3.10−3.12 into Eq. 3.8 to obtain

$$\gamma_{eg} = \sqrt{2j_e+1}J_{eg}^2\gamma. \tag{3.13}$$

For the transitions in Fig. 3.1b, the 3-j symbols are $J_{41} = J_{32} = -1/\sqrt{3}$ and $J_{31} = J_{42} = 1/\sqrt{6}$ and $j_e = 1/2$, so $\gamma_{41} = \gamma_{32} = \gamma/3$ and $\gamma_{42} = \gamma_{31} = 2\gamma/3$.

The angular distribution of spontaneously emitted photons follows that of an electric dipole relative to the quantization axis and depends on the angular momentum of the emitted photon (i.e., polarization of the decay channel). The LIF process described here involves the capture of both π- and σ-polarized radiation. The mean power radiated per unit solid angle $d\Omega = \sin(\alpha)d\alpha d\theta$ is

$$\begin{aligned} \frac{dP_\pi}{d\Omega} &= \frac{3P_0}{8\pi}\sin^2(\alpha) \\ \frac{dP_\sigma}{d\Omega} &= \frac{3P_0}{8\pi}\left[1-\frac{1}{2}\sin^2(\alpha)\right], \end{aligned} \tag{3.14}$$

where $P_0 = ck^4d^2/12\pi\epsilon_0$ is the the total power radiated for a linear dipole moment d, $k = \omega/c$, and α is the polar angle of a spherical coordinate system [93]. In the next section, these distributions are used to determine the fraction of photons captured by the optical relay for each photon polarization.

3.2.2 Photon Capture using an Optical Relay

The optical relay in Fig. 3.1a consists of a single spherical lens with diameter $d = 50.8\,\mathrm{mm}$ that is located a distance $L = 175\,\mathrm{mm}$ from the imaging plane (i.e., the midway point between the imaging plane and the camera). The lens diameter is sufficiently large compared to the FOV of the camera ($\approx 5\,\mathrm{mm}$ from the field null) that the ions can be treated as a point source. In this case, the relay will capture emitted photons for polar angles within $\delta\alpha = \pm\tan^{-1}(d/2L) \approx 8^\circ$ of the z axis in the lab coordinate system.

The fraction of captured photons for photon polarization $q = \pi, \sigma$ is computed by integrating the angular distribution over the captured solid angle and dividing it by the total number of radiated photons

$$\xi_q = \frac{1}{P_0} \int_{\alpha-\delta\alpha}^{\alpha+\delta\alpha} \int_0^{2\pi} d\alpha d\theta \sin(\alpha) f_q(\alpha - \phi), \tag{3.15}$$

where ϕ is the angle that the ion quantization axis subtends from the x-y plane and θ is the azimuth angle.

The captured fraction generally depends on the angle ϕ, but this dependence does not translate to the photon capture rate due to decay from each excited state. This can be seen through rearrangement of variables within the summation in Eq. 3.7, which can alternatively be expressed as

$$F(x, y, \Delta) = VC_{p\to s} \int_0^{\tau_E} d\tau \sum_e n\bar{p}_e r_e. \tag{3.16}$$

where $r_e = \sum_g \gamma_{eg}\xi_{eg}$ is proportional to the rate of photon capture due to decay from excited state $|e\rangle$. Due to the symmetry of the LIF level structure (Fig. 3.1), $r_3 = r_4$. Fig. 3.3 plots Eq. 3.15 and r_e/γ as a function of ϕ. r_e does not depend on ϕ because the two decay channels for each excited state - one with linear polarization with a rate $\gamma/3$ and another with circular polarization with a rate $2\gamma/3$ - are weighted such that the dependence cancels out. This validates the evaluation of ξ_{eg} in Eq. 3.7 at $\phi = 0$, for which the the captured fraction is 0.2067 (π) and 0.1047 (σ).

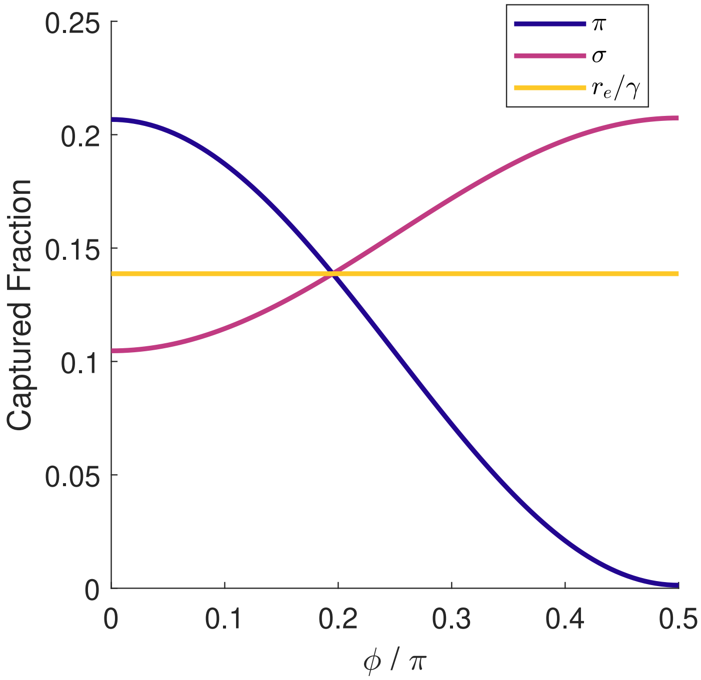

Figure 3.3 : Fraction of spontaneously emitted photons that are captured using the optical relay in Fig. 3.1a for spontaneous emission of π- and σ-polarized light as a function of the angle (ϕ) that the ion quantization axis subtends from the x-y plane. $r_e = \sum_g \gamma_{eg}\xi_{eg}$ is proportional to the total photon capture rate due to decay from excited state $|e\rangle$ to each LIF ground state $|g\rangle$. This quantity sums the contributions from the σ- and π- polarized decay paths and is found to be invariant with ϕ.

3.3 Electric Dipole Interaction for a Two-Level Ion in a Magnetic Field

Before introducing the model for the magnetized plasma in its full complexity, we will first consider the influence of the electric and magnetic fields during LIF on a single two-level ion with velocity $\vec{v}$. The direction of the external quadrupole magnetic field in Eq. 2.2 is chosen as the quantization axis for the ion's internal states, which consist of an excited state $|e\rangle$ that spontaneously decays to ground state $|g\rangle$ with rate γ. The excited state energy relative to the ground state is $\hbar\omega_0$ in the absence of a magnetic field.

3.3.1 Electric Dipole Interaction

The interaction between the ion and the light field in the electric dipole approximation is given by

$$\hat{H}_d = -\hat{d} \cdot \vec{E}, \tag{3.17}$$

where $\hat{d} = e\hat{r}$ is the dipole moment operator. The frequency of the LIF laser (ν) is Doppler-shifted in the ion's frame of reference and, to first order, the shifted frequency is $\nu' = \nu - kv_x$. By inserting the expression for the LIF-laser's electric field from Eq. 3.5, the dipole Hamiltonian in Eq. 3.17 can be rewritten as

$$\hat{H}_d = -\frac{\hbar}{2}\left[\hat{\Omega} e^{i(kx-\nu' t)} + \hat{\Omega}^\star e^{-i(kx-\nu' t)}\right], \tag{3.18}$$

where $\hat{\Omega} = \frac{eE_0}{\hbar}\hat{r} \cdot \hat{\epsilon}$ is the Rabi coupling operator. The matrix elements of $\hat{\Omega}$ quantify the laser-induced coupling between the internal states and are given by

$$\langle e|\hat{\Omega}|g\rangle \equiv \Omega_{e\leftarrow g} = \frac{eE_0}{\hbar}\langle e|\hat{r} \cdot \hat{\epsilon}|g\rangle. \tag{3.19}$$

A more meaningful expression for $\Omega_{e\leftarrow g}$ can be obtained by expanding the inner product in the spherical basis as $\hat{r} \cdot \hat{\epsilon} = \sum_q (-1)^q r_q \epsilon_{-q} = \sum_q r_q \epsilon_q^\star$. Using the WE theorem (Eq. 3.10) and the expression for the reduced matrix element for the position operator (Eq. 3.12), we find

$$\Omega_{e\leftarrow g} = \Omega_0 \epsilon_q^\star (-1)^{j+j'+j_>-m'} \sqrt{2j'+1} J_{eg}, \tag{3.20}$$

where $\Omega_0 = \sqrt{6\pi\gamma c^2 I/\hbar\omega^3}$ and $q = m_j^e - m_j^g$ [91]. Here, I have used the fact that $I(y,z) = \frac{1}{2}c\epsilon_0 \left|E_0(y,z)^2\right|$.

The components of ϵ_q depend on the direction of the ion quantization axis, which is set by the local quadrupole magnetic field. The local field coordinate system, denoted by primes, is defined such that $\hat{y}'$ lies in the x-y plane and $\hat{z}' = \hat{B}$. The direction of the local field can be characterized by $\phi = \sin^{-1}(z/\sqrt{4x^2 + y^2})$, the angle that $\hat{B}$ subtends from the x-y plane of the lab coordinate system, and $\theta = \tan^{-1}(2x/y)$, the angle that the projection of $\hat{B}$ in the x-y plane subtends from the y axis.

The LIF-laser's polarization vector in Eq. 3.6 is expressed in the basis of the lab coordinate system, but must be expressed in terms of the local field basis prior to determining the spherical tensor components. A change of basis from a vector using the lab coordinates ($\vec{v}$) to one using those of the local field ($\vec{v}'$) can be obtained through the transformation

$$\vec{v}' = R_{y'}(\pi/2 - \phi) R_z(\pi/2 - \theta)\vec{v}, \tag{3.21}$$

where R_a is a standard rotation matrix about the indicated axis a. The first rotation is about the z axis and the second is about the intermediate y' axis. Applying this transformation to the LIF-laser polarization yields

$$\begin{aligned} \hat{\epsilon} = &+ \hat{x}' \left[e^{i\xi}\sqrt{1-\eta^2}\cos(\phi) - \eta\cos(\theta)\sin(\theta) \right] \\ &+ \hat{y}' \left[\eta \sin(\theta) \right] \\ &+ \hat{z}' \left[e^{i\xi}\sqrt{1-\eta^2}\cos(\phi) + \eta\cos(\theta)\sin(\theta) \right]. \end{aligned} \tag{3.22}$$

The spherical tensor components of $\hat{\epsilon}$ are obtained by projection onto the spherical basis [$\hat{e}_0 = \hat{z}'$ and $\hat{e}_{\pm 1} = \mp(\hat{x}' \pm i\hat{y}')/\sqrt{2}$]:

$$\begin{aligned} \epsilon_0 &= \eta\cos(\theta)\cos(\phi) + e^{i\xi}\sqrt{1-\eta^2}\sin(\phi) \\ \epsilon_{\pm 1} &= -\frac{1}{\sqrt{2}} \left[i\eta\sin(\theta) \pm e^{i\xi}\sqrt{1-\eta^2}\cos(\phi) \mp \eta\cos(\theta)\sin(\phi) \right]. \end{aligned} \tag{3.23}$$

The fluorescence model in Eq. 3.7 evaluates all quantities in the x-y plane. In this simplifying case, the spherical tensor components reduce to

$$\begin{aligned} \epsilon_0 &= \eta\cos(\theta) \\ \epsilon_{\pm 1} &= -\frac{1}{\sqrt{2}} \left[i\eta\sin(\theta) \pm e^{i\xi}\sqrt{1-\eta^2} \right]. \end{aligned} \tag{3.24}$$

3.3.2 Hamiltonian for LIF in the Rotating Wave Approximation

The magnetic fields considered here ($|\vec{B}| \lesssim 100\,\mathrm{G}$) are sufficiently weak that the Zeeman shifts are small compared to the fine-structure splittings. In this weak-field limit, degenerate perturbation theory can be used to show that the Zeeman Hamiltonian is diagonal with elements indicating the first-order Zeeman shift:

$$\hbar\delta_\alpha = g_L^\alpha m_j^\alpha \mu_B |\vec{B}|, \tag{3.25}$$

where g_L^α and m_j^α are the Lande g-factor and magnetic quantum number for state $|\alpha\rangle$, respectively. The closed system Hamiltonian for LIF, including the interactions with the electric and magnetic field, but ignoring spontaneous emission, can be expanded in terms of the basis states as

$$\begin{aligned} \hat{H}_{LIF} =& \hbar\delta_g|g\rangle\langle g| + \hbar(\omega_0 + \delta_e)|e\rangle\langle e| \\ &- \frac{\hbar}{2}\left[\Omega_{e\leftarrow g}|e\rangle\langle g|e^{i(kx-\nu' t)} + \Omega^\star_{e\leftarrow g}|g\rangle\langle e|e^{i(kx-\nu' t)}\right] \\ &- \frac{\hbar}{2}\left[\Omega_{e\leftarrow g}|e\rangle\langle g|e^{-i(kx-\nu' t)} + \Omega^\star_{e\leftarrow g}|g\rangle\langle e|e^{-i(kx-\nu' t)}\right]. \end{aligned} \tag{3.26}$$

The dynamics of the ion wave function are typically studied in the interaction picture, where a unitary transformation is made to a basis set where the wave functions are rotating with the light field. A unitary transformation in quantum mechanics is made by using a unitary operator ($\hat{U}$) to change the current basis set ($|\psi\rangle$) to a new set given by $|\tilde{\psi}\rangle = \hat{U}|\psi\rangle$. The Hamiltonian under the new basis is

$$\tilde{H} = UHU^\dagger + i\hbar\frac{\partial U}{\partial t}U^\dagger, \tag{3.27}$$

where here, and going forward, the hat notation for quantum mechanical operators will be suppressed for clarity. The Hamiltonian can be transformed to the interaction picture using a unitary operator of the form $U = \exp(\sum_k i f_k(t)|k\rangle\langle k|)$, such that the

Hamiltonian transforms as

$$\tilde{H} = UHU^\dagger - \sum_k \hbar \frac{\partial f_k}{\partial t} |k\rangle\langle k|. \tag{3.28}$$

In this form, it becomes apparent that the first term on the right-hand side transforms the off-diagonal elements of H and the second term shifts the diagonal elements. Eq. 3.26 can be transformed with a unitary operator defined by $f_g = 1$ and $f_e = \nu' t$ and, after ignoring any remaining terms that oscillate as $\sim \exp(2i\nu' t)$ (i.e., the rotating wave approximation), we find

$$\begin{aligned} \tilde{H}_{LIF} = &\hbar\delta_g |g\rangle\langle g| + \hbar(\delta_e - \Delta')|e\rangle\langle e| \\ &- \frac{\hbar}{2}\left[\Omega_{e\leftarrow g}|e\rangle\langle g|e^{ikx} + \Omega^\star_{e\leftarrow g}|g\rangle\langle e|e^{-ikx}\right], \end{aligned} \tag{3.29}$$

where $\Delta' = \Delta - kv_x$ is the Doppler-shifted detuning of the LIF-laser.

3.3.3 The Master Equation

The time evolution of a single-particle, pure-state density matrix $\rho = |\psi\rangle\langle\psi|$ in an open quantum system is governed by the master equation, which can be written in its most general form as

$$\frac{\partial \rho}{\partial t} = \frac{1}{i\hbar}[H, \rho] - \sum_k \frac{\gamma_k}{2}\left(c_k^\dagger c_k \rho + \rho c_k^\dagger c_k - 2c_k \rho c_k^\dagger\right), \tag{3.30}$$

where c_k are quantum jump operators with associated decay rates γ_k (i.e., k indexes each possible decay path, so $c_k = |u\rangle\langle l|$ where the upper and lower states for the decay path are $|u\rangle$ and $|l\rangle$, respectively), and H is the closed system Hamiltonian. The diagonal elements of the density matrix (i.e., the populations $p_\alpha \equiv \rho_{\alpha\alpha} = \langle\alpha|\psi\rangle\langle\psi|\alpha\rangle$) quantify the probability that the ion occupies state $|\alpha\rangle$ and the off-diagonal elements (i.e., the coherences $\rho_{\alpha\beta} = \langle\alpha|\psi\rangle\langle\psi|\beta\rangle$) quantify the phase difference between projections onto the two states.

In the simple case of a two-level ion, the time evolution of the density matrix for $\tilde{H}_{LIF}$ in Eq. 3.29 is given by the following set of differential equations

$$\dot{\rho}_{ee} = -\frac{i}{2}(\Omega^{\star}_{e\leftarrow g}\rho_{eg} - \Omega_{e\leftarrow g}\rho_{ge}) - \gamma\rho_{ee} \tag{3.31}$$

$$\dot{\rho}_{gg} = +\frac{i}{2}(\Omega^{\star}_{e\leftarrow g}\rho_{eg} - \Omega_{e\leftarrow g}\rho_{ge}) + \gamma\rho_{ee} \tag{3.32}$$

$$\dot{\rho}_{eg} = (i\Delta_{eg} - \gamma/2)\rho_{eg} + \frac{i\Omega_{eg}}{2}(\rho_{gg} - \rho_{ee}). \tag{3.33}$$

where $\Delta_{eg} = \Delta' - (\delta_e - \delta_g)$ is the Doppler- and Zeeman-shifted resonance condition for the transition.

Analytic solutions to Eqs. 3.31—3.33, which describe damped Rabi oscillations for a two-level ion, can be found in textbooks [94], but they often do not exist for systems with more complicated level structures, as is the case for LIF of Sr$^+$ ions. In the absence of analytic solutions, Eqs. 3.31-3.33 can be numerically integrated with Runge-Kutta methods, however, numerical solutions to the exact equations become impractical when implemented in a fit routine because the number of equations that must be solved scales with the square of the basis size.

Fortunately, the early-time dynamics of the coherences, which damp on timescales of γ^{-1}, do not play a significant role in LIF when the excitation duration vastly exceeds the damping time ($\tau \gg \gamma^{-1}$), and we can seek solutions in the limit $t \gg \gamma^{-1}$, for which the coherences are in equilibrium (i.e., $\dot{\rho}_{\alpha\beta} = 0$). In this case, Eq. 3.33 can be used to demonstrate that the population transfer rate between states coupled by the laser is proportional to

$$\Omega^{\star}_{e\leftarrow g}\rho_{eg} - \Omega_{e\leftarrow g}\rho_{ge} = \frac{2i|\Omega_{e\leftarrow g}|^2\gamma}{\Delta_{eg}^2 + \gamma^2/4}(\rho_{gg} - \rho_{ee}). \tag{3.34}$$

Inserting Eq. 3.34 into Eqs. 3.31 and 3.32, we obtain the following set of rate equations

(REEs) that describe the transfer of population between the two states

$$\begin{aligned}\dot{p}_e &= +R_{eg}(p_g - p_e) - \gamma p_e \\ \dot{p}_g &= -R_{eg}(p_g - p_e) + \gamma p_e,\end{aligned} \tag{3.35}$$

where the scattering rate from state $|g\rangle$ to $|e\rangle$ is defined as

$$R_{eg} = \frac{|\Omega_{e\leftarrow g}|^2\gamma}{\Delta_{eg}^2 + \gamma^2/4}. \tag{3.36}$$

The solutions to Eqs. 3.35 will eventually reach the steady state where $\dot{p}_e = \dot{p}_g = 0$, such that the excited state population in equilibrium is

$$p_e = \frac{R_{eg}}{\gamma + 2R_{eg}} = \frac{s_{eg}/2}{1 + s_{eg} + 4\Delta_{eg}^2/\gamma^2}, \tag{3.37}$$

where $s_{eg} = 2|\Omega_{e\leftarrow g}|^2/\gamma^2$ is the saturation parameter for the transition.

The steady state solution in Eq. 3.37 saturates at a maximum value of $p_e = 1/2$ for $s_{eg} \gg \gamma$, leading to power-broadening of the transition, and can also be arrived at using Fermi's golden rule (FGR), which is valid for the two-level case when $\tau \gg \gamma^{-1}$. In the event that the transition is not closed and the excited state can decay to a state that is dark to the imaging laser, the steady-state solution can still be valid when less than one photon is scattered during excitation (i.e., $R_{eg}\tau \ll 1$).

3.4 Rate Equation Model for LIF Imaging in a Magnetic Field

In this section, we introduce a set of incoherent, collisionless rate equations (REs) to calculate $\bar{p}_e(\tau, \Delta, n, v_{x,hyd}, T_i, P)$, the ensemble-averaged fraction of ions that occupy excited state $|e\rangle$ after an excitation of duration τ that is characterized by Eq. 3.43 and includes spontaneous emission from the ${}^2P_{1/2}$ excited state to the ${}^2S_{1/2}$ electronic ground state and the $^2D_{3/2}$ dark state. The calculations of $\bar{p}_e$ are then input to the fluorescence model in Eq. 3.7, which is used to fit local LIF spectra and extract measurements of plasma density (n), hydrodynamic fluid velocity along the LIF-laser propagation direction ($v_{x,hyd}$), ion temperature (T_i), and electron-spin polarization (P) inside volume V at position $x, y, z = 0$. These quantities vary with position and plasma evolution time t, but for brevity these dependencies are not explicitly indicated. The plasma density, hydrodynamic fluid velocity, and ion temperature are also assumed to be stationary in time during excitation, which is valid because $\tau_E \ll \tau_{exp}$.

At the beginning of the excitation period ($\tau = 0$), the ions occupy the $^2S_{1/2}$ ground manifold ($\bar{p}_1 + \bar{p}_2 = 1$, $\bar{p}_3 = \bar{p}_4 = 0$) with electron-spin polarization $P = \bar{p}_2 - \bar{p}_1$. The ions are assumed to be in local thermal equilibrium with Maxwell-Boltzmann velocity distribution centered around $v_{x,hyd}$, $G(v_x, v_{x,hyd}, T_i)$, therefore the probability that an ion with velocity v_x occupies state $|k\rangle$ at $\tau = 0$ is given by $p_k(v_x, \tau = 0, n, v_{x,hyd}, T_i, P) = \bar{p}_k(\tau = 0)G(v_x)$. (Here, and going forward, we suppress arguments of functions for clarity.) This formalism only tracks the velocity along the x axis because the Doppler shift of the LIF excitation is only sensitive to this component. For $\tau > 0$, the velocity dependence of $p_k(v_x, \tau)$ is not necessarily Gaussian and the ensemble average can be computed as

$$\bar{p}_k(\tau) = \int_{-\infty}^{\infty} dv_x p_k(v_x, \tau). \tag{3.38}$$

In the absence of magnetic fields, $F(x, y, \Delta)$ takes on a simple form when imaging a UCNP with linear polarization [33]. In this case, the ion quantization axis is set by the LIF-laser polarization direction, so the degenerate π transitions are driven equally and p_e quickly stabilizes after a few times the excited state lifetime ($\gamma^{-1} \approx 8\,\text{ns}$). The resulting spectrum, typically recorded after an excitation period of a few 100 ns, can be described as a single Voigt profile, formed by convolving the single-particle, power-broadened Lorentzian lineshape with the local velocity distribution [33].

In the presence of quadrupole magnetic fields, this simplicity is lost due to Zeeman shifts of the LIF transitions and the varying direction of the magnetic field, which is chosen as the quantization axis (Fig. 3.1b). The laser excitation rate from ground state $|g\rangle$ to excited state $|e\rangle$ is given by

$$R_{eg} = \frac{\Omega^2_{e\leftarrow g}\gamma_{tot}}{\gamma^2_{tot} + 4\Delta^2_{eg}}, \tag{3.39}$$

where $\Omega_{e\leftarrow g}$ is the Rabi coupling between the respective states, Δ_{eg} is the Doppler- and Zeeman-shifted resonance condition, and $\gamma_{tot} = \gamma + \gamma_D + \gamma_L$ is the effective linewidth including the laser linewidth $\gamma_L/2\pi = 5\,\mathrm{MHz}$. The resonance condition and Rabi couplings that determine the laser excitation rate for each transition are dependent on the spatially varying magnetic field strength and direction, respectively. In order to determine $\Omega_{e\leftarrow g}$, the LIF-laser polarization must be projected onto the coordinate frame of the local magnetic field and then expressed in the spherical tensor basis (Sec. 3.3.1). The largest coupling in this thesis, $\Omega \approx 0.375\gamma$, occurs while imaging with LC/RC polarization with the local magnetic field parallel to the LIF-propagation direction. The observed strength of each spectral Zeeman component depends on the laser polarization and $P(\tau = 0)$.

In Eq. 3.7, the effects of the magnetic fields, the LIF-laser intensity and polarization, and electron-spin polarization are contained within p_e, which is calculated using the following set of REs that describe the transfer of ion population between states due to photon scatter and spontaneous decay, including decay into the metastable

${}^2D_{3/2}$ manifold, which occurs with rate $\gamma_D = 9.5 \times 10^6\,\mathrm{s}^{-1}$ [87].

$$\begin{aligned} \frac{\partial p_g}{\partial t} &= \sum_e -R_{eg}(p_g - p_e) + \gamma_{eg} p_e \\ \frac{\partial p_e}{\partial t} &= \sum_g (R_{eg}(p_g - p_e) - \gamma_{eg} p_e) - \gamma_D p_e. \end{aligned} \tag{3.40}$$

The REs are solved using a 4th-order Runge-Kutta method with a fixed timestep $d\tau = 0.25\gamma^{-1}$ for $\tau < 4\gamma^{-1}$ to capture the initial rise and $d\tau = 2\gamma^{-1}$ at later times to capture the longer timescale changes due to optical pumping. The RE formalism is analogous to the rate equations introduced for the two-level ion in Sec. 3.3.3, where the time dependence of ion coherences, which are present in an optical Bloch treatment, are neglected, which is justified because $\gamma^{-1} \ll \tau_E$. However, the REs in Eq. 3.40 additionally neglect the coherences between states not directly coupled by the LIF laser, which are typically at least an order of magnitude smaller than those that are coupled. The systematic errors associated with this treatment of the coherences is quantified in Sec. 3.8 through comparison of the REs with exact solutions to the master equation (Eq. 3.30) for LIF of Sr^+.

This treatment also neglects velocity-changing collisions, which is justified using combined molecular-dynamics and quantum-trajectories (MDQT) simulations for typical experimental densities $n = 10^6 - 10^9\,\mathrm{cm}^{-3}$ (Sec. 3.6). Because transfer between different velocity classes can be neglected, the v_x and Δ dependence of p_e can in practice be reduced to a dependence on the Doppler-shifted laser detuning $\Delta' = \Delta - kv_x$. The REs are solved for $p_e(\Delta', \tau)$ at a distribution of Δ' values and then the solutions are interpolated and convolved with the Maxwell-Boltzmann distribution of detunings to find $\bar{p}_e(\Delta, \tau)$. We also confirm the validity of this approach with a RE formalism that includes collisions through a Bhatnagar–Gross–Krook collision term (Sec. 3.6).

3.5 Experimental Validation

The LIF model for ions in a magnetized UCNP (Eqs. 3.7 and 3.38−3.40) can be fit to local LIF spectra to extract measurements of n, $v_{x,hyd}$, T_i, and P. In this section, we discuss how these plasma characteristics manifest in the spectrum qualitatively and use experimental data to validate the model's determination of laser couplings between the magnetic sublevels in Fig. 3.1b, which allows for the measurement of the electron-spin polarization that the ions inherit from the precursor atoms, and optical pumping of ions to states not driven by the LIF laser.

3.5.1 General Characteristics of LIF Spectra

Figure 3.4 demonstrates how the LIF spectra depend on the various plasma parameters for a plasma imaged a short time after photoionization ($t = 4\,\mu$s), when the plasma expansion velocity is still small, and at a later time ($t = 40\,\mu$s) when the plasma has developed significant expansion velocity in peripheral regions of the plasma. Through the Doppler effect, $v_{x,hyd}$ and T_i manifest as a mean shift and broadening of the single-particle lineshape, respectively, and the amplitude of the spectrum scales with n. The spin polarization P is derived from the relative strength of the Zeeman components associated with each ground state. These parameters are extracted from fits to the spectra with Eqs. 3.7 and 3.38−3.40.

At the field null $x \approx y \approx z \approx 0$ (Fig. 3.4(left)), where the LIF transitions are degenerate and hydrodynamic fluid velocity is small, the spectra are composed of a single spectral feature that is centered at the unperturbed $5s\,^2S_{1/2} - 5p\,^2P_{1/2}$ resonance frequency. The narrowing of the spectrum from $t = 4\,\mu$s to $t = 40\,\mu$s reflects decreasing ion temperature as the plasma expands, which is expected for adiabatic expansion under predominantly hydrodynamic conditions. In a non-central region

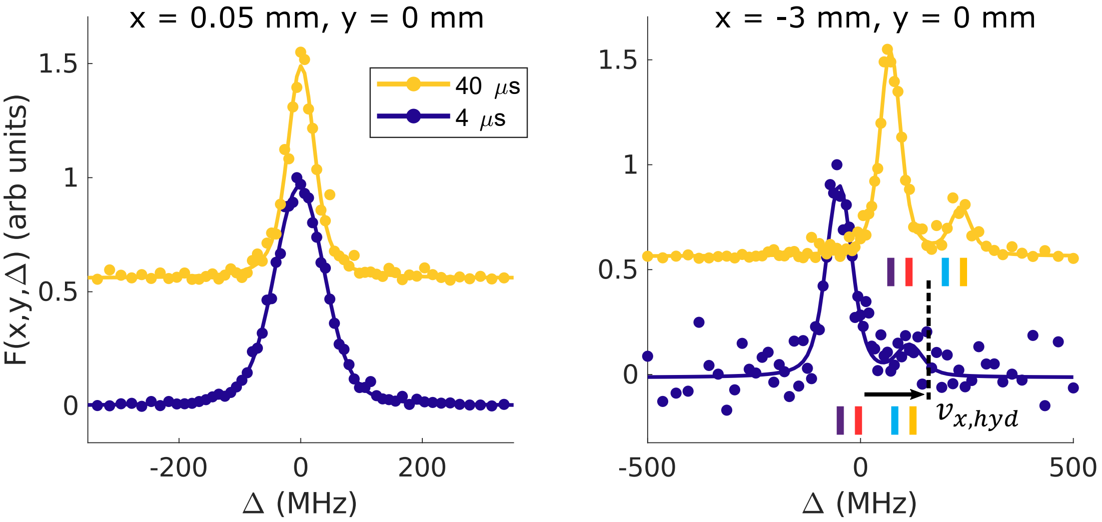

Figure 3.4 : LIF spectra of regions centered near the field null (left) and at $x = -3\,\text{mm}$, $y = 0\,\text{mm}$ (right) recorded with linear LIF-laser polarization for a UCNP with $T_e(0) = 40\,\text{K}$. The legend indicates time after photoionization and the spectra are normalized to the same amplitude and offset in the vertical scale for clarity. The spectral area scales with plasma density (n). Through the Doppler shift, the hydrodynamic fluid velocity ($v_{x,hyd}$) and ion temperature (T_i) manifest as a mean shift and broadening of the spectrum, respectively. Different Zeeman components are unresolved near the field null (left), but away from the plasma center (right) the splitting is resolved. The resonance positions of individual transitions are marked by ticks with color matching the corresponding transitions in Fig. 3.1b. Note that the Zeeman splitting is smaller for transitions initiating from the same ground state. The relative strengths of the resolved Zeeman components are sensitive to the electron-spin polarization of the ions. For these data, the majority of the ions occupy the field-aligned $m_j = +1/2$ ground state at the beginning of the excitation period, and transitions from this initial state are stronger. Polarization persists throughout the expansion. Lines are fits to spectra using Eqs. 3.7 and 3.38–3.40. Reused with permission from [86]. Copyright 2022 by the American Physical Society.

along the x axis (Fig. 3.4(right)), the transitions are Zeeman-shifted according to the local magnetic field strength. For the linear imaging polarization used for this data, the couplings for each σ transition are equal, and the asymmetry in the strength of the different Zeeman components indicates a high degree of spin polarization. Furthermore, at $t = 40\,\mu\text{s}$, the asymmetry is slightly lower, indicating that the ion spin polarization at this location has decreased with time. The fits with Eqs. 3.7 and 3.38−3.40 shown in Fig. 3.4b demonstrate that the polarization has decreased from $P = 0.73 \pm 0.07$ at $t = 4\,\mu$s to $P = 0.63 \pm 0.03$ at $t = 40\,\mu$s. $v_{x,hyd}$ increases with time, as indicated by the larger mean shift of the spectrum at later time.

3.5.2 Electron-Spin Polarization

Fig. 3.5 shows measurements of a UCNP after $26\,\mu$s of expansion in the biconic cusp field, recorded using LC, linear, and RC polarization (left, middle, and right, respectively). The 500 ns excitation period is sufficiently small so as to minimize the impact of optical pumping. The top row shows a spatial map of the spectral area (integrated over LIF-laser detuning), $F_{int}(x, y) = \int F_R(x, y, \Delta)d\Delta$ for regions (R) with size $\delta x = 0.1\,\mathrm{mm}$ and $\delta y = 0.2\,\mathrm{mm}$. For linear polarization, the σ transitions are driven equally and the integrated spectra are insensitive to P and the image spatial distribution matches that of the UCNP density distribution. However, for images recorded with LC and RC polarizations, the σ transitions are driven unequally. Imaging light with RC polarization will have a stronger σ^- drive for $x > 0$ and a stronger σ^+ drive for $x < 0$ because the local field direction reflects across the y axis (and vice versa for LC polarization). The asymmetry of the images for circular polarization shows that the ions predominantly occupy the field-aligned Zeeman ground state ($m_j = +1/2$ for quantization axis along the local field).

The bottom row of Fig. 3.5 shows $F_R(\Delta)$, the spectrum within a local region R defined by $x = 2.6 \pm 0.1$ mm and $y = 2.07 \pm 0.2\,\mathrm{mm}$. The solid yellow lines are fits of Eqs. 3.7 and 3.38−3.40 to the measured F_R. All three fits in Fig. 3.5 are constrained to use the same n, T_i, $v_{x,hyd}$, and P fit parameters. The good agreement with the data validates the calculation of Rabi couplings and strongly determines the

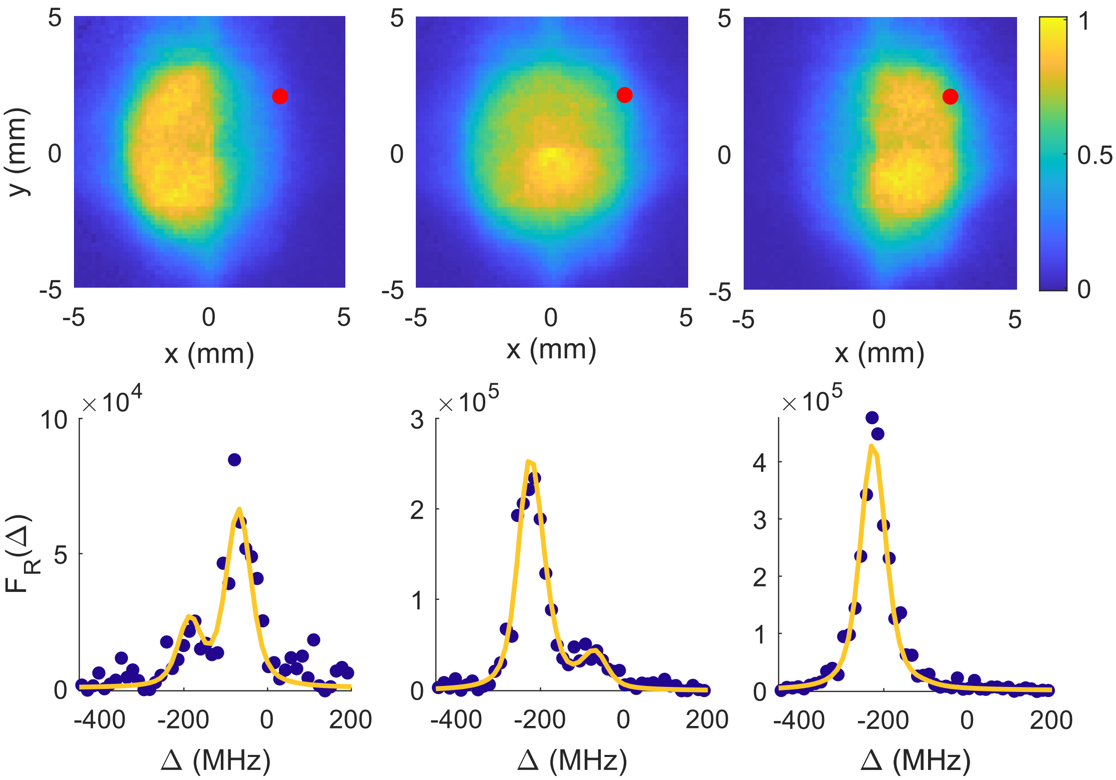

Figure 3.5 : LIF data for a magnetized UCNP with $T_e(0) = 20\,\mathrm{K}$ recorded at $t = 26\,\mu\mathrm{s}$ after photoionization with LC (left), linear (middle), and RC (right) lab-frame polarization of the imaging laser. The top row shows the integral of the fluorescence spectrum, $\int F_R(x, y, \Delta)d\Delta$, for laser detuning Δ with arbitrary units (the color bars are the same for each image). The image asymmetry along the x axis for LC and RC polarizations occurs because the $\sigma^{\pm}$ transitions are driven unequally, and is therefore reflective of the ion spin polarization. The bottom row plots the measured LIF spectrum (blue dots) averaged over a region (red circles) defined by $x = 2.6 \pm 0.1\,\mathrm{mm}$ and $y = 2.07 \pm 0.2\,\mathrm{mm}$, where the magnetic field amplitude is $42\,\mathrm{G}$, as a function of Δ. The data is well described by fits of Eqs. 3.7 and 3.38−3.40 (yellow lines), for which n, $v_{x,hyd}$, T_i, and P are constrained to be the same for all three imaging polarizations. The agreement validates the calculation of Rabi couplings for each imaging polarization (see appendix) and demonstrates the plasma is spin polarized. Reused with permission from [86]. Copyright 2022 by the American Physical Society.

polarization, which for this region is $P = 0.74 \pm .014$. The spin polarization of the ions is derived from the atomic gas from which the plasma is formed. The ${}^3P_2$ precursor atoms in the magnetic trap predominantly occupy the $m_j = +2$ magnetic sublevel

[71], in which both valence electrons are field-aligned. Following photoionization, the liberated electron carries away the angular momentum of the ionizing photon and the remaining valence electron is unperturbed, such that the ions inherit the electron-spin polarization from the precursor atoms.

Fig. 3.6 shows the extracted values of n (left) and P (right) from constrained fits to data such as in Fig. 3.5 for a plasma after $t = 26\,\mu$s of plasma expansion. The plasma is highly electron-spin polarized in peripheral regions where the magnetic fields are large, reaching up to $P \approx 0.8$. The spin polarization decreases for ions closer to the field null, which contains a pocket of weakly polarized ions with $P \approx 0.2$ within a 1 mm radius of the field null.

The strengths of the Zeeman components depend on the decomposition of the LIF-laser polarization in the coordinate frame of the local magnetic field and the ion spin polarization at the beginning of excitation. These two effects must be decoupled in order to obtain accurate measurements of P. This can be done using linear LIF-laser polarization anywhere the transitions are resolved, but is not possible in regions of small magnetic field because the asymmetry in the spectrum cannot be resolved. Imaging with LC and RC polarizations provides important information in regions of small magnetic field because the couplings to the σ transitions, and therefore, each ground state, are unequal. However, along the y axis where the transitions are unresolved, the couplings to the σ transitions are equal for all $\hat{\epsilon}$ and the spectra are insensitive to P. The impact of this issue is mitigated by choosing to define the grid of analysis regions so as to not have regions centered on $x = 0$, although central regions adjacent to the y axis are still more likely to yield poor fit results for P (Fig. 3.6(right)). For this reason, we do not show fit results for P within $|x| < 0.15\,$mm and $|y| < 2.5\,$mm.

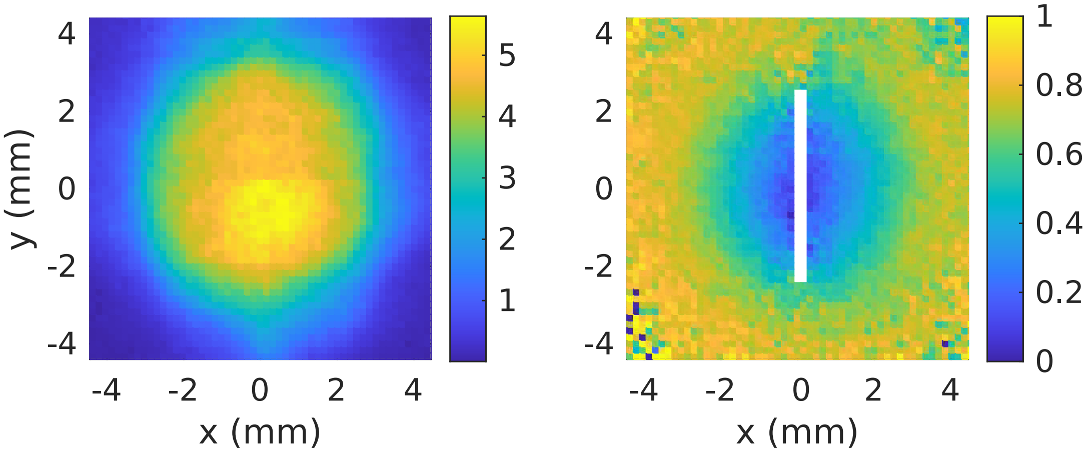

Figure 3.6 : Measurements of plasma density (n, left) and spin polarization (P, right) for a plasma with $T_e(0) = 20\,\mathrm{K}$ after $t = 26\,\mu\mathrm{s} \approx \tau_{exp}$ of plasma expansion, but before the onset of magnetic trapping. The plasma is highly electron-spin-polarized in peripheral regions where the magnetic fields are large, reaching up to $P \approx 0.8$. The spin polarization decreases for ions closer to the field null, which contains a pocket of weakly polarized ions with $P \approx 0.2$ within a 1 mm radius of the field null. The LIF model is insensitive to P within $|x| < 0.15\,\mathrm{mm}$ and $|y| < 2.5\,\mathrm{mm}$ for these plasma conditions, so fit results are not shown in these regions. Density is expressed in units of $10^8\,\mathrm{cm}^{-3}$. Reused with permission from [86]. Copyright 2022 by the American Physical Society.

Figure 3.7 demonstrates the ability to resolve P for regions that lie along $x = y$ for the same data shown in Fig. 3.6. The Rabi coupling to each Zeeman component in the x-y plane for a given polarization only depends on the angle that the local field subtends from the y axis, $\theta = \tan^{-1}(2x/y)$, and does not change with distance from plasma center along $x = y$. For RC polarization, the coupling to the σ^- transition is $\approx 9\times$ larger than the σ^+ coupling for $x > 0$ (and vice versa for LC polarization). Furthermore, the coupling of RC polarization to the σ^- transition is equal to the coupling of LC polarization to the σ^+ transition, so the asymmetry in signal strength recorded for the respective polarizations only depends on P. Near the field null (Fig. 3.7(left)), the signal strength for LC and RC polarization are nearly equal, which

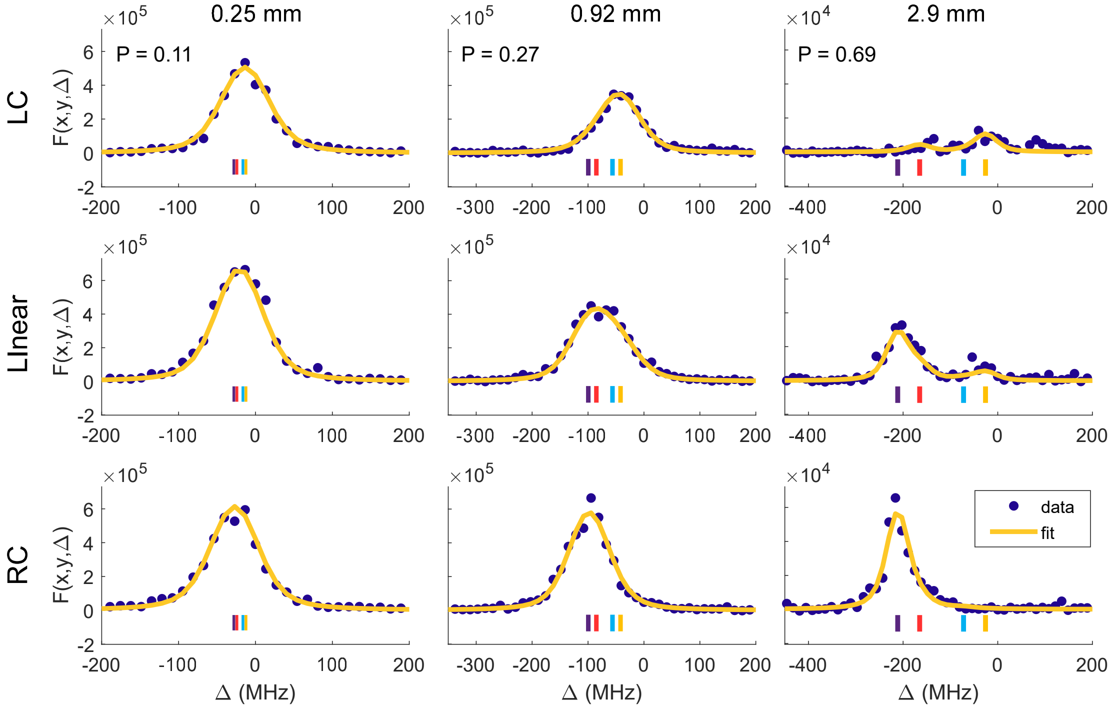

Figure 3.7 : Constrained fits of LIF data recorded with LC, linear, and RC laser polarization to Eqs. 3.7 and 3.38–3.40 for a UCNP with $T_e(0) = 20\,\mathrm{K}$ after $t = 66\,\mu\mathrm{s}$ of plasma evolution in regions that lie along $x \approx y$. The resonance positions of individual transitions are marked by ticks with color matching the corresponding transitions in Fig. 3.1. The x position along $x \approx y$ is indicated above each column. The subplots in each column share a common y axis. The relative strength of coupling to the σ transitions does not change with distance along $x = y$, so the decrease in relative signal strength for LC polarization as a function of x indicates increasing P.

results in a small value of $P = 0.11$. With increasing distance from the plasma center along $x = y$, the decreasing signal strength for LC polarization indicates an increase in P. The cause of the gradient in spin polarization is an open question and will be the subject of future study. However, the high degree of polarization away from the plasma center for $t = 26\,\mu\mathrm{s}$ of plasma expansion implies that the collisional spin-flip rate is low, which suggests that the polarization may provide valuable information for studying plasma flow and diffusion. The interrelated spatial and temporal dynamics of the plasma density and spin polarization are discussed in more detail in Chap. 5.

3.5.3 Optical Pumping

One important aspect of the RE model is that it accounts for the optical pumping of ions into states that are dark to the LIF laser. Optical pumping occurs when the scattering rate out of the two LIF ground states is unequal or when ions decay into the ${}^2D_{3/2}$ manifold, resulting in a decrease in the LIF signal collected per unit time during excitation. Differential scattering rates can develop any time the transitions are resolved or when the couplings to the σ transitions differ. For the experiments described here, optical pumping is greatest in regions along the x axis where the Zeeman components are resolved because this is where the LIF-laser intensity is the highest.

Fig. 3.8 demonstrates the impact of optical pumping in a magnetically trapped UCNP [50] in a central (left) and non-central (right) region probed 100 μs after plasma creation with linear laser polarization. At the field null, the scattering rate out of each LIF ground state is equal and ions are only lost to the off-resonant ${}^2D_{3/2}$ manifold, resulting in a 20% decrease of LIF signal per unit time for 2000 ns excitation compared to 250 ns excitation. Far from the field null, the transitions are resolved and the effects of pumping are more significant, with half the signal lost during the same excitation period due to optical pumping between LIF ground states. In both cases, optical pumping is only significant when the LIF laser is near resonance with an optical transition. The solid lines in Fig. 3.8 are fits to the local spectra and the density extracted from the fits to Eqs. 3.7 and 3.38−3.40 for each excitation time in the respective regions agree within 10% when optical pumping is accounted for.

Properly accounting for optical pumping is important for accurate measurements

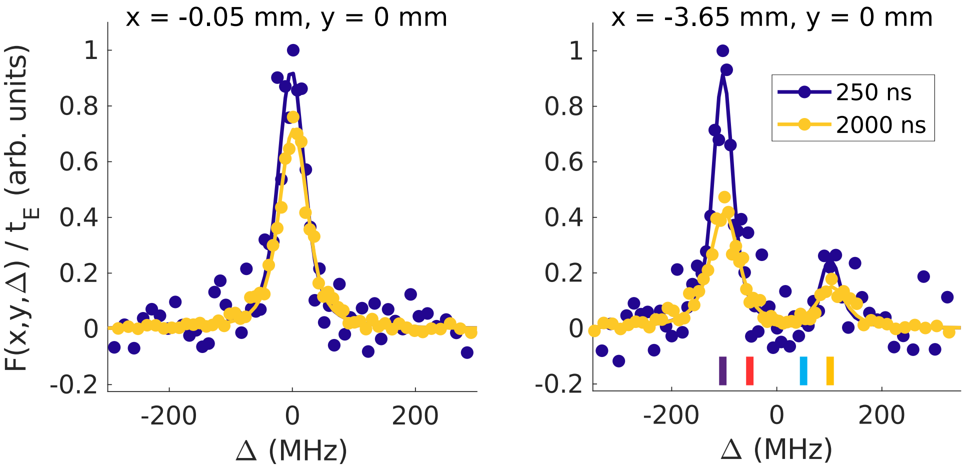

Figure 3.8 : LIF signal recorded 100 μs after plasma creation with linear laser polarization, illustrating optical pumping of ions into off-resonant states at the field null (left) and far from the field null (right) for a plasma with $T_e(0) = 40\,$K. Two different excitation times are used, as indicated in the legend, and the signal is divided by the excitation time. Near the field null, where the LIF transitions are degenerate, the signal loss on resonance with increasing excitation time reflects decay of excited ions into the off-resonant ${}^2D_{3/2}$ manifold. Away from the field null, where the LIF transitions are resolved, the loss of signal on each resonance feature is more severe due to optical pumping into the ground state that is not resonantly excited. Tick marks are the same as in Fig. 3.4. Reused with permission from [86]. Copyright 2022 by the American Physical Society.

of the spatial distribution of the plasma density. Optical pumping is dependent on the Rabi coupling to each Zeeman component, which varies with the local direction of the magnetic field and the local laser intensity, and whether or not the transitions are resolved. In Sec. 3.10, a steady-state model for $p_k(\tau)$ is introduced to describe LIF under excitation conditions where fewer than one photon is scattered per ion (i.e., in the validity of Fermi's golden rule). Using this FGR model to extract the plasma density under conditions where optical pumping is significant leads to warped spatial distributions of the plasma density, primarily near the field null where optical pumping only occurs due to decay to the ${}^2D_{3/2}$ state.

Figure 3.9 plots the density distributions along the x (top) and y (bottom) axes obtained by treating $p_k(\tau)$ with the FGR (left) and RE (right) models for the same data shown in Fig. 3.8. The density extracted with the FGR model display a systematic decrease of plasma density with excitation duration away from the plasma center because optical pumping among LIF ground states leads to significant loss of resonant signal. For $|x| \lesssim 0.75\,\mathrm{mm}$ ($B \lesssim 10\,\mathrm{G}$), the loss is less significant because ions are only pumped to the $^2D_{3/2}$ state and this manifests as a peak in the density distribution near the field null. Along the y axis, the systematic dependence of the density extracted with the FGR model is less significant. One reason for this is that the Zeeman shifts of π transitions, which are primarily driven near the y axis, are smaller than for the σ transitions. Combined with the weaker field gradient along y, the transitions are not sufficiently resolved for significant optical pumping in a much larger region than along x. Furthermore, the LIF-laser intensity decreases along the y axis, so the peak laser intensity does not drive the ions in regions where the transitions are resolved.

A similar study of optical pumping was conducted when imaging with LC polarization. However, unlike when imaging with linear polarization, the Rabi couplings to the σ transitions are unequal everywhere except for the y axis, so optical pumping can significantly alter the symmetry of the spectrum with respect to unperturbed resonance and the signal amplitude is dependent on both n and P. This is particularly relevant along the x axis, where the laser drives only a single σ transition. To avoid errors in density extraction due to proportionality of the signal strength with P, constrained fits for P were obtained, as discussed in Fig. 3.5 using the REs, and P was fixed to the value in the constrained measurements while fitting spectra taken with LC polarization for n.

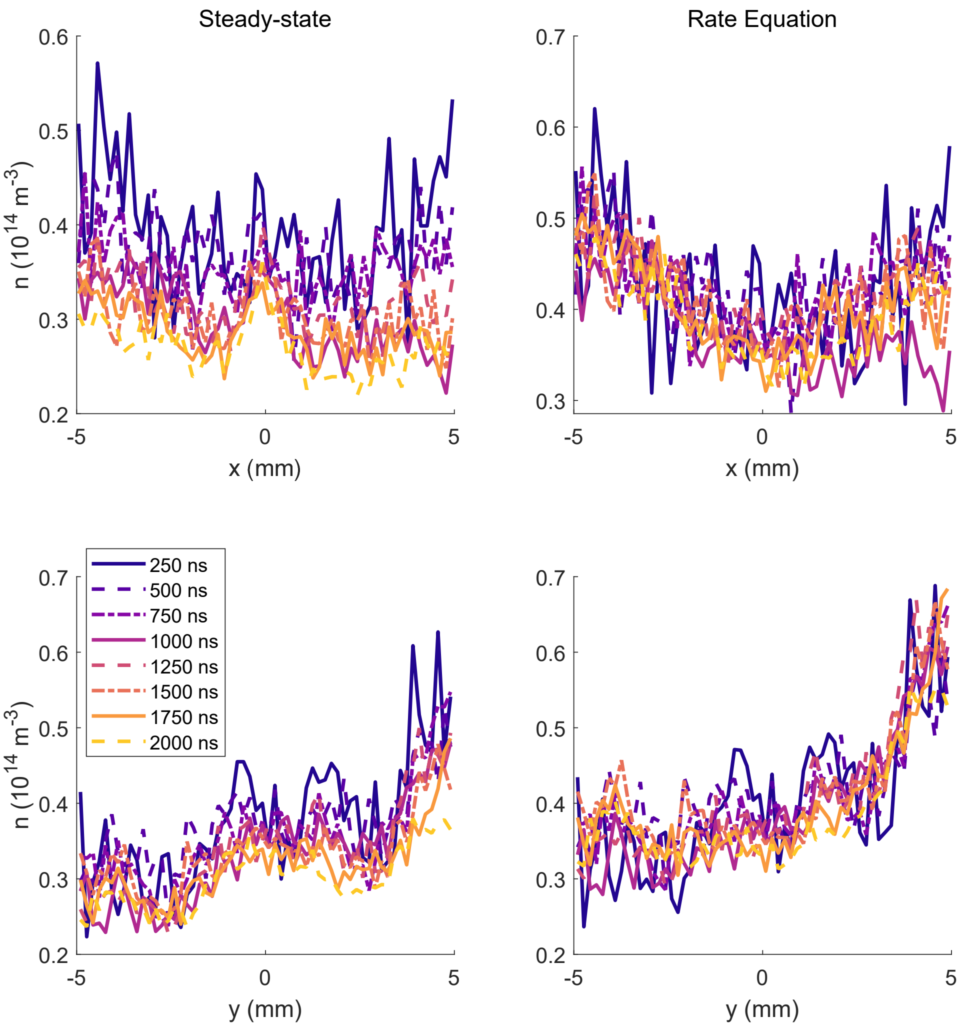

Figure 3.9 : Extraction of plasma density (n) along the x (top) and y (bottom) axes for the same data shown in Fig. 3.8 using fits to the fluorescence model in Eq. 3.7 with a steady-state model of ion state populations given by Eqs. 3.48 (left) and the rate equation model given by Eqs. 3.38−3.40 (right). The legend indicates the excitation duration. The density extracted by the steady-state model, which neglects optical pumping between LIF ground states, displays a systematic decrease with excitation duration. No such dependence is observable for the density extracted by the RE model, providing further validation that of the RE approach. The effects of optical pumping are greatest along the x axis for $|x| > 0.75\,\mathrm{mm}$ because the transitions are resolved and the laser intensity is highest along the x axis.

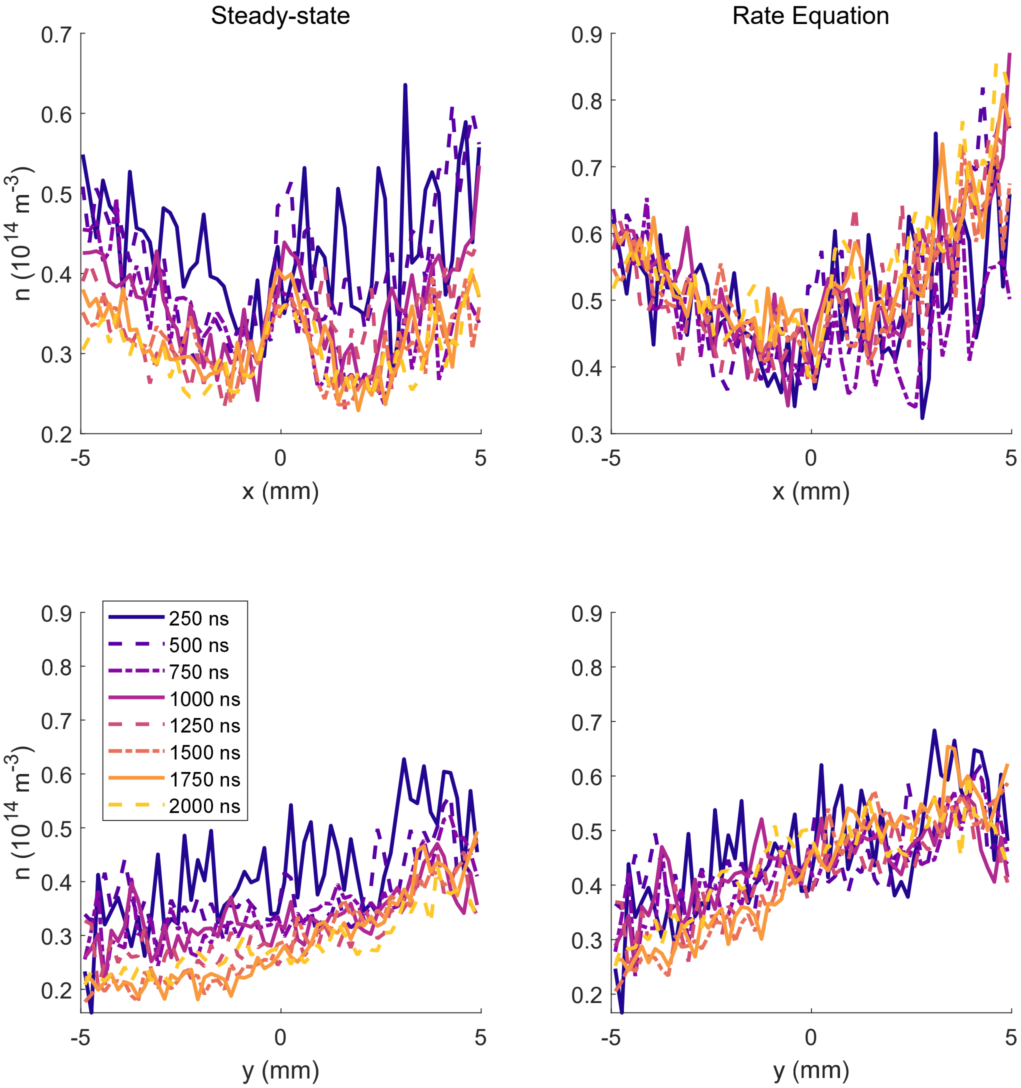

Figure 3.10 : Extraction of plasma density (n) along $y = 0.52\,\mathrm{mm}$ (top) and $x = -2\,\mathrm{mm}$ (bottom) using fits to the fluorescence model in Eq. 3.7 with a steady-state model of ion state populations given by Eqs. 3.48 (left) and the rate equation model given by Eqs. 3.38–3.40 (right) for similar conditions as in Fig. 3.9, except using LC polarization. The legend indicates the excitation duration.

Figure 3.10 demonstrates the validity of the REs for LC polarization for $y = 0.52\,\mathrm{mm}$ (top) and $x = -2\,\mathrm{mm}$ (bottom) for a UCNP with similar conditions to Fig. 3.9. Here, we avoid showing transects along either axis to avoid including regions

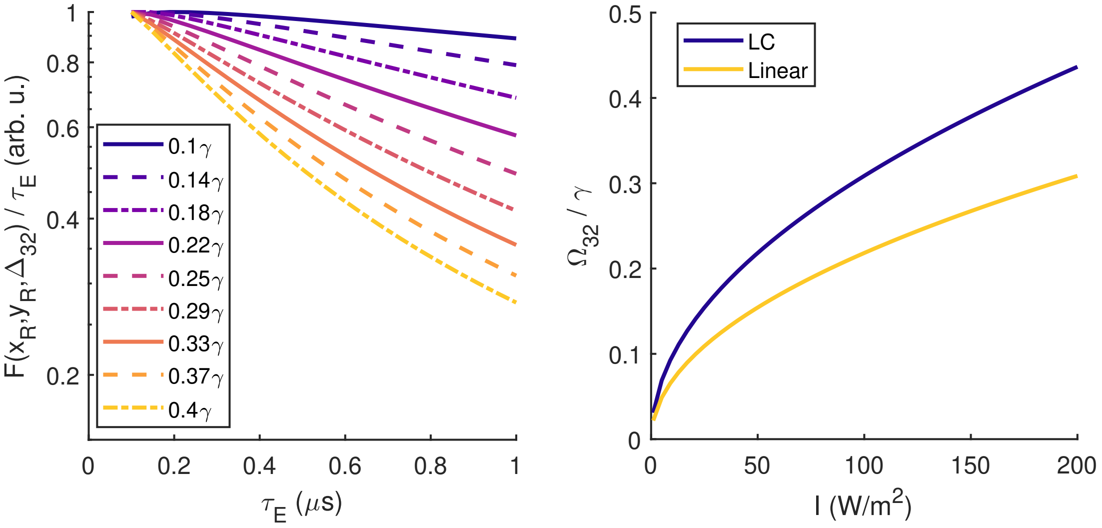

Figure 3.11 : Characterizing the severity of optical pumping during LIF. (left) Systematic loss of resonant LIF signal per unit excitation for the same region (R) as in Fig. 3.8(right). The loss increases with the Rabi coupling to the σ^- transition ($\Omega_{3\leftarrow2}$, indicated in the legend) and the excitation duration τ_E. (right) Scaling of $\Omega_{3\leftarrow2}$ with the LIF-laser intensity (I) along the x axis. The coupling is greater for LC polarization due to the way the LIF-laser polarization projects onto the local magnetic field.

where P cannot be reliably measured. For $y = 0.52\,\mathrm{mm}$, where the Rabi coupling to the σ transitions for LC polarization (σ^+ for $x > 0$ and σ^- for $x < 0$) are stronger than for linear LIF-laser polarization, the systematic decrease with excitation duration for the density extracted by the FGR model is slightly larger than for linear polarization. Near the y axis, the σ transitions are driven equally and the states are not sufficiently resolved to allow for optical pumping. Along $x = -2\,\mathrm{mm}$, the systematic decrease of density with excitation duration for the FGR model does not change significantly with y position because the transitions are resolved everywhere. Once again, the density extracted with the REs (Fig. 3.10(right)) do not display the systematic dependence observed in the density extracted with the FGR model.

For experiments seeking to avoid significant optical pumping, it is helpful to quantify the loss of resonant LIF signal per unit excitation, which is the greatest along the x axis where the transitions are most easily resolved and the Rabi coupling is the largest ($x < 0$ for LC and $x > 0$ for RC). Figure 3.11(left) plots $F(x_R, y_R, \Delta_{32})/\tau_E$ as a function of τ_E for several values of $\Omega_{3\leftarrow 2}$, as indicated in the legend, for the same region (R) shown in Fig. 3.8(right). For context, Fig. 3.11(right) plots $\Omega_{3\leftarrow 2}$ as a function of the LIF-laser intensity (I). The coupling for circular LIF-laser polarization is higher than linear polarization along the x axis due to the way it projects onto the local magnetic field. For the data shown in Fig. 3.5, which was taken with an effective laser intensity $\bar{I} = 85\,\mathrm{W/m^2}$, the resonant signal loss per unit excitation was 18(30)% for linear(circular) polarization, respectively.

3.6 Collisional Effects During LIF

Rapid velocity-changing collisions (VCCs) are a hallmark of UCNPs and strongly coupled plasmas in general [34, 57], and can influence the time evolution of internal quantum states of laser-driven systems. VCCs are strong collisions that result in velocity changes of $\sim v_{th} = \sqrt{k_B T/m}$, for an ensemble with temperature T. On average, each collision effectively randomizes ion velocities within the thermal distribution and causes non-equilibrium velocity distributions to equilibrate towards a Maxwellian. The VCC rate (μ) in plasmas is proportional to the ion plasma oscillation frequency $\omega_{pi} = \sqrt{ne^2/m_i\epsilon_0}$ and in [34] was measured to be $\sim 0.2\omega_{pi}$ for $\Gamma \sim 3$, which is typical for UCNPs following DIH [49]. In [57], a combined molecular-dynamics and quantum-trajectories (MDQT) code was developed to describe laser cooling of the ions in a UCNP and VCCs were shown to collisionally suppress the development of velocity-dependent coherent dark states.

Coherent effects make a minimal impact on LIF of UCNPs because the coherences equilibrate in a few $\gamma^{-1} \approx 7\,\mathrm{ns}$, which is much faster than typical excitation times of a few 100s of ns. However, VCCs can become important during LIF under excitation conditions where the velocity dependence of $p_k(v_x, \tau)$ for the driven LIF ground state becomes non-Maxwellian. This typically occurs under conditions where optical pumping is significant and the Doppler width $\sigma_D = k\sqrt{k_B T_i/m_i}$ exceeds the width of the excitation rate γ_{tot}. Optical pumping starts to occur when many photons are scattered per ion ($R_{eg}\tau_E > 1$). Under these conditions, the resonant portion of the driven LIF ground state's velocity distribution is depleted as those ions are pumped into off-resonant states, causing the measured LIF signal to decrease with τ, as characterized in Fig. 3.11. In the absence of collisions, the off-resonant ions in the driven ground state will remain dark to the imaging laser. However, if VCCs occur rapidly enough, the velocity distribution for each state will equilibrate towards a Maxwell-Boltzmann distribution during LIF, effectively increasing the measured signal by providing optical access to the nominally off-resonant portion of the velocity distribution.

The effects of collisions on LIF were quantified by adapting the MDQT code in [57] to simulate $\bar{p}_k(\tau)$ for LIF of a magnetized UCNP [86]. The MD portion of the code is a particle-in-cell method that evolves the positions and velocities of ions interacting via the Yukawa force. The QT portion of the code evolves the wave function $|\psi(t)\rangle$ for each ion under the influence of a non-Hermitian effective Hamiltonian that includes the closed system Hamiltonian for LIF (given by Eq. 3.43) and spontaneous emission between states driven by the LIF laser (Fig. 3.1b). Decay from the excited ${}^2P_{1/2}$ state to the metastable ${}^2D_{3/2}$ dark state is grafted onto the QT formalism through the inclusion of a single basis state $|5\rangle$, which states $|3\rangle$ and $|4\rangle$ can decay to with rate γ_D. This approach, rather than including all seven magnetic sublevels, is justified because the LIF laser does not couple to this manifold.

The MDQT simulations of $\bar{p}_k(\tau)$, computed as the ensemble-averaged diagonal elements of the density matrix $\rho(\tau) = |\psi(\tau)\rangle\langle\psi(\tau)|$, were found to be in good agreement with the REs in Eq. 3.40 modified to include a Bhatnagar-Gross-Krook collision term (Fig. 3.12)

$$\frac{\partial \rho_k(v_x,\tau)}{\partial t} = -\mu[p_k(v_x,\tau) - \bar{p}_k(\tau)G(v_x)], \tag{3.41}$$

which describes the equilibration of $p_k(v_x,\tau)$ towards a Maxwellian with collisional relaxation rate μ, which is extracted from MD simulations in [95] that were experimentally verified for strongly coupled plasmas in [34]. The value of μ depends on n and T_i. For a plasma with $T_i = 1\,\mathrm{K}$, the ion-ion collision rate is $\mu = 5.2 \times 10^4\,\mathrm{s}^{-1}$ for $n = 10^7\,\mathrm{cm}^{-3}$ and $\mu = 1.94 \times 10^7\,\mathrm{s}^{-1}$ for $n = 10^{11}\,\mathrm{cm}^{-3}$.

Figure 3.12 compares MDQT simulations of the instantaneous fluorescence signal per unit density and unit time (dF/dt) with predictions from the collisional RE (REK) model as a function of plasma density (indicated in the legend) for a plasma with $T_i = 1\,\mathrm{K}$ in a magnetic field of 15 G that is imaged with $I = 100\,\mathrm{W/m^2}$ on resonance with the π transition out of state $|2\rangle$. At early excitation times ($\tau < 100\,\mathrm{ns}$), optical pumping is negligible and there is no density dependence. At later times during excitation, collisional effects manifest as an enhanced fluorescence signal compared to the collisionless model ($n = 0$) for higher plasma densities.

Collisions are computationally challenging to incorporate in the LIF fit model, so it is best to avoid their influence on LIF entirely by choosing the effective LIF-laser intensity ($\bar{I}$) and excitation duration (τ_E) to minimize the impact of optical pumping. Figure 3.13 plots the relative error between the peak plasma signal with (F_{REK}) or without (F_{RE}) the inclusion of collisions for a UCNP with $n = 5 \times 10^9\,\mathrm{cm}^{-3}$ that is imaged with $\bar{I} = 100\,\mathrm{W/m^2}$ as a function of position along the x axis for several

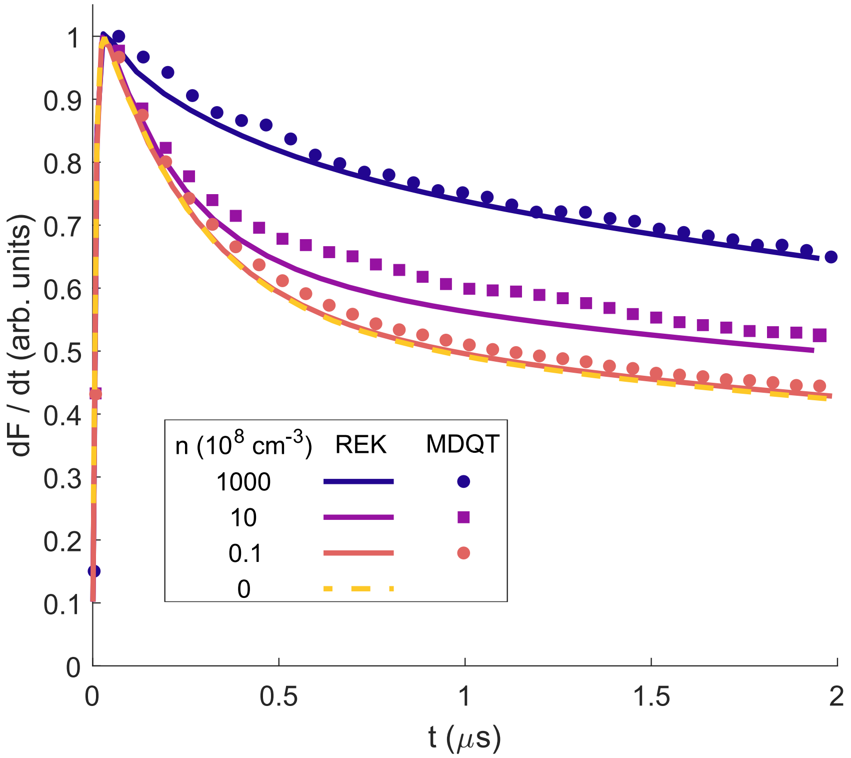

Figure 3.12 : Effect of collisions on instantaneous fluorescence signal per unit density and unit time (dF/dt) as a function of time during LIF (τ) for a plasma with ion temperature $T_i = 1\,\mathrm{K}$ in a magnetic field of 15 G. Under these conditions, the width of the velocity distribution is broader than the excitation rate. The MDQT simulations (markers) and solutions to the collisional rate equations (REK, lines) are in good agreement. For $\tau < 100\,\mathrm{ns}$, optical pumping has yet to occur and there is no density dependence. At later times, collisional effects provide optical access to the nominally off-resonant portion of the velocity distribution and manifest as an enhancement of the fluorescence signal. The legend indicates the plasma density, n.

values of τ (left, $T_i = 2\,\mathrm{K}$) and T_i (right, $\tau_E = 2\,\mu\mathrm{s}$), as indicated in the legend. The collision rate is highest early in the plasma lifetime because the density decreases with expansion. The plasma density does not exceed the density used in Fig. 3.12 for data shown in this thesis, so these results represent an upper limit on the influence of collisions.

As expected, collisional effects generally increase with τ and T_i and are lowest near

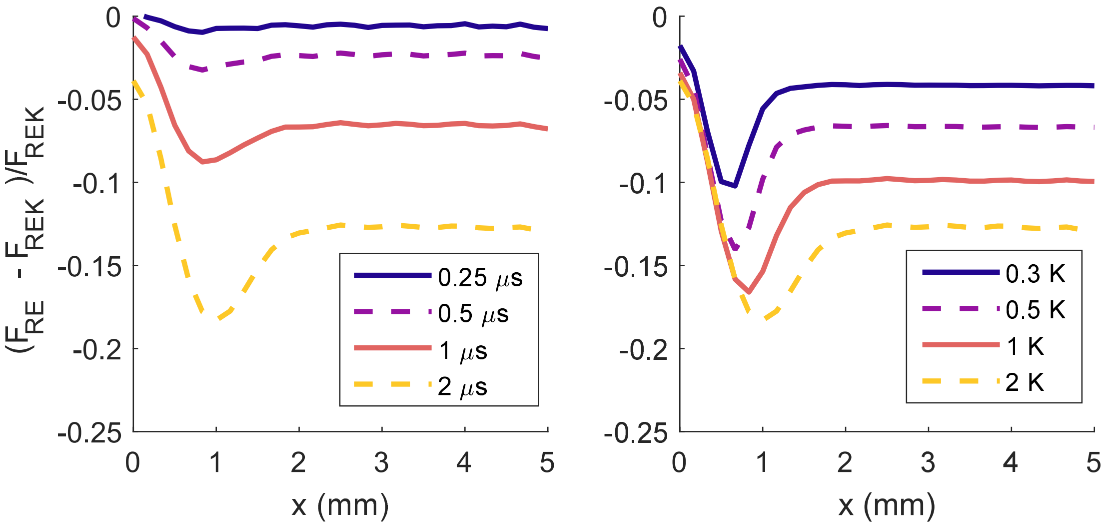

Figure 3.13 : Relative error in the peak LIF signal for population transfer models including (F_{REK}) and neglecting (F_{RE}) collisions in a plasma with $n = 5 \times 10^9\,\mathrm{cm}^{-3}$ that is imaged with $\bar{I} = 100\,\mathrm{W/m}^2$. The discrepancy is plotted as a function of position along the x axis for several values of τ_E (left, $T_i = 2\,\mathrm{K}$) and T_i (right,$\tau_E = 2\,\mu\mathrm{s}$).

the center, where ions are only optically pumped through the slow leak to the ${}^2D_{3/2}$ state. At large distances from the plasma center ($x \gtrsim 2\,\mathrm{mm}$), where the transitions are fully resolved, the error displays no dependence with x position. However, at intermediate positions ($x \approx 0.5 - 1\,\mathrm{mm}$), collisional effects are the largest because the Zeeman components are partially resolved so as to allow for optical pumping, but the splitting is sufficiently small that the thermal distribution allows for both σ transitions to be driven simultaneously. In this case, collisions influence LIF for longer periods because the resonant portion of the velocity distribution can never be fully depleted; the excited state populations reach an equilibrium value that is enhanced by collisions (as is the case in Fig. 3.12). For the conditions in Fig. 3.13(left), collisions lead to no larger than a 3.2% enhancement of the LIF signal for $\tau_E < 500\,\mathrm{ns}$. For data shown in this thesis, the plasma density and ion temperature are smaller than in Fig. 3.13 in the partially resolved region where collisions are most important, providing further justification for the neglect of collisions.

3.7 Justifying the Use of an Effective LIF-Laser Intensity

The LIF spectrum model given by Eq. 3.7 computes the spectrum within a volume element $V \approx \delta x \delta y w$, where $A = \delta x \delta y$ is a user-defined analysis area within the x-y plane and w is the $1/e^2$ diameter of the LIF-laser along the z axis. Eq. 3.7 makes the simplifying approximation of evaluating all quantities except for the LIF-laser intensity at the center of the volume V in order to avoid the significant computational overhead that spatial integration would impose in order to account for variation of $\vec{B}$ and I across the local volume element. A is chosen to be sufficiently small such that variation of quantities within the x-y plane can be neglected. However, the imaging process inherently averages over the camera line of sight and significant variation of I along the z axis cannot be avoided. The most significant impact of this averaging is in the amount of optical pumping the model predicts. In order to account for this variation, Eq. 3.7 uses an effective laser intensity $\bar{I} = 0.45 I_{max}$ that is chosen to minimize discrepancy between Eq. 3.7 and the following realistic model that integrates over the camera line of sight.

$$F(x, y, \Delta) = A\, C'_{p\rightarrow s} \int_0^{\tau_E} d\tau \int_{-\infty}^{\infty} dz \sum_{e,g} n\bar{p}_e(z)\gamma_{eg}\xi_{eg}, \tag{3.42}$$

where $p_e(z)$ is explicitly stated as a function of z in order to emphasize that the variation of I and $\vec{B}$ are accounted for. The photon-to-signal conversion factor in Eq. 3.42 is denoted with a prime to differentiate it from that of Eq. 3.7. The photon-to-signal conversion factors in Eq. 3.42 ($C'_{p\rightarrow s}$) and Eq. 3.7 ($C_{p\rightarrow s}$) are chosen to match predictions of these calculations to experimentally observed signal levels at small exposure time and with no external magnetic fields so as to avoid the effects of optical pumping. The density assumed for this procedure is determined by a density calibration that relies on the density dependence of DIH [41]. $C_{p\rightarrow s}$ and $C'_{p\rightarrow s}$ differ because the two equations calculate the volume contributing to the signal differently.

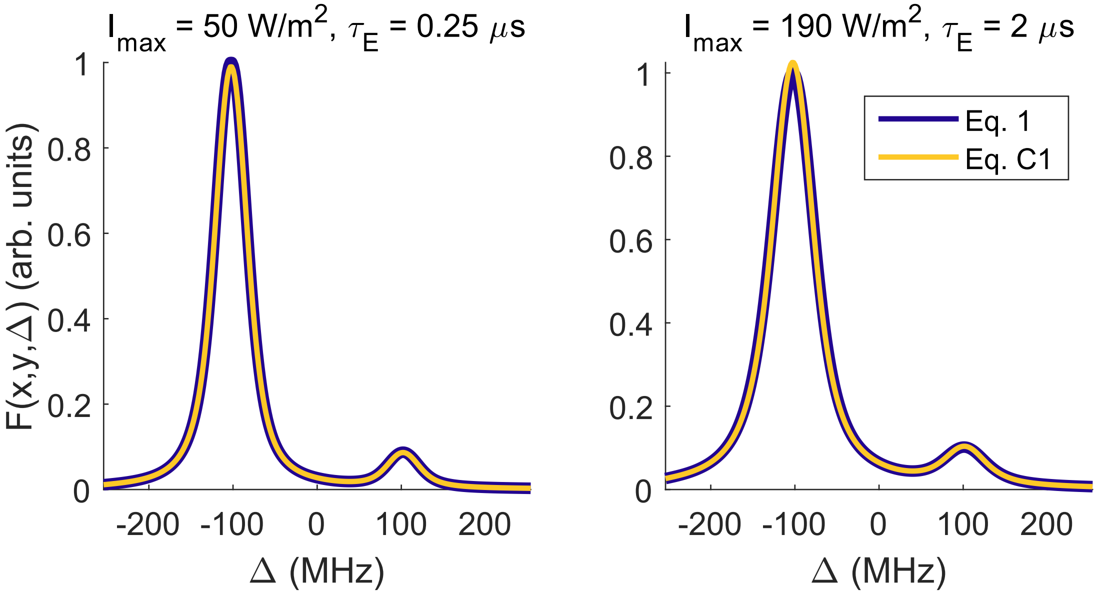

Figure 3.14 : Comparison of the LIF models given by Eq. 3.7 (assumes $z = 0$ with an effective LIF-laser intensity) and Eq. 3.42 (realistic model with spatial averaging) under excitation conditions where optical pumping is minimal (left) and significant (right) for the same spatial region and ion temperature (300 mK) as in Fig. 3.8b. The two models are in good agreement for both excitation conditions and the relative error in the peak signal is less than 2.5%. The blue line is slightly thicker in order to improve visibility.

Fig. 3.14 compares Eqs. 3.7 and 3.42 for excitation conditions where optical pumping is minimal (left) and significant (right) for the same spatial region and ion temperature (300 mK) as in Fig. 3.8b. $I_{max} = 50\,\mathrm{W/m^2}$ is typical for the edges of the CCD camera near $|y| \approx 5\,\mathrm{mm}$ and $I_{max} = 190\,\mathrm{W/m^2}$ is the maximum intensity used in this work. The models are found to be in good agreement for both excitation conditions with relative error less than 2.5%. In the absence of optical pumping, the agreement is expected and is independent of the choice of $\bar{I}$ due to the external density calibration. $\bar{I}$ is chosen to minimize the difference between the two models when optical pumping is significant. For a given value of $\bar{I}$, the discrepancy between the two models will vary slightly with ion temperature because as the temperature increases the ensemble-averaged scattering rate decreases slightly. The variation with temperature is greatest when optical pumping is significant. For the conditions of greatest optical pumping in this work (Fig. 7(right) and Fig. 3b) and the chosen value of $\bar{I}$, the discrepancy between the two models varies from 0.92% at $T_i = 1\,\mathrm{K}$ to 4.37% at $T_i = 100\,\mathrm{mK}$. Across the relevant parameter regime for this experiment, the discrepancy does not exceed 5% and is typically less than 2.5%.

3.8 Neglecting Coherent Effects During Population Transfer

The methods from Sec. 3.3, which model LIF for a two-level ion in a magnetic field, can be extended to describe LIF for Sr^+. The states coupled by the LIF laser are shown in Fig. 3.1b and the Hamiltonian can be formed in the rotation wave approximation analogously to that in Eq. 3.29:

$$\begin{aligned}\tilde{H}_{LIF} = &\sum_k \hbar\delta_k |k\rangle\langle k| - \sum_e \hbar\Delta' |e\rangle\langle e| \\ &- \frac{\hbar}{2}\sum_{e,g}\left[\Omega_{e\leftarrow g}|e\rangle\langle g| + \Omega^\star_{e\leftarrow g}|g\rangle\langle e|\right],\end{aligned} \tag{3.43}$$

where e and g indexes the excited ($|3\rangle, |4\rangle$) and ground ($|1\rangle, |2\rangle$) states, respectively, and k indexes all four states.

The evolution of the density matrix is described by the following set of equations, which result from evaluating the master equation (ME, Eq. 3.30) for H_{LIF} in Eq. 3.43:

$$\dot{\rho}_{ee} = -\frac{i}{2}\sum_g (\Omega^\star_{e\leftarrow g}\rho_{eg} - \Omega_{e\leftarrow g}\rho_{ge}) - (\gamma + \gamma_D)\rho_{ee} \tag{3.44}$$

$$\dot{\rho}_{gg} = +\frac{i}{2}\sum_e (\Omega^\star_{e\leftarrow g}\rho_{eg} - \Omega_{e\leftarrow g}\rho_{ge}) + \sum_e \gamma_{eg}\rho_{ee} \tag{3.45}$$

$$\dot{\rho}_{eg} = (i\Delta_{eg} - (\gamma + \gamma_D)/2)\rho_{eg} + \frac{i\Omega_{e\leftarrow g}}{2}(\rho_{gg} - \rho_{ee}) + \frac{i}{2}(\Omega_{e'\leftarrow g}\rho_{ee'} - \Omega_{eg'}\rho_{g'g}), \tag{3.46}$$

where $g' \neq g$ and $e' \neq e$ (for $\dot{\rho}_{32}$, $\rho_{ee'} = \rho_{34}$) and the equations for the coherence between the two excited ($\rho_{ee'}$) and ground ($\rho_{gg'}$) states are not explicitly listed.

These equations are similar to those for the two-level ion (Eqs. 3.31−3.33), where the population transfer between state $|g\rangle$ and $|e\rangle$ is governed by terms of the form $\Omega^\star_{e\leftarrow g}\rho_{eg} - \Omega_{e\leftarrow g}\rho_{ge}$ and the diagonal elements consist of a superposition of the transfer and decay terms. Decay from the ${}^2P_{1/2}$ state to the ${}^2D_{3/2}$ is grafted on through additional loss of population and coherence at a rate γ_D. Aside from this, the only other difference is the last term in Eq. 3.46, which results from the coherence terms $\rho_{ee'}$ and $\rho_{gg'}$, respectively.

The REs given by Eq. 3.40 can be derived from Eqs. 3.44−3.46 by neglecting the coherence terms between states not directly coupled by the LIF laser ($\rho_{ee'} = \rho_{gg'} = 0$) in the limit $t \gg \gamma^{-1}$ ($\dot{\rho}_{eg} = 0$). These assumptions lead to small systematic errors in the instantaneous fluorescence signal dF/dt at early times during excitation ($\tau \approx 10\gamma^{-1}$), as demonstrated in Fig. 3.15 for LIF in a magnetic field of 15 G with $\Omega_{3\leftarrow 2} = 0.22\gamma$. When the LIF laser is on resonance, the fluorescence signal is overestimated by the REs for $\tau < 10\gamma^{-1}$, but subsequently underestimates the signal as the RE solutions relax towards the MEs over the next $\tau \approx 60\gamma^{-1} \approx 500$ ns. In contrast, when the laser is off resonance, the REs fail to capture rapid oscillations of the state populations for $\tau < 10\gamma^{-1}$, which results in a systematic underestimation of the LIF signal.

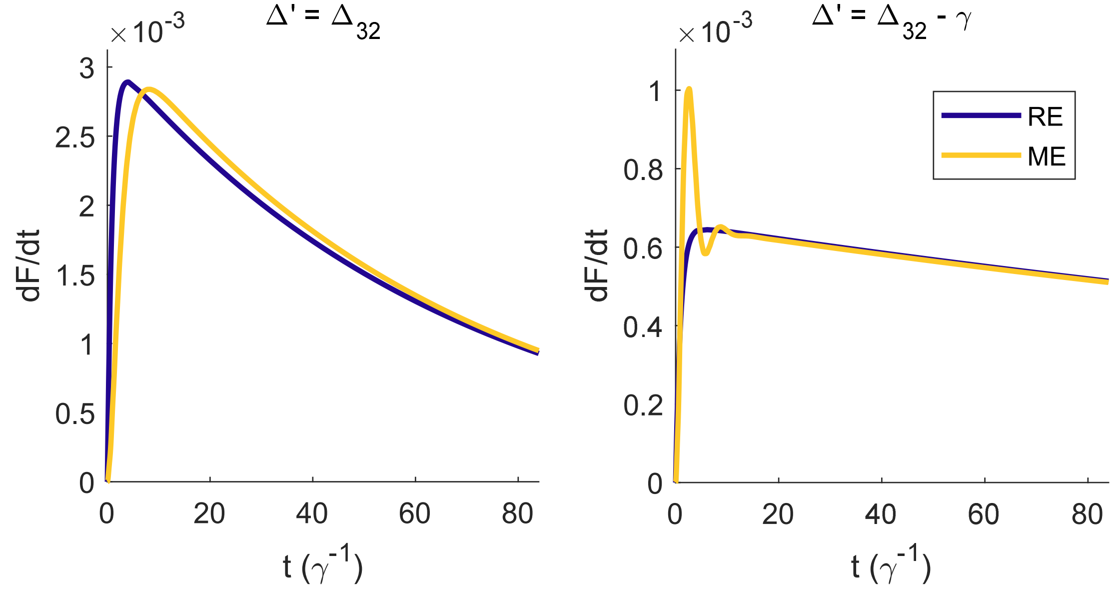

Figure 3.15 : Time evolution of the instantaneous fluorescence signal (dF/dt) for a single ion during LIF in a magnetic field of 15 G with $\Omega_{3\leftarrow 2} = 0.22\gamma$. When the LIF-laser is resonant with the transition (left), the rate equations (REs) overestimate the LIF signal for $t < 10\gamma^{-1}$ compared to the exact treatment by the master equation (ME), but overestimate the signal afterward and the two models converge together at $\approx 60\gamma^{-1} \approx 500$ ns. Off resonance (right), the LIF signal is underestimated by the REs because they fail to capture rapid oscillations of the state populations in the first $10\gamma^{-1} \approx 100$ ns of evolution.

The systematic errors resulting from this treatment of the coherences are observed through the time-integrated fluorescence signal, F. Fig. 3.16 compares the LIF signal that results from treating the state populations with the rate equations (F_{RE}) and the master equation (F_{ME}) as a function of Δ' for several values of the excitation duration. Here, the Rabi coupling to each transition is $\Omega = 0.22\gamma$. As discussed in Fig. 3.15, the LIF signal is overestimated near resonance of each Zeeman component, which is indicated by the markers with color corresponding to the transitions in Fig. 3.1, but is underestimated away from resonance. The discrepancy is largest for short excitation ($\tau_E = 250$ ns), but decreases with excitation time because the RE and ME solutions

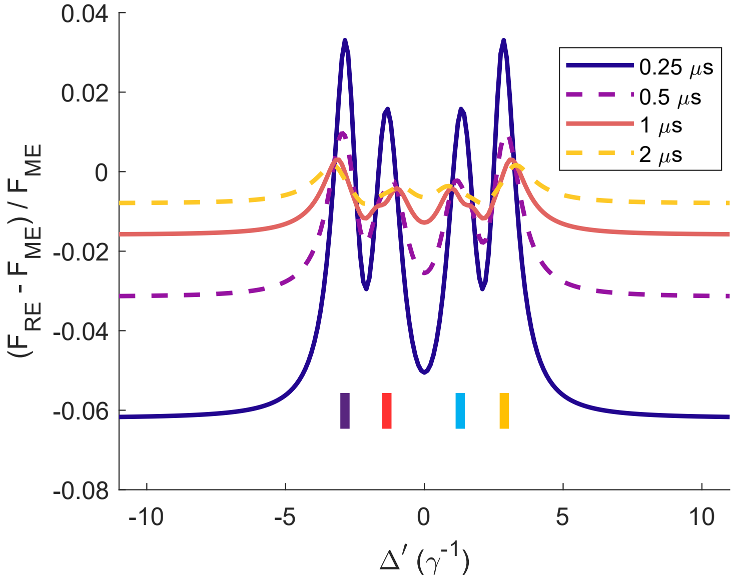

Figure 3.16 : Comparison of the LIF signal predicted by Eq. 3.7 derived by treating the state populations with the rate equations (F_{RE}) and optical Bloch (F_{ME}) for a single ion as a function of the Doppler-shifted laser detuning Δ' for several values of the excitation duration, as indicated by the legend. The markers indicate the resonance position of the transition of corresponding color in Fig. 3.1, which are driven equally here with $\Omega = 0.22\gamma$ in a magnetic field of 30 G. The LIF signal is overestimated by the rate equations near resonance of each Zeeman component, but is underestimated away from resonance.

converge for $t >> \gamma^{-1}$. The error when resonant with the σ transitions (purple for the σ decay channel are larger. The levels of error shown in Fig. 3.16 do not change significantly with the coupling to the transition for $\Omega < 1$, as is the case for all data shown here.

3.9 Measuring the Magnetic Field Amplitude

The local magnetic field strength can be measured using LIF by additionally setting the field amplitude (B) as a free parameter in the constrained fits of Eqs. 3.7 and 3.38−3.40 to LIF data recorded with LC, linear, and RC polarization, as described in Fig. 3.5. Accurate measurements of B can be obtained anywhere that the Zeeman components are resolved or where the spectra are asymmetric with respect to $\Delta' = 0$ (i.e., when $P \neq 0$ or when the couplings to the σ transitions are unequal). The latter condition arises because both B and T_i will symmetrically broaden the spectrum when the Zeeman components are symmetric and unresolved. Thus, the spatial region where B cannot be resolved roughly corresponds to where the model is insensitive to P ($|x| < 0.15\,\mathrm{mm}$ and $|y| < 2.5\,\mathrm{mm}$; Fig. 3.6).

A UCNP after the onset of magnetic trapping ($t \gtrsim 2\tau_{exp}$) is best suited for local measurements of B because the ion temperature has decreased due to adiabatic cooling, which allows the transitions to be resolved by smaller fields, and the plasma has expanded to provide sufficient LIF signal in peripheral regions of the camera FOV. Fig. 3.17 shows constrained fits for n (left) and B (middle) for a magnetized UCNP with $T_e(0) = 20\,\mathrm{K}$ after $t = 110\,\mu\mathrm{s} \approx 4\tau_{exp}$ of evolution. The plasma pressure (nk_BT_e) is significantly smaller than the pressure of the external quadrupole magnetic field ($B^2/2\mu_0$), so plasma flow is not expected to influence the local magnetic field. The field measurements were fit to the linear approximation of the quadrupole magnetic field given by Eq. 2.2 to determine the field gradient along the symmetry axis (B'). Measurements of B within $|x| < 0.15\,\mathrm{mm}$ and $|y| < 2.5\,\mathrm{mm}$ are unreliable and were not used for this fit. The linear approximation (B_l) is found to be in good agreement with the experimental measurements, as indicated by the fit residual $B_l - B$ in Fig. 3.17(right). Six independent measurements of the field gradient were obtained by fitting LIF data for the same plasma conditions in Fig. 3.17 for evolution times ranging from $t = 52 - 176\,\mu\mathrm{s}$, which yielded a value of $B' = 151.5 \pm 0.2\,\mathrm{G/cm}$.

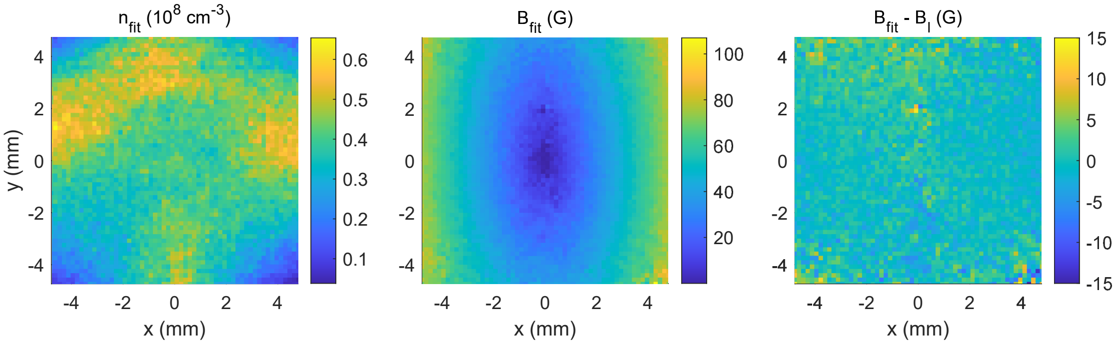

Figure 3.17 : Experimental measurement of the local magnetic field amplitude (B) using constrained fits to Eqs. 3.7 and 3.38−3.40 for LIF data recorded with LC, linear, and RC polarization (as in Fig. 3.5) for a magnetized UCNP with $T_e(0) = 20\,\mathrm{K}$ at $t = 110\,\mu\mathrm{s}$ after photoionization. The experimental measurements were found to be in good agreement with the linear approximation to the quadrupole magnetic field (B_l) given by Eq. 2.2, as demonstrated by the fit residual $B_l - B$ (right).

3.10 A Steady-State Model for LIF

Computational efficiency was a major consideration during the development of the RE model introduced in Sec. 3.4 because the solutions for $\bar{p}_e$ are input to the fluorescence model (Eq. 3.7) for fitting to local LIF spectra. In the previous sections, careful consideration was given towards the influence of coherent effects, optical pumping, velocity-changing collisions, and spatial averaging of the LIF-laser along the camera line of sight, with the purpose of finding the lowest level of sophistication required to accurately model LIF of a magnetized UCNP. The REs are required in order to account for optical pumping during LIF and provide a relatively efficient means for extracting macroscopic plasma characteristics. However, they are not quite efficient enough to provide real-time analysis during the data taking process.

It is desirable to have a model for LIF that can be used on-the-fly to quickly assess LIF data during the data taking process. The largest computational expense associated with the RE model is solving the REs, so a steady-state model for $p_e(v_x, \tau)$ would be considerably more efficient. In this section, a steady-state model is introduced to describe LIF in the regime of validity of Fermi's golden rule, where the ion state populations have reached equilibrium ($t \gg \gamma^{-1}$) and less than one photon is scattered per particle. This FGR model inherently does not account for optical pumping, so it should be used with caution when the latter condition is not satisfied. However, in the absence of magnetic fields, optical pumping only occurs through a slow leak to the ${}^2D_{3/2}$ state, so as we will show shortly, the FGR model is accurate for LIF of an unmagnetized UCNP with linearly polarized light after grafting on decay to the dark state.

The FGR model for LIF of Sr^+ makes the simplifying assumption that the saturation of state populations due to laser coupling of one state to more than one other state are treated independently of one another (i.e., in the two-level picture). In this case, the fraction of ions transferred from ground state $|g\rangle$ to excited state $|e\rangle$ is given by Eq. 3.37 for the two-level ion and the total population in state $|e\rangle$ is

$$p_e = \sum_g \frac{R_{eg} p_g(\tau = 0)}{\gamma + \gamma_D + 2R_{eg}}, \tag{3.47}$$

where the sum is over ground states $|g\rangle = |1\rangle, |2\rangle$ (Fig. 3.1b), R_{eg} is the scattering rate given by Eq. 3.39, and $p_k(v_x, \tau = 0) = \bar{p}_k G(v_x)$ is the population of each ground state prior to excitation for spin polarization $P = \bar{p}_2 - \bar{p}_1$.

For LIF of a magnetized UCNP, optical pumping between LIF ground states typically needs to be accounted for, so Eq. 3.47 is only valid for short excitation periods ($\tau_E \lesssim 200\,\mathrm{ns}$). However, for imaging with linear LIF-laser polarization, errors introduced due the neglect of optical pumping primarily occur in measurements of n due to the loss of resonant signal, but not in $v_{x,hyd}$ or P because the σ transitions are driven equally and the symmetry of the measured spectrum remains unchanged even when optical pumping occurs. In the absence of magnetic fields, where the degenerate π transitions are driven equally with linear polarization, Eq. 3.47 is accurate for longer excitation periods where decay into the ${}^2D_{3/2}$ state becomes significant.

The decay into the dark state can be grafted onto the FGR model with a simple rate equation approach:

$$\begin{aligned} p_e(\tau) &= (1 - p_D(\tau)) \sum_g \frac{R_{eg} p_g(0)}{\gamma + \gamma_D + 2R_{eg}} \\ \dot{p}_D(\tau) &= -\gamma_D \sum_e p_e(\tau) \end{aligned} \tag{3.48}$$

where $p_D(\tau) = 0$ is the population of the dark state prior to excitation. These equations are solved iteratively with a timestep of $2\gamma^2/\gamma_D \approx 26\gamma$. Here, it is not strictly necessary to track $p_g(\tau)$ because the existence of $p_g(0)$ in Eq. 3.48 is to account for the spin polarization; the number of ions transferred from one state to another depends on the fraction that occupied that state to begin with and the loss of ions from the cycling transitions is handled by the factor of $1 - p_D(\tau)$.

Figure 3.18(a) compares the FGR model given by Eqs. 3.48 in the absence of external magnetic fields for linear LIF-laser polarization through comparison with the REs given by Eqs. 3.40 for resonant excitation with $\Omega_{31} = \Omega_{42} = 0.22\gamma$ and $P = 0$. The excited state populations for each treatment disagree at early times during the initial rise in population for the REs, but converge after the rate equations reach equilibrium ($\tau \gtrsim 4$). The agreement indicates that the FGR model adequately captures the slow loss of population to the ${}^2D_{3/2}$ state. This was demonstrated experimentally by imaging a UCNP with $T_e(0) = 40\,\mathrm{K}$ after $t = 75\,\mu\mathrm{s}$ of plasma expansion in the absence of external magnetic fields using peak LIF-laser intensity $I_0 = 225\,\mathrm{W/m^2}$ (Fig. 3.19).

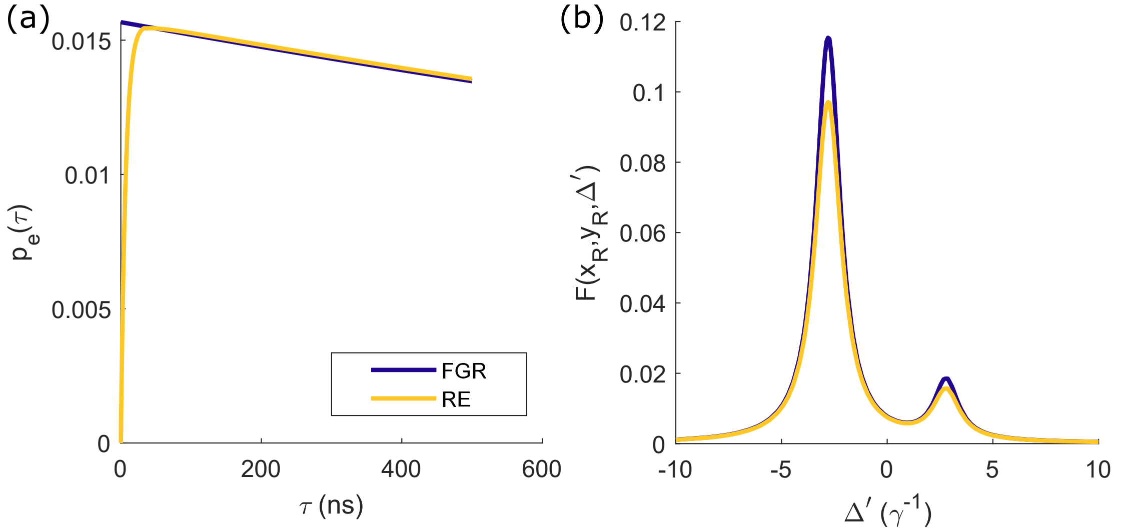

Figure 3.18 : Comparing the FGR and RE models for imaging $\bar{I} = 100\,\mathrm{W/m^2}$ with linear LIF-laser polarization (a) in the absence of magnetic fields and (b) with magnetic fields in a region R defined by $x = 2\,\mathrm{mm}$ and $y = 0$. The two models agree will with one another without fields for $\tau > 50\,\mathrm{ns}$, validating the ability of Eqs. 3.48 to account for loss of ions to the ${}^2D_{3/2}$ state. With magnetic fields, the resonant signal is 17% lower for the REs, but this loss should not influence measurements of $v_{x,hyd}$ or P because the symmetry of the spectrum is preserved.

The FGR model is also reasonably accurate for LIF in the presence of magnetic fields for short excitation periods ($\tau = 50 - 250\,\mathrm{ns}$). Figure 3.18(b) compares the FGR and RE models in a magnetic field of 30 G for $\Omega_{32} = \Omega_{41} = 0.22\gamma$ and an excitation duration $\tau_E = 250\,\mathrm{ns}$. The discrepancy between the FGR and RE models increases with the excitation duration because the FGR model does not account for optical pumping between the LIF ground states, which occurs primarily on resonance. However, despite the optical pumping, the symmetry in the spectrum is preserved for linear LIF-laser polarization because the coupling to the σ transitions is equal ($\Omega_{41} = \Omega_{32}$). The FGR model can thus be used to extract accurate measurements for $v_{x,hyd}$ and P. For the short excitation periods shown here, the density should be within $\approx 20\%$ of the real value.

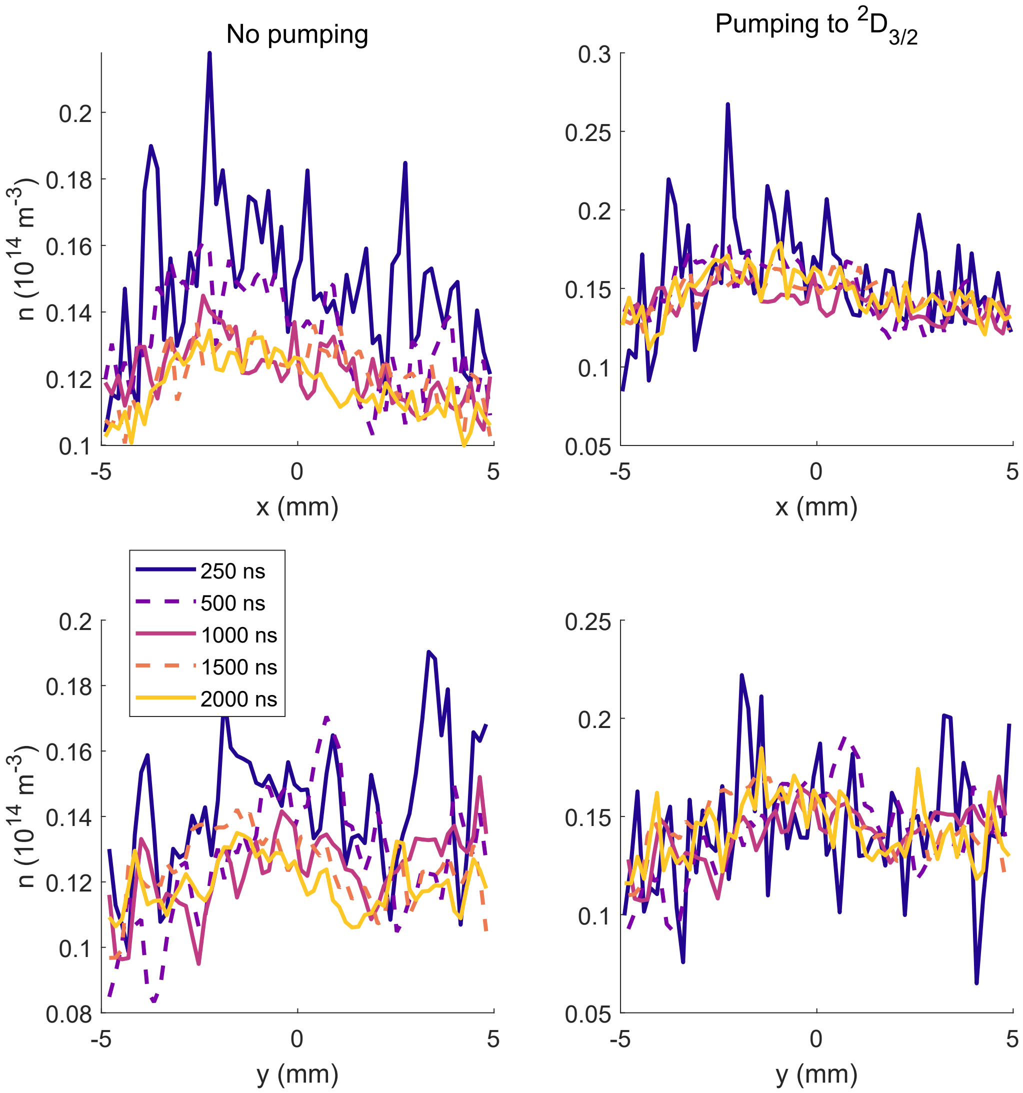

Figure 3.19 : Extraction of plasma density (n) along the x (top) and y (bottom) axes for a UCNP without magnetic fields using fits to the fluorescence model given by Eq. 3.7 with a steady-state model of ion state populations given by Eqs. 3.47 (left) and the rate equation model given by Eqs. 3.38−3.40 (right). The legend indicates the excitation duration.

3.11 Conclusions

In this chapter, we described LIF of magnetized UCNPs and a model based on rate equations that describe the transfer of ions between states involved in LIF due to laser coupling and spontaneous emission. This model can be fit to LIF spectra to extract local measurements of ion density, fluid velocity, temperature, and electron-spin polarization. The code for the spectrum fit model (Eqs. 3.7 and 3.38−3.40) and the MDQT simulations used to quantify the influence of collisions on LIF is publicly available [96]. These observations demonstrate that the ions in a UCNP created by photoionization of magnetically trapped Sr atoms are electron-spin polarized.

This probe was used in the recent experimental demonstration of magnetic confinement of a UCNP created at the null of a biconic cusp field [50], as described in Chap. 4, and will aid further study of the dynamics of magnetized and strongly coupled UCNPs. In Chap. 5, the time evolution of the ion spin polarization for a magnetically trapped UCNP is discussed. The ability to characterize the interrelated dynamics of the ion density and spin polarization should aid in the development of a magnetohydrodynamic model of magnetized UCNP dynamics.

Chapter 4

Magnetic Confinement of an Ultracold Neutral Plasma

The biconic cusp, or quadrupole magnetic field configuration, formed by anti-Helmholtz current coils [97, 98], can confine neutral plasmas near the central null-field region due to the magnetic-mirror effect [99]. This confinement scheme has been of long-standing interest, initially for magnetic-confinement fusion [97, 98, 100, 101, 102], and more recently for ion sources for applications such as material processing and ion thrusters [103, 104, 105]. Neutral plasma expanding across biconic cusp field lines experiences changing length scales and dominant physical processes, and the complex geometry has similarity to the solar wind interacting with the Earth's magnetosphere [98, 106]. In this chapter, we demonstrate the magnetic confinement of an ultracold neutral plasma (UCNP) [1, 3, 35] created at the null point of a biconic cusp field.

UCNPs, created here by photoionizing laser-cooled Sr atoms near the ionization threshold, have ion temperatures $T_i \sim 1\,\mathrm{K}$ and tunable electron temperatures of $T_e = 1-1000\,\mathrm{K}$, which offers a novel regime for study of magnetized and magnetically confined neutral plasmas. UCNPs also provide the opportunity to study the combined effects of magnetization and strong coupling on collisional and transport phenomena because ions are strongly coupled in UCNPs, with the ratio of Coulomb energy to kinetic energy, known as the Coulomb coupling parameter [107], as high as $\Gamma_i = 11$ [27, 52, 32]. Electrons can also approach the strongly coupled regime, with $\Gamma_e \lesssim 0.4$ [108, 109, 110, 111, 112]. There is emerging focus on magnetized and strongly coupled plasmas in general [4, 5] and in the ultracold regime [5, 7, 8], driven in large part by new experimental capabilities in dusty [9, 10, 11] and laser-produced high-energy-density plasmas [12, 13].

4.1 Principles for Plasma Confinement in a Magnetic Field

The dynamics of a neutral plasma in a non-uniform magnetic field are complex, but the potential for confinement within a purely magnetic trap is undergirded by two basic principles. The first principle is the reduction of plasma transport across a magnetic field, which can become prominent for particles that are magnetized (i.e., $\delta = \rho/L < 1$, where $\rho = \sqrt{mk_BT}/eB$ is the thermal gyroradius and $L = n/\nabla n$ is the length scale for density variation). For neutral plasmas that consist of electrons and relatively heavy ions ($m_i \gg m_e$, as is the case here), the electron gyroradius is typically much smaller than that of the ions unless there is a significant temperature difference between the species. Figure 4.1 plots the gyroradii for the (a) electrons and (b) ions as a function of typical magnetic field strengths and temperatures encountered in the experiment. The electrons are magnetized with $\delta < 1$ everywhere except for within a small vicinity of the field null and are strongly magnetized with $\delta \ll 1$ for $B \gtrsim 20\,G$. On the other hand, the ions are typically unmagnetized and only become weakly magnetized with $\delta \approx 1$ for $B \gtrsim 50\,\mathrm{G}$.

A pioneering experiment with magnetized UCNPs studied the expansion of the plasma in a uniform magnetic field for conditions similar to those in Fig. 4.1, where the fields are strong enough to magnetize the electrons but not the ions [68]. This study found that the UCNP expansion dynamics were consistent with an anisotropic ambipolar diffusion model, where the cross-field transport was significantly reduced and the expansion along the field was unaffected. Assuming classical diffusion [68],

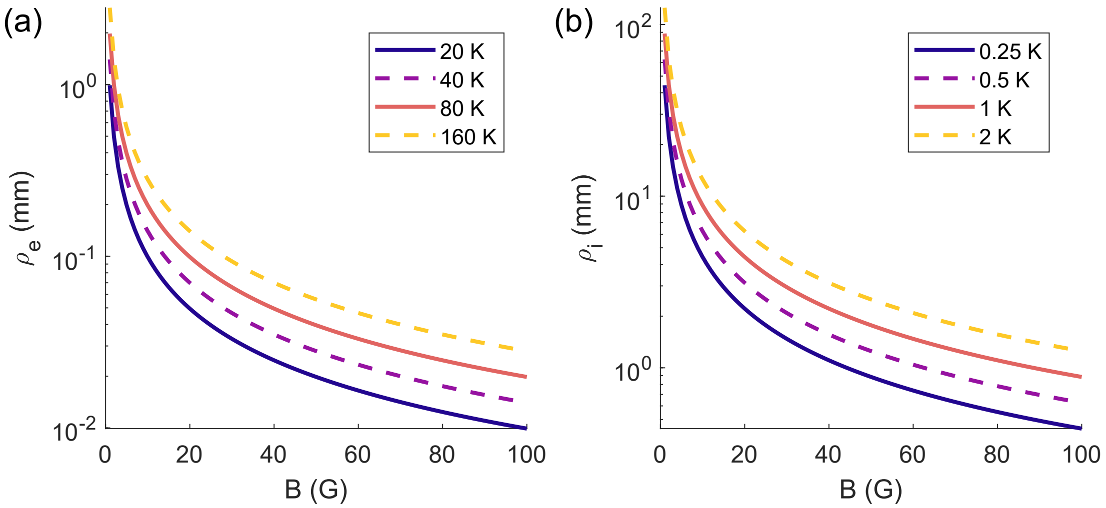

Figure 4.1 : Thermal gyroradius (ρ) for (a) electrons and (b) ions as a function of typical magnetic field strengths used in the experiment. The legend indicates the temperature of each species. The UCNPs described here begin with an initial plasma size of $\sigma(0) = 1\,\mathrm{mm}$. The electrons are strongly magnetized with $\delta \ll 1$ for $B \gtrsim 20\,\mathrm{G}$, while the ions are only weakly magnetized with $\delta \approx 1$ for $B \approx 60\,\mathrm{G}$.

where transport across the field is mediated by collisions that shift the guiding center for electron gyromotion, the transverse diffusion rate is $D_\perp = \rho_e^2 \nu_{ei}$, where $\nu_{ei} \propto n/T_e^{3/2}$ is the electron-ion collision rate [113].

The second principle for confinement relies on the magnetic mirror force, which arises for particle motion along a magnetic field of increasing strength due to the conservation of the particle's magnetic moment $\mu = mv_\perp^2/eB$, where $v_\perp$ is the particle's velocity transverse to the local field. The magnetic moment is an adiabatic invariant so long as the magnetic field changes slowly on length and time scales relevant for gyromotion (ρ and ω_c^{-1}, respectively, where $\omega_c = eB/m$ is the gyrofrequency). In this case, the force per particle is $\vec{F_\parallel} = -\hat{l}\mu\partial B/\partial l$ pointing in the direction of decreasing field strength, where l is the distance along the field line.

The magnetic mirroring of particles is conventionally discussed in the single-particle picture, where particles with large enough μ and small enough translational kinetic energy $\mathcal{E}$, described as having a large pitch angle, are trapped between bounce points. For the plasmas considered here, the electrons would be efficiently trapped in the magnetic mirror on their own. However, the mirroring of neutral plasmas is more complicated because the mirror force must also slow the motion of the ions, which carry the bulk of the inertia. Furthermore, collisions limit the efficacy of magnetic mirror trapping because they tend to scatter particle velocities into orientations that lower the magnetic moment and cause particles to diffuse away from the field center.

For the experiments described here, the external magnetic field is stationary in time and the pressure of the plasma ($P = nk_BT$) is significantly smaller than the pressure of the quadrupole field ($P_B = B^2/2\mu_0$), characterized by a beta parameter of $\beta = P/P_B \ll 1$. Thus, the plasma experiences changes in the external field primarily through bulk motion in spatially varying fields. The terminal hydrodynamic flow velocity of a UCNP in the absence of magnetic fields is $v_{x,hyd} \approx \sqrt{k_BT_e/m_i}$, so the condition for adiabatic invariance is

$$\frac{1}{B}\frac{\partial B}{\partial t} = \frac{v_{x,hyd}}{B}\frac{\partial B}{\partial x} < \omega_c. \tag{4.1}$$

For the largest electron temperature ($T_e = 160\,\mathrm{K}$) and field gradient along the symmetry axis ($\partial B/\partial x = 150\,\mathrm{G/cm}$) considered here, the condition for adiabatic invariance is well satisfied for the electrons.

The quadrupole magnetic field configuration provides both conditions required for confinement of a neutral plasma. Figure 4.2 qualitatively illustrates the expansion dynamics for a plasma localized at the trap center. Due to the reduction of cross-field transport, the plasma more freely expands into the line cusp along the symmetry axis (x) of the anti-Helmholtz coils and the ring cusp along the y-z plane. Long term confinement occurs through the magnetic mirror force because the field gradient increases with distance from the plasma center.

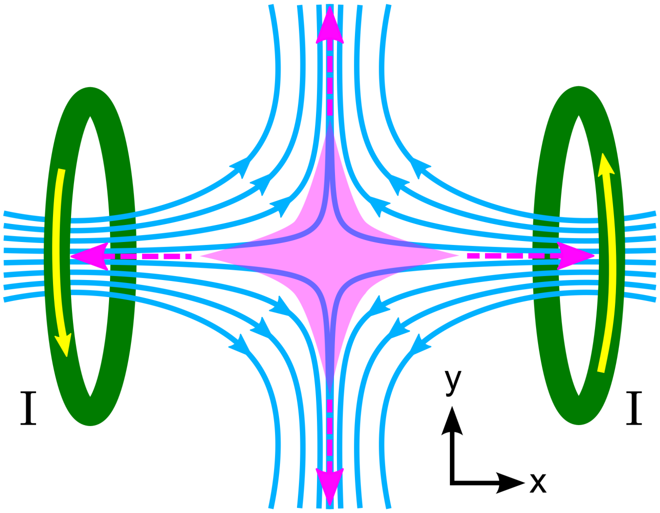

Figure 4.2 : Schematic for plasma expansion in a biconic cusp field. Plasma transport across magnetic field lines is reduced and plasma flow primarily occurs through the loss gaps along the symmetry axis (x) and the y-z plane. Long time confinement is achieved through the magnetic mirror effect due to the increasing magnetic field strength in the loss gaps.

4.2 Expansion of an Exponential Plasma

The creation of a UCNP by photoionization of magnetically trapped atoms in a quadrupole magnetic field results in an exponentially decaying density distribution of the form

$$n = n_0 \exp\left(-\frac{\sqrt{x^2 + (y^2 + z^2)/\eta^2}}{\alpha}\right), \tag{4.2}$$

where α characterizes the plasma size along the x axis and $\eta\alpha$ characterizes the plasma size along the y and z axes (see Sec. 2.2). Here, cylindrical symmetry has been assumed. Nominally, $\eta = 2$ because the magnetic field gradient is twice as large along the symmetry (x) axis, however, η can vary because the spatial distribution of the ionizing radiation can influence the distribution that the ions inherit from the precursor atoms. Prior to discussing the influence of the magnetic fields on the plasma expansion, it is first instructive to consider the plasma dynamics in the absence of magnetic fields, which are studied by extinguishing the field over a 280 μs period prior to photoionization.

The expansion of an exponentially decaying plasma, which from now on will be referred to as an exponential plasma, was studied in detail in [40] and the following discussion is based on results from this article. The conditions for the expansion of an exponential plasma were found to be largely hydrodynamic for lower T_e and higher n. For hydrodynamic conditions, the expansion of an exponential plasma can be parameterized by similar length ($\sigma_m(0)$) and time (τ_{exp}) scales as their Gaussian counterparts because in each case the expansion is driven by gradients in the electron thermal pressure. Here, $\sigma_m = (\sigma_x \sigma_y \sigma_z)^{1/3}$ is the geometric mean of the rms plasma size, as characterized by a Gaussian density distribution of the form

$$n = n_0 \exp\left(-\frac{x^2}{2\sigma_x^2} - \frac{y^2}{2\sigma_y^2} - \frac{z^2}{2\sigma_z^2}\right). \tag{4.3}$$

Figure 4.3 compares the density (n, top) and velocity ($v_{x,hyd}$, bottom) transects along the x axis for a plasma with an initially Gaussian and exponential distribution as a function of time after photoionization [40]. The velocity distribution of the Gaussian plasma is linear with space ($v_{x,hyd} = \gamma(t)r$, where $\gamma(t) = t/[\tau_{exp}^2(1 + t^2/\tau_{exp}^2)]$) throughout its evolution, resulting in a self-similar expansion of the density distribution. The density distribution is well characterized by fits to Eq. 4.3 and the time evolution of the plasma size was found to be well characterized by

$$\sigma_m(t)^2 = \sigma_m(0)^2(1 + t^2/\tau_{exp}^2). \tag{4.4}$$

For the exponential plasma, the velocity profile deviates dramatically from the

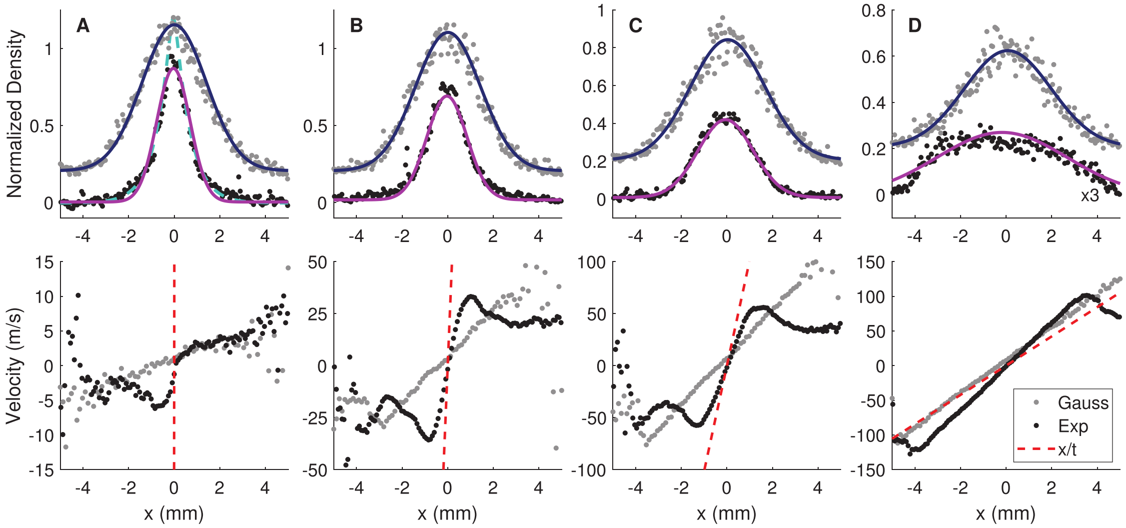

Figure 4.3 : Transects along the x axis of the plasma density (top) and velocity (bottom) distributions, for Gaussian and exponential plasmas with initial peak densities of $1.0 \times 10^9\,\mathrm{cm}^{-3}$ and $3.5 \times 10^9\,\mathrm{cm}^{-3}$, respectively, and electron temperature $T_e = 40\,\mathrm{K}$. Density transects for the Gaussian plasmas are offset for clarity. The time after photoionization is (a) $0.34 \pm 0.01\,\mu\mathrm{s}$, (b) $5.7 \pm 0.1\,\mu\mathrm{s}$, (c) $14 \pm 4\,\mu\mathrm{s}$, (d) $27 \pm 3\,\mu\mathrm{s}$. All density transects are fit to integrals over the LIF-laser-sheet thickness of a Gaussian density distribution (solid lines). The first time point (a) for the exponential plasma is also fit to the integral over the LIF-laser-sheet thickness of Eq. 4.2. Reused with permission from [40]. Copyright 2021 by the American Institute for Physics.

self-similar solutions for the Gaussian plasma due to a steep velocity gradient that develops near the cusp ($|x| \lesssim \alpha$). Due to the lack of self-similarity, the density distribution is poorly characterized by Eq. 4.2 throughout plasma expansion, so the time evolution of the plasma size is characterized by fits to Eq. 4.3. The exponential density distribution immediately after photoionization (Fig. 4.3a) was fit with Eqs. 4.2 and 4.3. The peak density extracted from fits to each model will differ significantly, but do yield similar values for the initial plasma size (i.e., $\alpha \approx \sigma_x$). Despite the lack of self-similarity, the plasma size was found to be well described by Eq. 4.4 with a modified effective expansion time scale $\tau_{exp} \to \beta\tau_{exp}$, where $\beta = 0.63$. For $t \gg \beta\tau_{exp}$, the velocity profile approaches $v_{x,hyd} = x/t$.

4.3 Results

In this section, we introduce measurements of the plasma density (n) and hydrodynamic flow velocity along the LIF-laser propagation direction ($v_{x,hyd}$) from [50] that demonstrate the magnetic confinement of a UCNP created at the null of a quadrupole magnetic field. The plasma was probed at an adjustable time after photoionization using LIF on the $5s\,^2S_{1/2} - 5p\,^2P_{1/2}$ transition of Sr^+ at 422 nm [33], as described in Chap. 3. For the data shown here, the LIF laser is linearly polarized along the y axis and the peak LIF-laser intensity is $I_0 \approx 150\,\mathrm{W/m}^2$. The intensity distribution of the LIF laser is similar to the characterization given in Sec. 3.1.1, except that the $1/e^2$ radius of beam along the y axis is $\approx 10\,\mathrm{mm}$. Plasma images were collected over an excitation period of duration $\tau_E = 0.5 - 2\,\mu\mathrm{s}$ and image times indicated in all figures refer to the midway point of the imaging window.

The results in [50] predate the development of the rate equation model described in Sec. 3.4, so measurements of n and $v_{x,hyd}$ were extracted through fits of local LIF spectra to the FGR spectrum model given by Eqs. 3.7 and 3.47. The FGR model does not account for the optical pumping of ions into states not driven by the LIF laser and therefore systematically underestimates the plasma density. For the excitation conditions used here, the errors are relatively small and the use of the FGR model provides a rather faithful representation of the relative density distribution. No error is expected for measurements of $v_{x,hyd}$ because optical pumping does not influence the symmetry of the recorded spectrum when imaging with linearly polarized light.

Fig. 4.4 shows the evolution of n and $v_{x,hyd}$ without and with magnetic fields for a UCNP with $T_e(0) = 20$ K and $\sigma(0) = 1.3$ mm ($\tau_{exp} = 30\,\mu\mathrm{s}$). The data in Fig. 4.4 is obtained by fitting the FGR model to local spectra that were averaged over 20-60 realizations of the plasma (more images were used for longer expansion times). A

2D Gaussian smoothing filter with RMS width 0.2 mm was used to filter out high-frequency noise components. Initially ($t = 1.5\,\mu$s), the plasma density and velocity distributions without (Fig. 4.4(a) and (c)) and with (Fig. 4.4(b) and (d)) the fields are nearly identical and the plasma has not yet developed significant expansion velocity.

At early times ($t < \tau_{exp}$), outward hydrodynamic pressure dominates and the expansion is relatively unaffected by the magnetic fields. This is reflected by the nearly identical density distributions at $t = 29\,\mu$s. However, while constant $v_{x,hyd}$ along lines of constant x is observed without fields as expected for $\vec{v}_{hyd} \propto \vec{r}$, velocity retardation is evident for ions traversing field lines in regions far from plasma center where the fields are large. For example, along the $y = 2x$ and $y = -4.8$ mm lines (indicated in Fig. 4.4(c) and (d), $t = 1.5\,\mu$s), magnetic forces have clearly impeded the expansion by $t = 29\,\mu$s. This is highlighted in the velocity transects shown in Fig. 4.5. Along the x-axis, where plasma expansion velocity is parallel to the field lines, $v_{x,hyd}$ is still unaffected by fields.

By $t = 85\,\mu$s the no-fields plasma appears uniform because the plasma size exceeds the imaged region. Gradients in plasma density that produce outward electron thermal pressure have diminished, leading to a ballistic plasma expansion for no fields that persists throughout the rest of the expansion (green line in Fig. 4.5 representing $v_{x,hyd} = x/t$).

The with-fields plasma shows considerable effects of the magnetic fields during this intermediate time. The plasma begins to develop a boundary that follows a field line (Fig. 4.4(b)). Expansion near the plasma center is relatively unaffected because of the weak fields, leading to a central plasma depletion and a build up of plasma density at the boundary. The effects on the plasma velocity, evident at earlier times, become stronger. Most striking is a reversal of $v_{x,hyd}$ in regions of strong field where

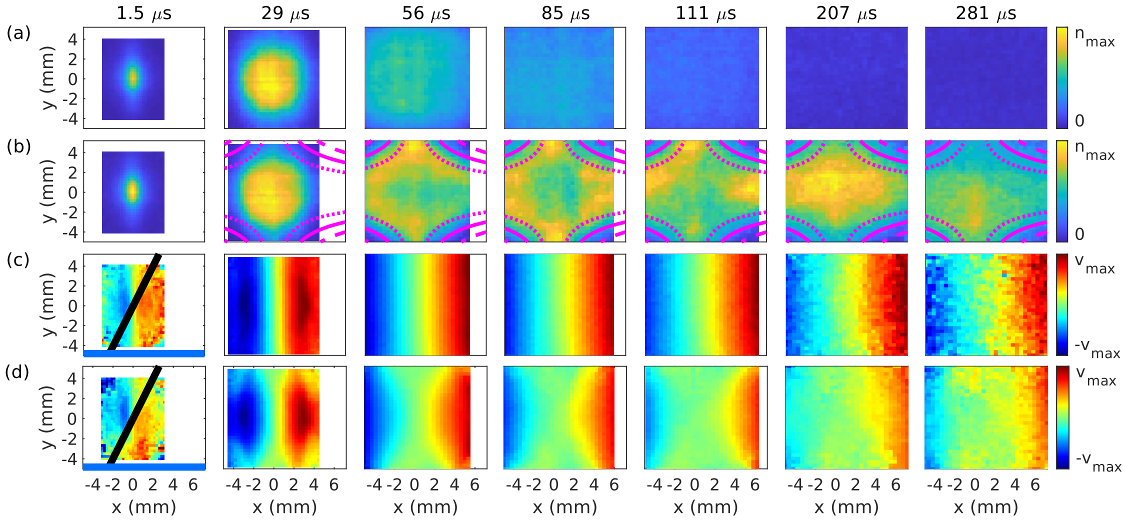

Figure 4.4 : Plasma expansion without and with magnetic field ($B' = 150$ G/cm) for $T_e(0) = 20$ K. Rows (a) and (b) show density distributions without and with field, respectively. The lines in row B (dotted, solid, dashed), correspond to sample field lines. Time after plasma creation is indicated above each column. The scale for the density color bar for each time point is $n_{max} = [13.8, 1.7, 0.59, 0.36, 0.25, 0.18, 0.18] \times 10^8$ cm^{-3}, in order of increasing time. Rows (c) and (d) show the x-component of the hydrodynamic velocity, $v_{x,hyd}$, without and with magnetic fields, respectively. The scale for the velocity color bar for each time point is $v_{max} = [10, 70, 100, 75, 62, 35, 25]$ m/s. The black and blue lines in the first time point of rows c and d correspond to $y = 2x$ and $y = -4.8$ mm, respectively. Fig. 3 plots $v_{x,hyd}$ along each of these lines. Reused with permission from [50]. Copyright 2021 by the American Physical Society.

the expansion velocity is close to perpendicular to field lines, such as near $x \pm 2\,\text{mm}$ for $y = -4.8\,\text{mm}$. The velocity reversal is subtle in Fig. 4.4(d), but is easier to discern in Fig. 4.5(bottom). The combined density and velocity information indicates that plasma flow across field lines in these regions has halted, and is now redirected along field lines back towards $x = 0$ and increasing $|y|$ for $|x| \lesssim 2\,\text{mm}$.

The initial expansion of the UCNP is driven by gradients in the hydrodynamic electron thermal pressure [3], which creates a force per ion of

$$\vec{F}_{exp}(\vec{r}, t) = -\frac{\nabla n(\vec{r})}{n(\vec{r})} k_B T_e(t), \tag{4.5}$$

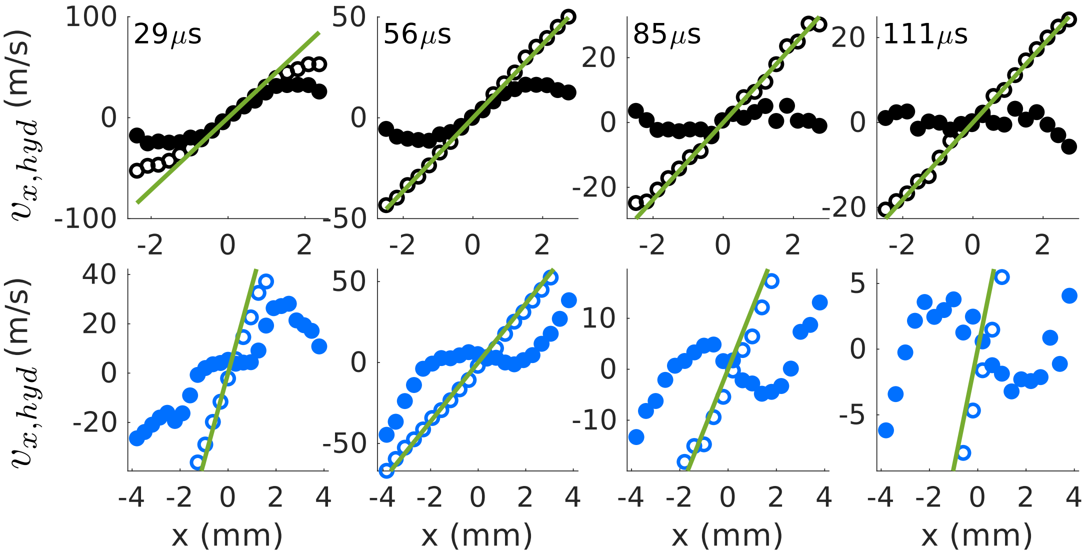

Figure 4.5 : Evolution of the x-component of hydrodynamic velocity for plasma along the lines $y = 2x$ (top) and $y = -4.8$ mm (bottom) for data shown in Fig. 4.4 for plasmas evolving without (open symbols) and with (closed symbols) magnetic fields. The solid green line represents $v_{x,hyd} = x/t$, the ion velocity expected for $\vec{v}_{hyd} = \gamma(t)\vec{r}$ or ballistic expansion at late times ($t \gg \tau_{exp}$). Time since plasma creation is indicated above each column. Reused with permission from [50]. Copyright 2021 by the American Physical Society.

where $T_e(t)$ is the electron temperature, which decreases during expansion due to adiabatic cooling. The UCNP expansion may equivalently be described as ambipolar diffusion, where the electrons and ions diffuse together at the ion acoustic velocity. Deviations between no-fields and with-fields plasma velocity for ions crossing field lines are observed as early as $t = 29\,\mu$s (for example, along the velocity transects in Fig. 4.5). The Lorentz force that the fields exert on charged particles of species s due to the expansion velocity, $\vec{F}_L(\vec{r}, t) = q_s\,\vec{v}_{x,hyd}(\vec{r}, t) \times \vec{B}(\vec{r})$ is negligible compared to $\vec{F}_{exp}$ at this time, and is not responsible for the velocity reduction.

However, at the boundary of the with-fields plasma, where the effects of the magnetic field on the expansion first appear, the magnetization of the plasma is significant, as characterized by the magnetization parameter $\delta = \rho/L$, the ratio of thermal gyroradius $\rho = \sqrt{k_B T_s m_s}/eB$ to the characteristic lengthscale of the plasma $n(\vec{r})/\nabla n(\vec{r}) \equiv L \sim 1\,\mathrm{mm}$. For $B \approx 50\,\mathrm{G}$ and $T_e = 10\,\mathrm{K}$, $\rho_e = 10\,\mu\mathrm{m}$, indicating the electrons are strongly magnetized. For ions with $T_i = 0.25\,\mathrm{K}$, the magnetization is modest, with $\rho_i \approx L$. This suggests that the reduction of cross-field expansion results from pinning of the strongly magnetized electrons to field lines, as discussed in Sec. 4.1. The transverse diffusion constant is $D_\perp = \rho_e^2 \nu_{ei} \approx 1\,\mathrm{mm}^2/\mathrm{ms}$ for ion density $n_i = 2 \times 10^7\,\mathrm{cm}^{-3}$. Cross-field diffusion several mm from the field null should thus be slow on the timescale of these experiments, as observed.

At late times (Fig. 4.4, $t > 150\,\mu\mathrm{s} \sim 5\tau_{exp}$), the expansion for the magnetized plasma has essentially halted and the plasma has become magnetically trapped, with a density maximum in the plasma center. Magnetic confinement arises from the magnetic mirror effect, which results from conservation of the adiabatic invariant $\mu \equiv m_s v_\perp^2/2B$ for a charged particle moving along a guiding field line, where $v_\perp$ is the particle's velocity transverse to the local field. Ion motion for plasma regions imaged in Fig. 4.4 is not adiabatic because the ion cyclotron period is longer than the lifetime of the ions in the magnetic trap, but electron motion is adiabatic everywhere except close to the field null due to their extremely small mass (see Sec. 4.1). Thus, as expected for biconic cusp fields [97, 98, 102, 114], the likely description of UCNP trapping is that electrons move along field lines, confined between bounce points, and ambipolar electric fields transverse to magnetic field lines constrain ion cross-field transport and provide long-term confinement for the ions.

Plasma with large enough bulk flow momentum can escape through loss gaps around the field maxima along field lines in the y-z plane and along the x symmetry axis (Fig. 4.2(a)). This loss is fed by non-adiabatic mixing of electron trajectories

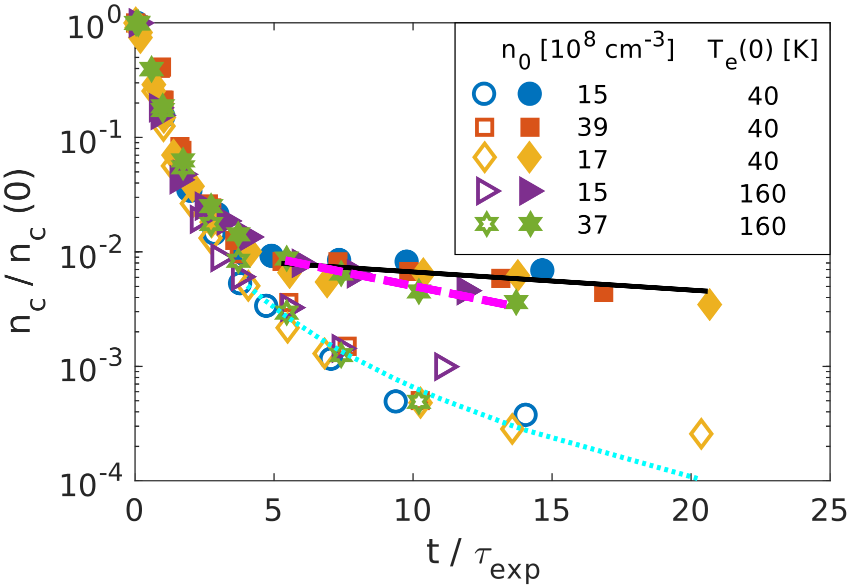

Figure 4.6 : Relative plasma density in the plasma center versus time scaled by the hydrodynamic expansion timescale (τ_{exp}) without (open symbols) and with (closed symbols) magnetic field. Solid and dashed lines are exponential fits to $T_e(0) = 40$ K and $T_e(0) = 160$ K with-fields data, respectively, for $t > 5\tau_{exp}$. The dotted line is a $1/t^3$ fit to all no-fields data with $t > 4\tau_{exp}$. Initial peak density and electron temperature are indicated in the legend. Reused with permission from [50]. Copyright 2021 by the American Physical Society.

near the field null and by collisions. In the loss gaps, ambipolar fields slow electrons, leading to plasma loss at ion acoustic velocities $\propto \sqrt{T_e/m_i}$ [114]. To characterize the onset of confinement and rate of plasma loss, Fig. 4.6 shows the time evolution of the central normalized plasma density $n_c(t)$ relative to its initial value. Time is scaled by the characteristic hydrodynamic timescale. A $1/t^3$ fit to data with $t > 4\tau_{exp}$ demonstrates the ballistic nature of plasma expansion without fields at late times.

In contrast, the with-fields (closed symbol) central density stabilizes at $n_c(t)/n_c(0) = 10^{-2}$ at $t = 5\tau_{exp}$. Developing a quantitative explanation for this universal behavior will the subject of future study, but it is generally consistent with the onset of trapping occurring when the average hydrodynamic expansion force (Eq. 4.5), which decreases rapidly with time, matches the typical magnetic mirror force. While the onset time and level of trapping in scaled units shows no discernible dependence on density, the trap lifetime decreases for higher $T_e(0)$, which is consistent with plasma loss through loss gaps at the ion acoustic speed. The solid and dashed lines in Fig. 4.6 are exponential fits to $T_e = 40\,\mathrm{K}$ and $T_e = 160\,\mathrm{K}$ data, respectively, which reveal magnetic confinement timescales of $500\,\mu\mathrm{s}$ (40 K) and $100\,\mu\mathrm{s}$ (160 K).

4.4 Scaling of Trapping Dynamics with T_e

In Fig. 4.6, it was shown that the trap lifetime decreases with the initial electron temperature. In this section, we take a closer look at how the magnetized plasma dynamics scale with $T_e(0)$ for a UCNP under predominantly hydrodynamic conditions. For a meaningful comparison of how the dynamics scale with the initial electron temperature, it is important that the initial plasma density distribution does not vary significantly for each case. Although the initial plasma density was not found to play a significant role in the evolution of the central plasma density, it can in principle influence the evolution because $D_\perp \propto n$. Furthermore, the expansion of the plasma at early times ($t \lesssim \tau_{exp}$) is dominated by gradients in the electron thermal pressure and the plasma size expands according to Eq. 4.4, so it is also important that the initial plasma sizes are the same.

Fig. 4.7 compares the evolution of plasma density for UCNPs with $T_e(0) = 40\,\mathrm{K}$ (Fig. 4.7a,c) and $T_e(0) = 160\,\mathrm{K}$ (Fig. 4.7b,d). The initial density distribution for each case is characterized by fits to Eq. 4.2, which yield peak density $n_0 = 4.88 \pm .02 \times 10^9\,\mathrm{cm}^{-3}$, plasma size $\alpha = 0.68 \pm .01\,\mathrm{mm}$, and $\eta = 1.65 \pm .01$. Time after photoionization is indicated above rows (a) and (c) in units of τ_{exp}. The LIF data shown in Fig. 4.7 was recorded with linear LIF-laser polarization using $I_0 = 70\,\mathrm{W/m}^2$

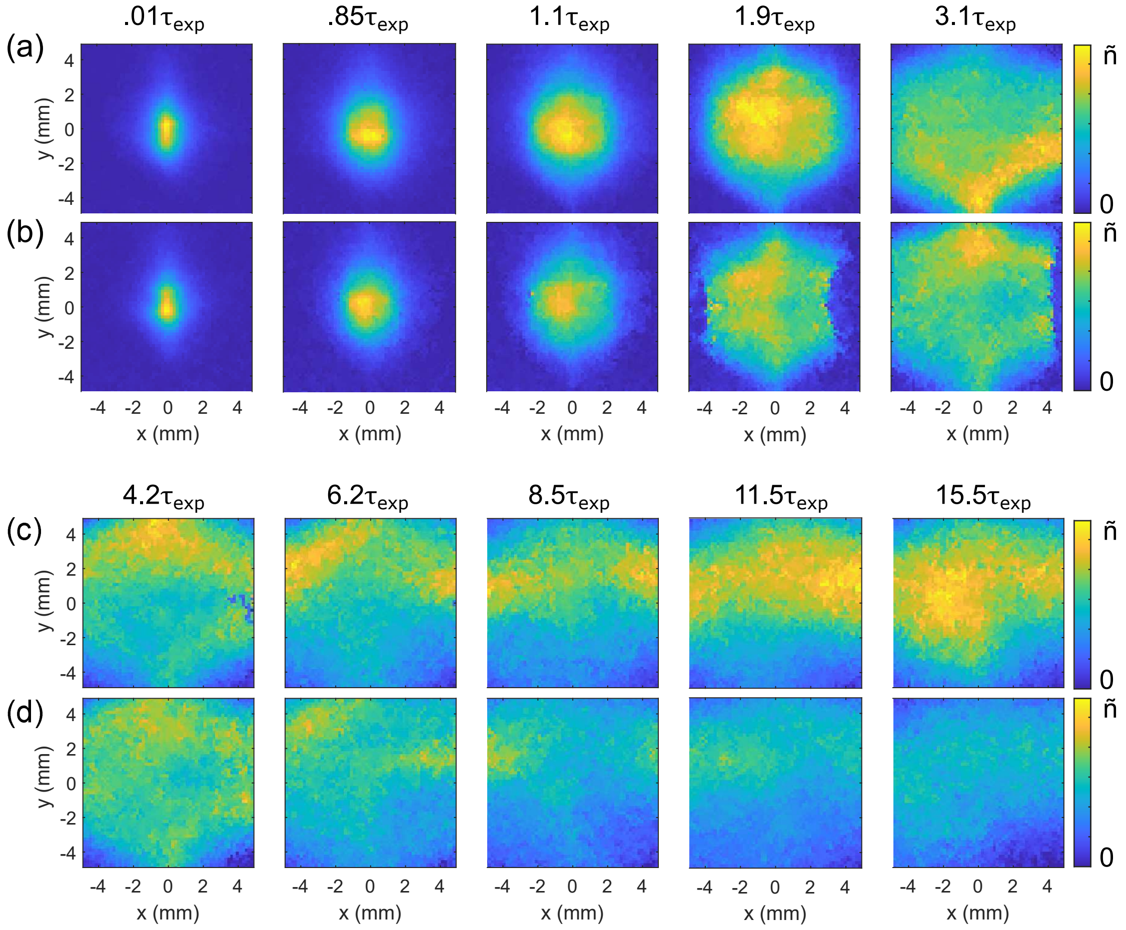

Figure 4.7 : Time evolution of normalized plasma density ($\tilde{n} = n/n_0$) in quadrupole magnetic fields for a UCNP with (a)/(c) $T_e(0) = 40\,\mathrm{K}$ and (b)/(d) $T_e(0) = 160\,\mathrm{K}$. For each T_e, the initial peak plasma density and geometric mean of the plasma size are $n_0 = 4.9 \times 10^9\,\mathrm{cm}^{-3}$ and $\sigma_m(0) = 0.96\,\mathrm{mm}$, respectively. The color bar maximum in order of increasing time after photoionization is $\tilde{n} = [1, .41, .22, .09, .04, .024, .015, .012, .009, .007]$. For the images corresponding to row (b) and $t = 1.9 - 3.1\tau_{exp}$, the hard cutoff of plasma density in peripheral regions of the plasma is an artifact of the analysis because the spectra in those regions were Doppler- and Zeeman-shifted out of the LIF-laser detuning range used to record the spectra.

and $\tau_E = 0.5 - 2\,\mu\mathrm{s}$, with larger exposure period being used for later expansion time. Local measurements of n were obtained by fitting spectra to Eqs. 3.7 and 3.38–3.40.

The plasma dynamics are nearly identical for each electron temperature before the onset of magnetic trapping when time is scaled in terms of τ_{exp} ($t \lesssim 4\tau_{exp}$, rows (a) and (b)). At early times ($t \lesssim 1.5\tau_{exp}$), the expansion is dominated by the electron thermal pressure as expected, and shortly afterward the plasma molds to the field lines. Note that for $t = 1.9 - 3.1\tau_{exp}$ in row (b), the hard cutoff of the plasma density distribution near $|x| \approx 4\,\mathrm{mm}$ is an artifact of the data taking process. In these regions, the spectra were Doppler- and Zeeman-shifted out of the range of detunings used to record the LIF data. This issue is not present for any other images shown.

The similarity between the spatial distributions at these times provides further evidence that the expansion dynamics are driven by ambipolar diffusion, as discussed in Sec. 4.1. The cross-field diffusion rate scales with the electron temperature as $D_\perp \propto 1/\sqrt{T_e}$. For time in units of $\tau_{exp} \propto 1/\sqrt{T_e}$, the ambipolar diffusion rate $\tilde{D}_\perp = D_\perp \tau_{exp}^{-1}$ has no dependence on T_e. After the onset of magnetic trapping ($t \gtrsim 4\tau_{exp}$), the spatial distributions of n are still very similar, but the density decreases more rapidly for larger electron temperature. At $t = 15.5\tau_{exp}$, the density for $T_e(0) = 160\,\mathrm{K}$ is approximately half that for $T_e(0) = 40\,\mathrm{K}$.

4.5 Conclusions

In this chapter, we demonstrated the magnetic confinement of a UCNP in a biconic cusp magnetic field. The plasma density and velocity-field profiles and estimates of relevant forces imply that the plasma confinement results from strongly magnetized electrons following guiding field lines and ions constrained by ambipolar fields. Observed trap lifetimes decrease with increasing electron temperature, which is consistent with a dominant loss mechanism of flux through the loss gaps.

The magnetic confinement of UCNPs opens many new research directions. UCNPs have long been used for experimental studies of the effects of strong coupling on collisional transport processes [6], and these new capabilities may enable exploration of overlapping regimes of strong coupling and magnetization [4, 5]. With experimental improvements such as increased magnetic field gradient and field of view for LIF imaging, it should be possible to characterize scaling of trapping behavior with magnetic field and study plasma flow in loss gaps, which will support development of a quantitative model of plasma dynamics. The combination of magnetic trapping with recently demonstrated techniques of laser cooling of UCNP ions [32] appears promising for improving laser cooling efficacy. Because the loss processes for the biconic cusp trap are localized along loss gaps, laser-induced forces should be particularly effective for plugging the loss in this geometry, perhaps leading to significantly enhanced trap lifetimes.

Chapter 5

Evolution of the Electron-Spin Polarization in a Magnetized UCNP

In Chapter 4, we discussed the magnetic confinement of a UCNP created at the null of a biconic cusp field. That discussion focused on the interrelated spatial and temporal dynamics of the plasma density (n) and the hydrodynamic flow velocity along the LIF-laser propagation direction ($v_{x,hyd}$). In this chapter, we extend that discussion to the electron-spin polarization of the ions ($P = \bar{p}_2 - \bar{p}_1$), which characterizes the difference in the ensemble-averaged fraction of ions that occupy the two magnetic sublevels of the $^2S_{1/2}$ electronic ground state of Sr^+.

The spin polarization of the ions is derived from the atomic gas from which the plasma is formed. Following photoionization, the liberated electron carries away the angular momentum of the ionizing photon and the remaining valence electron is unperturbed, such that the ions inherit the spin polarization from the precursor magnetically trapped atoms. The $^3P_2$ atoms in the magnetic trap predominantly occupy the $m_j = +2$ magnetic sublevel because this sublevel is the most efficiently trapped (see Sec. 2.2). The valence electrons in this state are both field aligned, so the resulting ions are highly spin polarized in the field-aligned $m_j = +1/2$ sublevel of the $^2S_{1/2}$ ground state.

The ability to measure P is an interesting byproduct of the model introduced in Chapter 3 to describe LIF of Sr^+ ions in the presence of external magnetic fields. In Section 3.5.2, a constrained fit routine to LIF data recorded separately with LC, linear, and RC LIF-laser polarization was introduced to extract measurements of n, $v_{x,hyd}$, T_i, and P. The data recorded with LC and RC polarization provides valuable information for measurements of P where the spectral Zeeman components are unresolved because the coupling to each ground sublevel is unequal everywhere except for along the y axis; imaging light with RC polarization will have a stronger σ^- drive for $x > 0$ and a stronger σ^+ drive for $x < 0$ (and vice versa for LC polarization). Measurements of n, $v_{x,hyd}$, and P shown in this chapter were obtained using constrained fits of Eqs. 3.7 and 3.38−3.40 to local spectra recorded with LC, linear, and RC polarization using peak laser intensity $I_0 \approx 150\,\mathrm{W/m^2}$ and an exposure period of duration $\tau_E = 500\,\mathrm{ns}$. Fit results for P will not be shown for regions adjacent to the y axis for $|y| < 3\,\mathrm{mm}$ because the spectra are not sensitive to P in these regions.

In the next section, we will discuss the spatial and temporal evolution of P and how these measurements suggest that the spin-flip rate in the plasma is low. This behavior is expected because the collision energies and densities are low enough that state-changing collisions are negligible. Under these conditions, the electron-spin polarization should be useful for studying plasma flow and diffusion. In Sec. 5.2, we will discuss how optical pump-probe techniques can be used in magnetized UCNPs to spin-tag and monitor the evolution of local groups of ions. In Sec. 5.3, we will show how the time evolution of P is described by a continuity relation when spin-flips can be neglected.

5.1 Preliminary Measurements

Figure 5.1 shows the evolution of n and P for a UCNP with $T_e(0) = 20\,\mathrm{K}$ and $\sigma_m(0) \approx 1\,\mathrm{mm}$ ($\tau_{exp} \approx 23\,\mu\mathrm{s}$). Figures 5.2 and 5.3 show transects of n, P, and $v_{x,hyd}$ along $y = 0$ and $x = y$ for the same data as in Fig. 5.1. Immediately after photoionization

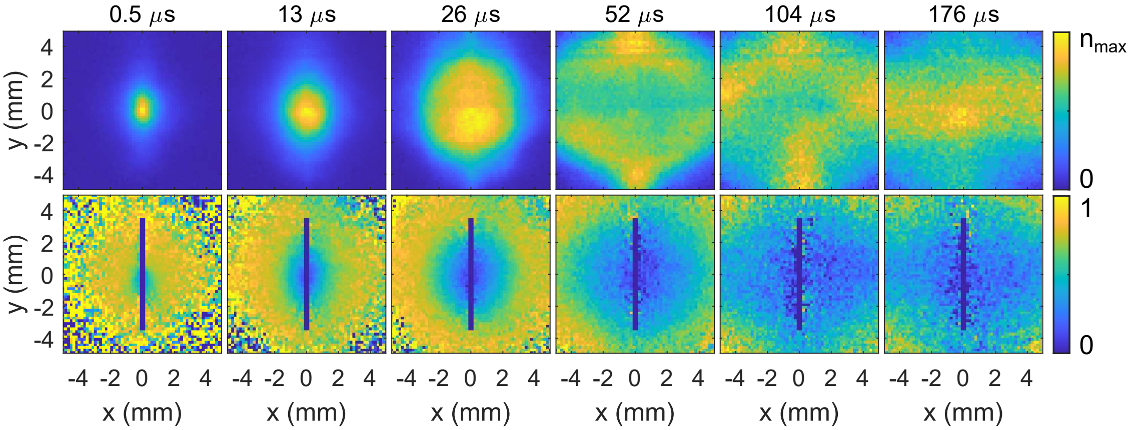

Figure 5.1 : Time evolution of (top) density and (bottom) electron-spin polarization of the ions during expansion for a UCNP with $T_e(0) = 20\,\mathrm{K}$ and $\sigma_m(0) \approx 1\,\mathrm{mm}$. Time after plasma creation is indicated above each column. The scale for the density color bar for each time point is $n_{max} = [52,\ 19,\ 5.8,\ 2.4,\ 0.8,\ 0.48] \times 10^8\,\mathrm{cm}^{-3}$.

($t = 0.5\,\mu$s), the plasma is highly spin polarized with $P \gtrsim 0.75$ for $r > \sigma_m(0)$. The spin polarization decreases towards the plasma center for $r \lesssim \sigma_m(0)$, but cannot be resolved at the field null. The regions closest to the field null where P can be resolved ($|x| = 0.25\,\mathrm{mm}$, $y = 0$) indicate $P \approx 0.45$ immediately after photoionization. We get a better idea of the initial spin polarization at the field null after a short period of expansion because central ions have expanded into regions where P can be resolved. By $t = 26\,\mu$s, the spin polarization has reached $P \approx 0.15$ near the field null and remains at this value throughout the duration of plasma expansion.

An imperfect polarization is not surprising because atoms in the $m_j = +1$ sublevel of the $^3P_2$ state are also magnetically trappable, albeit less efficiently than ions in the $m_j = +2$ sublevel, and the spin alignment of the electron left behind is not uniquely determined. Furthermore, non-adiabatic motion of atoms through the field null throughout the trapping of precursor atoms will lead to a constant transfer of the efficiently trapped $m_j = +2$ atoms to other sublevels. Atoms that flip to states

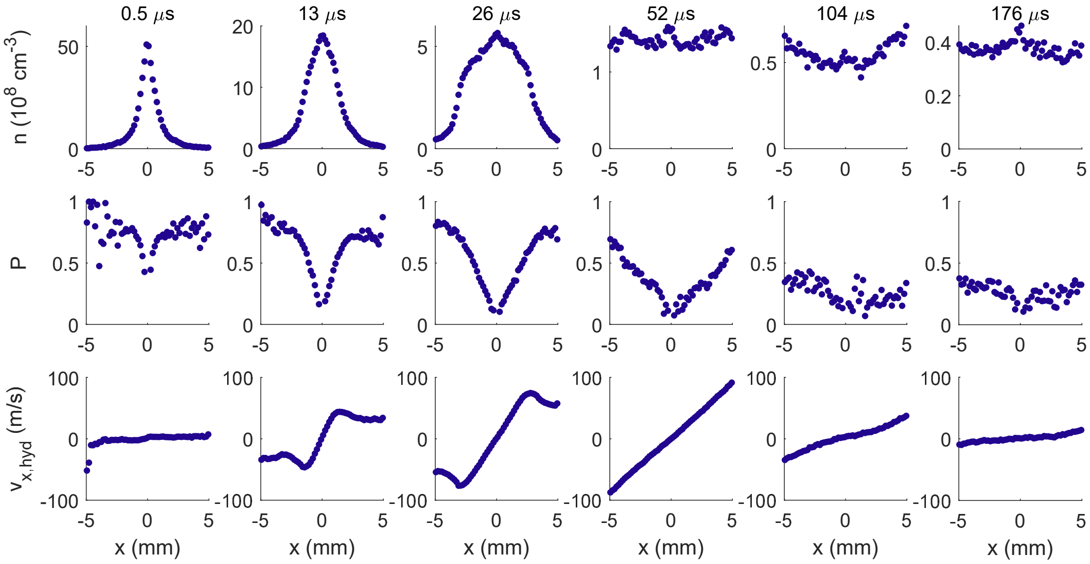

Figure 5.2 : Evolution of n, $v_{x,hyd}$, and P along the symmetry (x) axis for the same data set shown in Fig. 5.1.

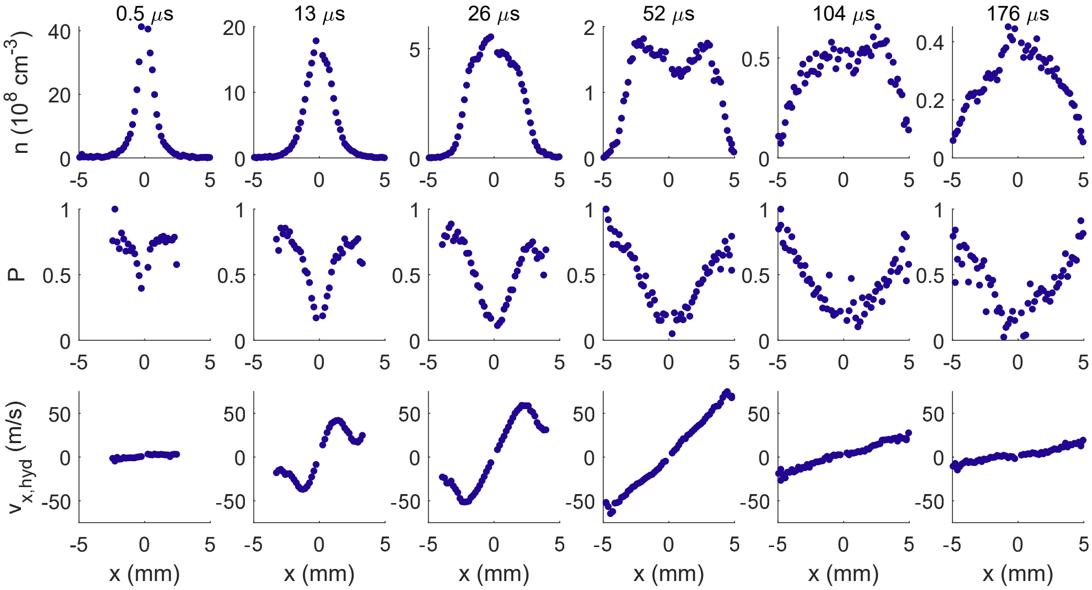

Figure 5.3 : Evolution of n, $v_{x,hyd}$, and P along $x = y$ for the same data set shown in Fig. 5.1.

with $m_j < 0$ are anti-trapped and will be quickly expelled from the trap, but a significant portion of atoms can accumulate in the $m_j = 0$ state because this state does not interact with the fields. The ionization of these atoms will on average result in $P = 0$.

At early times during plasma expansion when the influence of the magnetic fields is small ($t \lesssim 26\,\mu$s), the hydrodynamic flow velocity generally increases with distance from plasma center and the length scale for change in n and P evolve at similar rates. At later times when the magnetic fields have slowed the expansion across field lines ($t \gtrsim 52\,\mu$s), the evolution of n and P in the loss gaps (i.e., the x axis and the y-z plane) differ significantly from the cross-field regions (i.e., $|x| \approx |y|$). Along the x axis (Fig. 5.2), the weakly polarized ions that originate from near the field null flow relatively freely and the spin polarization decreases until the plasma is magnetically trapped at $t = 104\,\mu$s. In contrast, cross-field diffusion is significantly reduced along $x = y$ (Fig. 5.3) and the distribution for n and P do not change significantly after $t = 52\,\mu$s.

The stabilization of P for $t \geq 104\,\mu$s suggests that the internal states of individual ions are conserved throughout the plasma evolution and the polarization within a local volume element only changes due to the flow of particles into and out of the element. Because P cannot be measured at the field null, we cannot definitively determine whether the polarization changes due to non-adiabatic motion through the field null. However, the data in Figs. 5.1−5.3 suggest that this rate is low because the polarization in the regions adjacent to the field null ($|x| \approx 0.25\,$mm) do not change significantly for $t \geq 26\,\mu$s.

Similar observations were made for the evolution of a UCNP with $T_e(0) = 40\,$K. Figures 5.4 and 5.5 compare the evolution of 2D distributions and 1D transects along

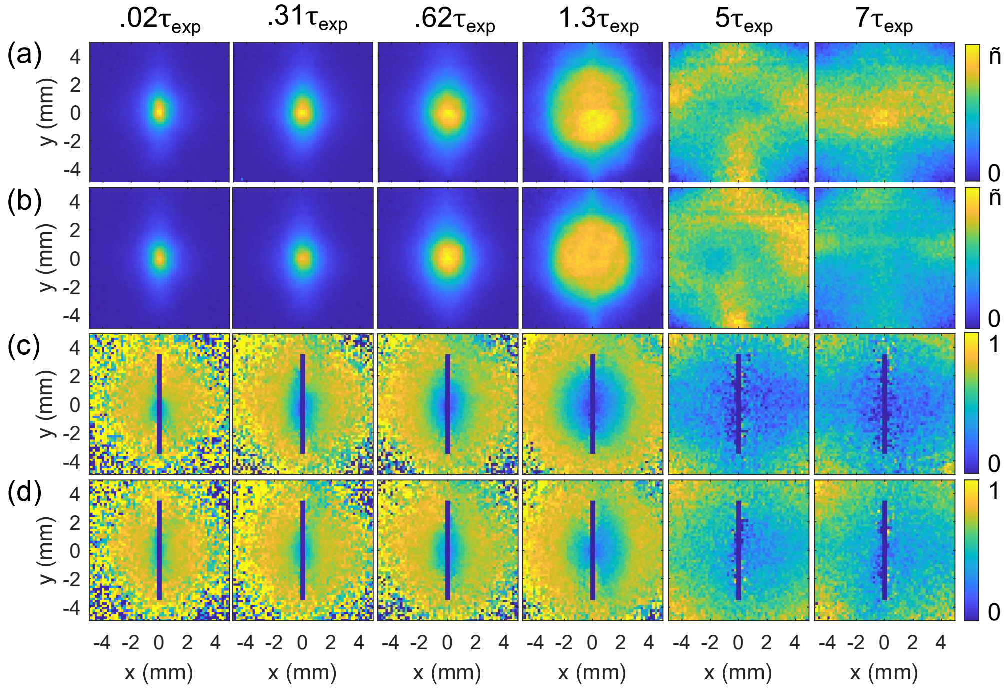

Figure 5.4 : Comparing the evolution of (a)-(b) $\tilde{n} = n/n_0$ and (c)-(d) P for a UCNP with $T_e(0) = 20\,\mathrm{K}$ [(a),(c)] and $T_e(0) = 40\,\mathrm{K}$ [(b),(d)]. The initial peak density is $5.2 \times 10^9\,\mathrm{cm}^{-3}$ (20 K) and $4.7 \times 10^9\,\mathrm{cm}^{-3}$ (40 K). Time after photoionization is indicated above each column in units of τ_{exp}. The maximum of the density color bar in order of increasing time after photoionization is $\tilde{n} = [1, 0.92, 0.43, 0.13, 0.02, 0.015]$.

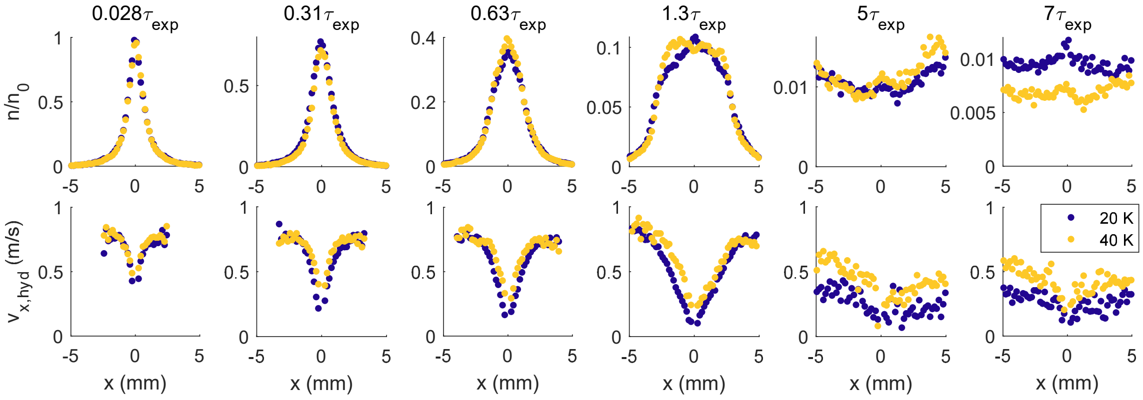

Figure 5.5 : Comparing the evolution of n and P for a UCNP with $T_e(0) = 20\,\mathrm{K}$ and $T_e(0) = 40\,\mathrm{K}$ along the x symmetry axis for the same data in Fig. 5.4.

the x axis, respectively, for n/n_0 and P for the 40 K plasma with the 20 K plasma shown in Figs. 5.1−5.3. The evolution of the normalized density and spin polarization profiles are very similar throughout the duration of plasma expansion and confinement. After the onset of magnetic trapping ($t \approx 5\tau_{exp}$), the density for the 40 K plasma decays more quickly than the 20 K plasma, which is consistent with decreasing trap lifetime for increasing T_e observed in Sec. 4.3. The spin polarization for the 40 K plasma is higher than the 20 K plasma initially, likely due to differences in the spin polarization of the precursor atoms, and throughout the duration of plasma expansion. For each data set, the spin polarization in the regions adjacent to the field null decrease until they stabilize to $P \approx 0.15$ (20 K) and $P \approx 0.25$ (40 K) at $t \approx 1.3\tau_{exp}$. The stabilization of the distributions for P provides further evidence that changes to individual ion spin states are negligible on these timescales.

5.2 Spin-Tagging Ions in a Magnetized UCNP

The time evolution of P tells us a great deal about plasma flow because UCNPs created at the null of a biconic cusp field are initialized with decreasing spin polarization towards the plasma center, where the density is highest, and the polarization will decrease anywhere the dense central ions flow to. For example, the spin polarization in cross-field regions remains high throughout plasma expansion, which indicates that ions near the field null do not penetrate far into these regions. Thus, the spin polarization essentially allows us to monitor which ions go where when there is a gradient in P.

In this section, we consider how the distribution of P can be sculpted through spatially dependent optical pumping in a way that facilitates the monitoring of the evolution of a small population of spin-tagged ions. The concept of spin-tagging (i.e., using laser light to manipulate the internal states of the ions) is not new in the field of UCNPs. For example, optical pump-probe techniques have been used previously to measure Coulomb collision rates [34] and self-diffusion [62] in strongly coupled UCNPs. In these experiments, counter-propagating cross-polarized lasers are used to establish non-equilibrium velocity distributions for ions in the ${}^2S_{1/2}$ electronic ground state of Sr^+ and spin-selective LIF measurements allow for the monitoring of these distributions as they relax towards equilibrium (Fig. 1.5).

Cross-polarized lasers were required in previous experiments to establish a local velocity dependence to optical pumping, so as to skew local velocity distributions for each magnetic sublevel of the ground state. For the spin-tagging techniques proposed here, one laser is sufficient for establishing a gradient in the ensemble-averaged internal states because the velocity dependence is integrated out. We have already seen in Sec. 3.5.3 that optical pumping occurs to states dark to the driving laser while illuminating ions in a magnetic field with a fixed laser detuning. Optical pumping is most effective when the laser coupling to each ground state differs, which can occur any time the transitions are resolved or when the coupling to the σ transitions is unequal. These conditions are most broadly satisfied by circularly polarized radiation because the couplings to the σ transitions differ everywhere except for along the y axis and the σ transitions are easier to resolve than the π transitions due to their larger Zeeman splitting.

A collimated, circularly polarized laser that propagates along the x axis can be used to optically pump millimeter-sized holes into the spatial distribution of P for a UCNP in a quadrupole magnetic field. The collisional rate equation (REK) model for ion population transfer (Eqs. 3.38−3.41) can simulate the time evolution of P for a magnetized UCNP under the influence of a driving laser. Figures 5.6 and 5.7

demonstrate spin-tagging of a UCNP with $T_e(0) = 20\,\mathrm{K}$ after $t = 26\,\mu\mathrm{s}$ and $t = 104\,\mu\mathrm{s}$, respectively, following an excitation of duration $\tau_E = 1\,\mu\mathrm{s}$ with a RC-polarized laser. Measurements of n, $v_{x,hyd}$, and P prior to spin-tagging are shown in panels (a)-(c) and panel (d) shows the REK simulations of the spin polarization following spin-tagging, $P(\tau_E)$. In each grid cell, measurements of n, $v_{x,hyd}$, T_i, and P are input to the REK model to simulate spin-tagging of the measured plasma conditions in each region for a driving laser that propagates along the x axis and is centered at $y = 1.5\,\mathrm{mm}$ with a peak effective laser intensity $\bar{I} = 250\,\mathrm{W/m^2}$ and $1/e^2$ radius of $0.75\,\mathrm{mm}$ along the y axis. The laser polarization and propagation direction were chosen to ensure a stronger σ^- drive for $x > 0$, such that the ions, which are initially polarized in the $m_j = +1/2$ ground state, are optically pumped into the $m_j = -1/2$ ground state. Similar results can also be achieved with LC-polarized light propagating along the $-x$ direction.

The location and dimensions of the optically pumped region can be controlled with the properties of the driving laser. The hole location along the y axis is controlled through laser alignment while the location along the x axis is dependent on the laser detuning because of the Doppler shift along the laser propagation axis. For the simulations in Figs. 5.6 and 5.7, the detuning has been chosen such that the ions were optically pumped in approximately the same spatial region ($x \approx 1.5\,\mathrm{mm}$). The size of the region along the y axis is primarily shaped by the $1/e^2$ radius of the driving laser, which can easily be controlled with optical lenses or through truncation of the laser by a slit, as is done to control the thickness of the LIF imaging sheet. The size along the x axis is determined from the combined Zeeman and Doppler shifts of the driving laser. The $150\,\mathrm{G/cm}$ field gradient along the x axis results in $\approx 28\,\mathrm{MHz/mm}$ Zeeman shifts of the σ transitions, which should lead to spatial selectivity on the order of a

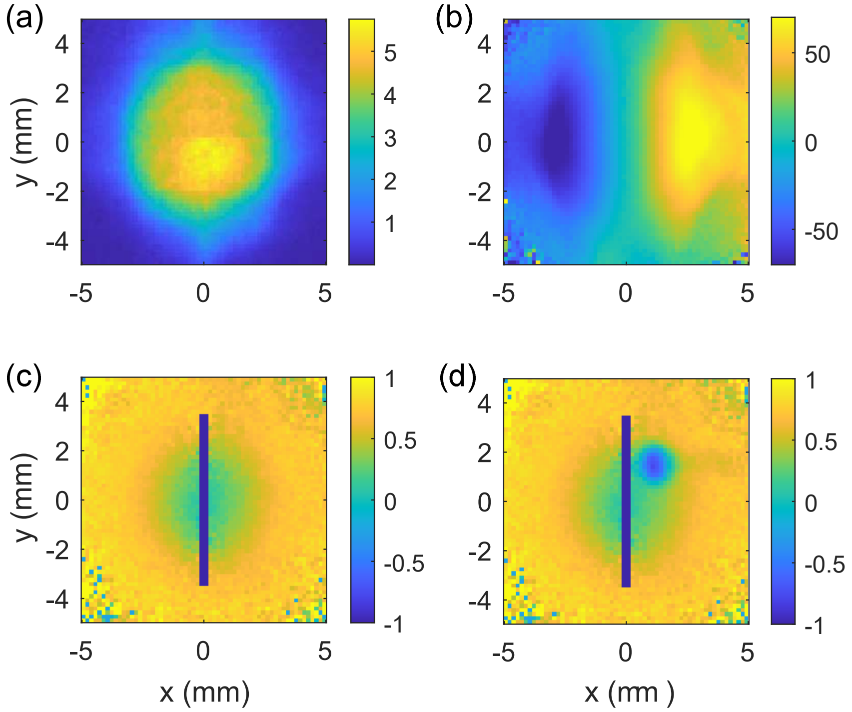

Figure 5.6 : Spin-tagging a UCNP with $T_e(0) = 20\,\mathrm{K}$ after $26\,\mu$s of evolution in a biconic cusp field. Panels (a)-(c) show measurements of n, $v_{x,hyd}$, and P prior to spin-tagging ($\tau = 0$). Panel (d) shows $P(\tau_E)$, the spin polarization after an excitation of duration $\tau_E = 1\,\mu$s with a RC-polarized laser that propagates along the x axis. The peak laser intensity $I_0 = 250\,\mathrm{W/m^2}$ is centered at $y = 1.5\,\mathrm{mm}$ and the beam has a $1/e^2$ radius of $0.75\,\mathrm{mm}$ along the y axis. Density and velocity are expressed in units of $10^8\,\mathrm{cm^{-3}}$ and m/s, respectively.

few millimeters, depending on the Doppler width of the velocity distribution.

Gradients in the hydrodynamic flow velocity along the laser propagation (x) axis will lead to increased spatial resolution for the pumped region. Prior to the onset of magnetic trapping ($t = 26\,\mu$s; Fig. 5.6), the velocity gradient along the x axis is the largest and the pumped region is approximately circular with a $1/e^2$ radius of $0.75\,\mathrm{mm}$. At later times when the velocity gradient is reduced ($t = 104\,\mu$s; Fig. 5.7), the size of the pumped region along the x axis has approximately doubled and remains the same along the y axis.

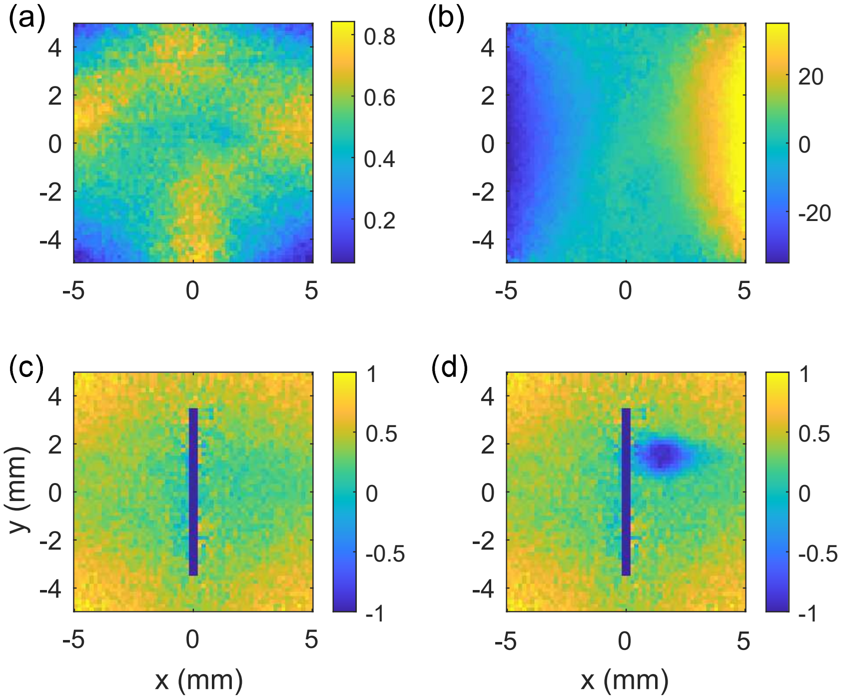

Figure 5.7 : Spin-tagging a UCNP with $T_e(0) = 20\,\mathrm{K}$ after $104\,\mu\mathrm{s}$ of evolution in a biconic cusp field. Panels (a)-(c) show measurements of n, $v_{x,hyd}$, and P prior to spin-tagging ($\tau = 0$). Panel (d) shows $P(\tau_E)$, the spin polarization after an excitation of duration $\tau_E = 1\,\mu\mathrm{s}$ with a RC-polarized laser that propagates along the x axis. The peak laser intensity $I_0 = 250\,\mathrm{W/m^2}$ is centered at $y = 1.5\,\mathrm{mm}$ and the beam has a $1/e^2$ radius of $0.75\,\mathrm{mm}$ along the y axis. Density and velocity are expressed in units of $10^8\,\mathrm{cm^{-3}}$ and m/s, respectively.

This technique should be useful for studies of plasma flow and diffusion because a small region of ions can be spin-tagged essentially anywhere in the plasma throughout its lifetime. It should be possible to reduce the size of the spin-tagged region along the y axis by decreasing the $1/e^2$ radius of the driving laser and along the x axis either by increasing the magnetic field gradient or by creating a plasma with higher T_e, which results in larger velocity gradients.

One potential limitation for this technique could be ion motion along the z axis, which could limit the time that spin-tagged ions will remain within the x-y imaging plane defined by the thickness of the LIF imaging sheet. In the absence of external magnetic fields, components of velocity along the z axis are negligible in the x-y plane. However, the trajectory of ions moving across magnetic field lines can be curved out of the plane either due to the influence of the Lorentz force on ion bulk-flow motion, thermal gyromotion, or drift velocities that arise due to gradients in the magnetic field. However, all of these effects are expected to be small on timescales of interest here because the ions are weakly magnetized.

The curvature of bulk-flow motion across magnetic field lines due to the Lorentz force occurs on times scales set by the inverse of the ion gyrofrequency ($\omega_{ci} = eB/m_i$). For the largest magnetic fields used here ($B \approx 75\,\mathrm{G}$), the period of ion gyromotion is $t_c = 2\pi/\omega_c \approx 750\,\mu\mathrm{s}$. However, the ions do not have significant velocity components across the magnetic field lines in regions of large magnetic field. For ions closer to the field null, which may have significant expansion velocity across the field, the time and length scale for bulk-flow gyromotion will be much longer due to the weaker fields and, thus, this should not be a concern. Likewise, similar arguments can be made for the neglect of thermal gyromotion.

Drift velocities can arise in magnetized plasmas in the presence of an external force ($\vec{F}$) that is perpendicular to the local magnetic field. The guiding center drift velocity is given generally by

$$v_{gc} = \frac{\vec{F} \times \vec{B}}{eB^2}. \tag{5.1}$$

In Sec. 4.1, we discussed how magnetic field gradients result in a force of the form $\vec{F} = -\mu\nabla\vec{B}$, where μ is the magnetic moment for thermal ion motion. Thus, when $\vec{B} \perp \nabla\vec{B}$ and the local field lies in the x-y plane, the drift velocity will have a component in the z direction. Due to the dependence on the ion's magnetic moment, it is difficult to provide an estimate of the ion drift velocity because ion motion is not adiabatic. By the same token, the adiabatic moment is expected to be small and, therefore, the drift velocity should also be small.

5.3 Modeling the Evolution of P

The LIF data presented in this chapter demonstrates that the electron-spin polarization of the ions is long-lived, which suggests that spin-flip mechanisms in the plasma, such as those induced by collisions or non-adiabatic motion through the field null, are slow compared to the $\sim 100\,\mu$s timescales for these experiments. The polarization should not influence the bulk flow motion of the ions in the magnetic field because spin-dependent interactions are negligible, so the evolution of P should be well described by a magnetohydrodynamic (MHD) treatment where the density of ions in state $|k\rangle$, $n_k = n\bar{p}_k$, evolves according to the following continuity relation

$$\frac{\partial n_k}{\partial t} + \nabla \cdot (n_k \vec{v}_k) = 0, \tag{5.2}$$

where v_k and $\bar{p}_k$ are the hydrodynamic flow velocity and ensemble-averaged fraction of ions in state $|k\rangle$, respectively (quantum state indices correspond to those in Fig. 3.1). In the absence of driving fields, the ions occupy one of the two magnetic sublevels in the ${}^2S_{1/2}$ electronic ground state, such that $\bar{p}_1 + \bar{p}_2 = 1$ and the total density is $n = n_1 + n_2$.

The time evolution of P is embedded within the continuity relation given by Eq. 5.2. The spin-independence of the evolution requires $\vec{v}_1 = \vec{v}_2 = \vec{v}$. As a result, the spin polarization density $\tilde{P} = nP$ can be shown to obey an analogous continuity relation by subtracting Eq. 5.2 evaluated with $k = 1$ from that evaluated with $k = 2$ to obtain

$$\frac{\partial \tilde{P}}{\partial t} + \nabla \cdot (\tilde{P}\vec{v}) = 0. \tag{5.3}$$

Eq. 5.3 is best suited for integration in numerical models because it is expressed in conservative form. However, the dependence on n, which is implicit within $\tilde{P}$, can be removed from Eq. 5.3 if desired by expanding the derivatives with the product rule and using the continuity relation for n to obtain

$$\frac{\partial P}{\partial t} + \nabla \cdot (P\vec{v}) = P(\nabla \cdot \vec{v}). \tag{5.4}$$

The term on the RHS of Eq. 5.4 describes how local gradients and time variation of n influence the evolution of P.

5.4 Conclusions

In this chapter, we presented preliminary measurements of the time evolution of the electron-spin polarization of ions in a UCNP that is created at the null of a biconic cusp field. These observations demonstrate that the spin polarization is long-lived because the spatial distribution for P stabilizes after the onset of plasma confinement, which suggests that collision-induced spin-flips are low. While these measurements also suggest that spin-flips due to non-adiabatic motion through the field are slow on the timescale of these experiments, the inability to measure the polarization within a small vicinity of the field null makes it difficult to conclusively rule them out.

Nevertheless, the length scale for gradients in n and P are sufficiently large at the onset of magnetic confinement that P is well determined for the vast majority of the ions in the plasma. Subsequent evolution of the plasma should not be significantly affected by the ions remaining in the regions where P cannot be measured because the hydrodynamic flow velocity generally scales with distance from plasma center and, therefore, the small number of ions at the center largely remain stationary.

In future work, we plan to develop a model for the dynamics of a UCNP within a biconic cusp field. In the previous section, we showed how the electron-spin polarization density of the ions follows a continuity relation. This should make it relatively straightforward to incorporate the dynamics of P into single- or two-fluid magnetohydrodynamic model of the plasma. The ability to spin-tag and monitor the flow of local groups of ions should prove useful in the development of such a model.

Chapter 6

Conclusions

In this thesis, we developed a model to describe LIF of UCNPs in an external magnetic field and used LIF imaging to demonstrated the magnetic confinement of a UCNP that is created at the null of a biconic cusp field. UCNPs offer a novel regime for the study of magnetized neutral plasmas due to their dilute densities and ultracold temperatures and are uniquely suited for the study of strongly coupled plasmas across the full regime of magnetization. The ability to resolve the density, velocity, and internal-state distributions of the ions in magnetic fields builds a foundation for future studies of the combined effects of magnetization and strong coupling on collisional and transport phenomena in magnetized and magnetically confined neutral plasmas.

Magnetic confinement within a biconic cusp field should compliment the recent application of laser cooling to the ions in UCNPs [32] and help extend the range of ion Coulomb coupling that can be realized in the laboratory. The ion coupling has traditionally been limited to $\Gamma_i = 2 - 5$, however, laser cooling/heating extended this range to $\Gamma_i = 0.1 - 11$ in the center of the plasma where ion velocities remain low. The primary limitation to the cooling efficacy in these experiments was the rapid plasma expansion, which limits the amount of time available for laser cooling and Doppler shifts ions in peripheral regions of the plasma out of resonance with the cooling lasers. The introduction of magnetic fields promises to alleviate both of these issues through magnetic confinement, which greatly enhances the plasma lifetime, and spatially varying Zeeman shifts, which should extend the effective region for cooling to a larger portion of the cloud. In kind, optical forces should also enhance magnetic confinement times by reducing the loss of ions through the field cusps.

The magnetic confinement times observed here could be improved in future work by trapping the precursor atoms in a weaker magnetic field than is used to trap the plasma. Currently, we do not possess the capability of ramping the magnetic fields on fast enough timescales that would allow the field strength to be changed appreciably during the $\sim 100\,\mu$s time period between atom trapping and photoionization. As a result, the initial plasma size is proportional to the field gradient used to trap both the atoms and the plasma. However, the ability to ramp the fields on and off quickly would both allow for atom trapping to occur at lower field strengths than used here while also allowing for higher field strengths to be used to confine the plasma. With these improvements and increased field of view for LIF imaging, it should be possible to characterize the scaling of trapping behavior with the initial plasma size, electron temperature, and magnetic field strength and study plasma flow in the loss gaps.

The dynamics of a UCNP in a biconic cusp field are complex and in future work we plan to develop a magnetohydrodynamic model that should elucidate the physical mechanisms that undergird the plasma behavior. Comparison with experimental data will be important for determining what level of sophistication will be required to accurately model the influence of the magnetic fields on plasma transport. The electrons in UCNPs are strongly magnetized in the sense that the time and length scales for gyromotion are smaller than the hydrodynamic expansion time scale and length scale for change in plasma density, respectively, while the ions are weakly magnetized. In this case, a two-fluid model may be required to describe how the magnetic fields influence the transport of ions indirectly through ambipolar fields that develop between the ions and strongly magnetized electrons.

Measurements of the electron-spin polarization should aid in the development of such a model because it allows for the tracking of which ions go where. For example, the polarization is lower near the field null for the UCNPs described here, so as the plasma expands we gain information about where the ions are flowing based on where the spin polarization decreases as the plasma expands. The spin-tagging techniques discussed in Sec. 5.2 should enhance our ability to monitor the flow of a small subset of ions in the plasma.

The initial distribution for the spin polarization can be influenced by the distribution of the precursor atoms or the photoionization process. In either case, the initial spin polarization is not as important as the conservation of it after plasma creation. The data presented here confirms that the collisional spin-flip rate is low by demonstrating that the polarization stabilizes in cross-field regions for long time periods. The data also suggests that spin flips due to non-adiabatic motion through the field null are low on the timescales of these experiments, however, this cannot be conclusively ruled out because the spin polarization cannot be measured at the field null. In future experiments, it could be useful to obtain measurements of P with similar initial density distributions as described here and with higher $T_e(0)$. The faster expansion timescale will lead to less time for ions to occupy the field null and could help determine the rate that spin flips occur due to non-adiabatic motion through the field null.

Bibliography

[1] T. C. Killian, S. Kulin, S. D. Bergeson, L. A. Orozco, C. Orzel, and S. L. Rolston, "Creation of an Ultracold Neutral Plasma," *Physical Review Letters*, vol. 83, pp. 4776–4779, Dec. 1999.

[2] B. T. Draine and L. Hao, "Gamma-Ray Burst in a Molecular Cloud: Destruction of Dust and H2and the Emergent Spectrum," *The Astrophysical Journal*, vol. 569, pp. 780–791, Apr. 2002. Publisher: American Astronomical Society.

[3] T. C. Killian, T. Pattard, T. Pohl, and J. M. Rost, "Ultracold neutral plasmas," *Physics Reports*, vol. 449, pp. 77–130, Sept. 2007.

[4] T. Ott and M. Bonitz, "Diffusion in a Strongly Coupled Magnetized Plasma," *Physical Review Letters*, vol. 107, p. 135003, Sept. 2011.

[5] S. D. Baalrud and J. Daligault, "Transport regimes spanning magnetization-coupling phase space," *Physical Review E*, vol. 96, p. 043202, Oct. 2017.

[6] S. D. Bergeson, S. D. Baalrud, C. L. Ellison, E. Grant, F. R. Graziani, T. C. Killian, M. S. Murillo, J. L. Roberts, and L. G. Stanton, "Exploring the crossover between high-energy-density plasma and ultracold neutral plasma physics," *Physics of Plasmas*, vol. 26, p. 100501, Oct. 2019. Publisher: American Institute of Physics.

[7] I. L. Isaev and A. P. Gavriliuk, "Interaction of ultracold non-ideal ion–electron

plasma with a uniform magnetic field," *Journal of Physics B: Atomic, Molecular and Optical Physics*, vol. 51, p. 025701, Jan. 2018.

[8] S. K. Tiwari and S. D. Baalrud, "Reduction of electron heating by magnetizing ultracold neutral plasma," *Physics of Plasmas*, vol. 25, p. 013511, Jan. 2018.

[9] E. Thomas, R. L. Merlino, and M. Rosenberg, "Magnetized dusty plasmas: the next frontier for complex plasma research," *Plasma Physics and Controlled Fusion*, vol. 54, p. 124034, Dec. 2012.

[10] V. Y. Karasev, E. S. Dzlieva, L. G. D'yachkov, L. A. Novikov, S. I. Pavlov, and S. A. Tarasov, "The effect of magnetic field on plasma particles in dusty plasma," *Contributions to Plasma Physics*, vol. 59, no. 4-5, p. e201800136, 2019. _eprint: https://onlinelibrary.wiley.com/doi/pdf/10.1002/ctpp.201800136.

[11] Y. Feng, S. Lu, K. Wang, W. Lin, and D. Huang, "Dynamics and transport of magnetized two-dimensional Yukawa liquids," *Reviews of Modern Plasma Physics*, vol. 3, p. 10, June 2019.

[12] Y. Shi, H. Qin, and N. J. Fisch, "Laser-plasma interactions in magnetized environment," *Physics of Plasmas*, vol. 25, p. 055706, Mar. 2018. Publisher: American Institute of Physics.

[13] J. J. Santos, M. Bailly-Grandvaux, M. Ehret, A. V. Arefiev, D. Batani, F. N. Beg, A. Calisti, S. Ferri, R. Florido, P. Forestier-Colleoni, S. Fujioka, M. A. Gigosos, L. Giuffrida, L. Gremillet, J. J. Honrubia, S. Kojima, P. Korneev, K. F. F. Law, J.-R. Marquès, A. Morace, C. Mossé, O. Peyrusse, S. Rose, M. Roth, S. Sakata, G. Schaumann, F. Suzuki-Vidal, V. T. Tikhonchuk, T. Toncian, N. Woolsey, and Z. Zhang, "Laser-driven strong magnetostatic fields with

applications to charged beam transport and magnetized high energy-density physics," *Physics of Plasmas*, vol. 25, p. 056705, May 2018. Publisher: American Institute of Physics.

[14] J. Hughto, A. S. Schneider, C. J. Horowitz, and D. K. Berry, "Diffusion of neon in white dwarf stars," *Physical Review E*, vol. 82, p. 066401, Dec. 2010.

[15] G. Valyavin, D. Shulyak, G. A. Wade, K. Antonyuk, S. V. Zharikov, G. A. Galazutdinov, S. Plachinda, S. Bagnulo, L. F. Machado, M. Alvarez, D. M. Clark, J. M. Lopez, D. Hiriart, I. Han, Y.-B. Jeon, C. Zurita, R. Mujica, T. Burlakova, T. Szeifert, and A. Burenkov, "Suppression of cooling by strong magnetic fields in white dwarf stars," *Nature*, vol. 515, pp. 88–91, Nov. 2014.

[16] F. Peng, E. F. Brown, and J. W. Truran, "Sedimentation and Type I X-Ray Bursts at Low Accretion Rates," *The Astrophysical Journal*, vol. 654, pp. 1022–1035, Jan. 2007.

[17] A. Y. Potekhin, J. A. Pons, and D. Page, "Neutron Stars—Cooling and Transport," *Space Science Reviews*, vol. 191, pp. 239–291, Oct. 2015.

[18] D. J. Bernstein, T. Lafleur, J. Daligault, and S. D. Baalrud, "Friction force in strongly magnetized plasmas," *Physical Review E*, vol. 102, p. 041201, Oct. 2020.

[19] K. R. Vidal and S. D. Baalrud, "Extended space and time correlations in strongly magnetized plasmas," *Physics of Plasmas*, vol. 28, p. 042103, Apr. 2021. Publisher: American Institute of Physics.

[20] S. D. Baalrud and J. Daligault, "Mean force kinetic theory: A convergent kinetic

theory for weakly and strongly coupled plasmas," *Physics of Plasmas*, vol. 26, p. 082106, Aug. 2019.

[21] L. Jose and S. D. Baalrud, "A generalized Boltzmann kinetic theory for strongly magnetized plasmas with application to friction," *Physics of Plasmas*, vol. 27, p. 112101, Nov. 2020.

[22] D. Ciampini, M. Anderlini, J. H. Müller, F. Fuso, O. Morsch, J. W. Thomsen, and E. Arimondo, "Photoionization of ultracold and Bose-Einstein-condensed Rb atoms," *Physical Review A*, vol. 66, p. 043409, Oct. 2002.

[23] D. Feldbaum, N. V. Morrow, S. K. Dutta, and G. Raithel, "Coulomb Expansion of Laser-Excited Ion Plasmas," *Physical Review Letters*, vol. 89, p. 173004, Oct. 2002.

[24] T. M. Wilson, W.-T. Chen, and J. L. Roberts, "Density-dependent response of an ultracold plasma to few-cycle radio-frequency pulses," *Physical Review A*, vol. 87, p. 013410, Jan. 2013.

[25] E. A. Cummings, J. E. Daily, D. S. Durfee, and S. D. Bergeson, "Fluorescence Measurements Of Expanding Strongly Coupled Neutral Plasmas," *Physical Review Letters*, vol. 95, p. 235001, Nov. 2005. Publisher: American Physical Society.

[26] T. Sprenkle, A. Dodson, Q. McKnight, R. Spencer, S. Bergeson, A. Diaw, and M. S. Murillo, "Ion friction at small values of the Coulomb logarithm," *Physical Review E*, vol. 99, p. 053206, May 2019.

[27] C. E. Simien, Y. C. Chen, P. Gupta, S. Laha, Y. N. Martinez, P. G. Mickelson, S. B. Nagel, and T. C. Killian, "Using Absorption Imaging to Study Ion

Dynamics in an Ultracold Neutral Plasma," *Physical Review Letters*, vol. 92, p. 143001, Apr. 2004.

[28] M. P. Robinson, B. L. Tolra, M. W. Noel, T. F. Gallagher, and P. Pillet, "Spontaneous Evolution of Rydberg Atoms into an Ultracold Plasma," *Physical Review Letters*, vol. 85, pp. 4466–4469, Nov. 2000.

[29] A. Walz-Flannigan, J. R. Guest, J.-H. Choi, and G. Raithel, "Cold-Rydberg-gas dynamics," *Physical Review A*, vol. 69, p. 063405, June 2004.

[30] E. V. Crockett, R. C. Newell, F. Robicheaux, and D. A. Tate, "Heating and cooling of electrons in an ultracold neutral plasma using Rydberg atoms," *Physical Review A*, vol. 98, p. 043431, Oct. 2018.

[31] J. P. Morrison, C. J. Rennick, J. S. Keller, and E. R. Grant, "Evolution from a Molecular Rydberg Gas to an Ultracold Plasma in a Seeded Supersonic Expansion of NO," *Physical Review Letters*, vol. 101, p. 205005, Nov. 2008.

[32] T. K. Langin, G. M. Gorman, and T. C. Killian, "Laser cooling of ions in a neutral plasma," *Science*, vol. 363, pp. 61–64, Jan. 2019. Publisher: American Association for the Advancement of Science Section: Report.

[33] J. Castro, H. Gao, and T. C. Killian, "Using sheet fluorescence to probe ion dynamics in an ultracold neutral plasma," *Plasma Physics and Controlled Fusion*, vol. 50, p. 124011, Dec. 2008.

[34] G. Bannasch, J. Castro, P. McQuillen, T. Pohl, and T. C. Killian, "Velocity Relaxation in a Strongly Coupled Plasma," *Physical Review Letters*, vol. 109, p. 185008, Nov. 2012. Publisher: American Physical Society.

[35] M. Lyon and S. L. Rolston, “Ultracold neutral plasmas,” *Reports on Progress in Physics*, vol. 80, p. 017001, Jan. 2017.

[36] T. Langin, *Laser Cooling of Ions in a Neutral Plasma.* PhD thesis, Rice University, Houston, TX, 2019.

[37] P. McQuillen, *High Resolution Measurement and Modeling of Ion Dynamics in an Ultracold Neutral Plasma.* PhD thesis, Rice University, Houston, TX, 2015.

[38] J. A. C. Nieto, *Collective effects in Ultracold Neutral Plasmas.* PhD thesis, Rice University, Houston, TX, 2011.

[39] S. Laha, P. Gupta, C. E. Simien, H. Gao, J. Castro, T. Pohl, and T. C. Killian, “Experimental Realization of an Exact Solution to the Vlasov Equations for an Expanding Plasma,” *Physical Review Letters*, vol. 99, p. 155001, Oct. 2007. Publisher: American Physical Society.

[40] M. K. Warrens, G. M. Gorman, S. J. Bradshaw, and T. C. Killian, “Expansion of ultracold neutral plasmas with exponentially decaying density distributions,” *Physics of Plasmas*, vol. 28, p. 022110, Feb. 2021.

[41] T. K. Langin, T. Strickler, N. Maksimovic, P. McQuillen, T. Pohl, D. Vrinceanu, and T. C. Killian, “Demonstrating universal scaling for dynamics of Yukawa one-component plasmas after an interaction quench,” *Physical Review E*, vol. 93, p. 023201, Feb. 2016.

[42] T. Pohl, D. Vrinceanu, and H. R. Sadeghpour, “Rydberg Atom Formation in Ultracold Plasmas: Small Energy Transfer with Large Consequences,” *Physical Review Letters*, vol. 100, p. 223201, June 2008.

[43] R. S. Fletcher, X. L. Zhang, and S. L. Rolston, "Using Three-Body Recombination to Extract Electron Temperatures of Ultracold Plasmas," *Physical Review Letters*, vol. 99, p. 145001, Oct. 2007.

[44] F. Robicheaux and J. D. Hanson, "Simulated expansion of an ultra-cold, neutral plasma," *Physics of Plasmas*, vol. 10, pp. 2217–2229, June 2003.

[45] D. Comparat, T. Vogt, N. Zahzam, M. Mudrich, and P. Pillet, "Star cluster dynamics in a laboratory: electrons in an ultracold plasma," *Monthly Notices of the Royal Astronomical Society*, vol. 361, pp. 1227–1242, Aug. 2005.

[46] S. Hamaguchi, R. T. Farouki, and D. H. E. Dubin, "Triple point of Yukawa systems," *Physical Review E*, vol. 56, pp. 4671–4682, Oct. 1997.

[47] S. Kulin, T. C. Killian, S. D. Bergeson, and S. L. Rolston, "Plasma Oscillations and Expansion of an Ultracold Neutral Plasma," *Physical Review Letters*, vol. 85, pp. 318–321, July 2000.

[48] T. Pohl, T. Pattard, and J. M. Rost, "Kinetic modeling and molecular dynamics simulation of ultracold neutral plasmas including ionic correlations," *Physical Review A*, vol. 70, p. 033416, Sept. 2004.

[49] P. McQuillen, T. Strickler, T. Langin, and T. C. Killian, "Ion temperature evolution in an ultracold neutral plasma," *Physics of Plasmas*, vol. 22, p. 033513, Mar. 2015.

[50] G. Gorman, M. Warrens, S. Bradshaw, and T. Killian, "Magnetic Confinement of an Ultracold Neutral Plasma," *Physical Review Letters*, vol. 126, p. 085002, Feb. 2021.

[51] O. Vaulina, S. Khrapak, and G. Morfill, "Universal scaling in complex (dusty) plasmas," *Physical Review E*, vol. 66, p. 016404, July 2002.

[52] M. Lyon, S. D. Bergeson, and M. S. Murillo, "Limit of strong ion coupling due to electron shielding," *Physical Review E*, vol. 87, p. 033101, Mar. 2013.

[53] V. S. Dharodi and M. S. Murillo, "Sculpted ultracold neutral plasmas," *Physical Review E*, vol. 101, p. 023207, Feb. 2020.

[54] P. McQuillen, J. Castro, T. Strickler, S. J. Bradshaw, and T. C. Killian, "Ion holes in the hydrodynamic regime in ultracold neutral plasmas," *Physics of Plasmas*, vol. 20, p. 043516, Apr. 2013.

[55] P. McQuillen, J. Castro, S. J. Bradshaw, and T. C. Killian, "Emergence of kinetic behavior in streaming ultracold neutral plasmas," *Physics of Plasmas*, vol. 22, p. 043514, Apr. 2015. Publisher: American Institute of Physics.

[56] J. Sous and E. Grant, "Possible Many-Body Localization in a Long-Lived Finite-Temperature Ultracold Quasineutral Molecular Plasma," *Physical Review Letters*, vol. 120, p. 110601, Mar. 2018.

[57] G. M. Gorman, T. K. Langin, M. K. Warrens, D. Vrinceanu, and T. C. Killian, "Combined molecular-dynamics and quantum-trajectories simulation of laser-driven, collisional systems," *Physical Review A*, vol. 101, p. 012710, Jan. 2020. Publisher: American Physical Society.

[58] P. McQuillen, J. Castro, and T. C. Killian, "High-resolution ionization of ultracold neutral plasmas," *Journal of Physics B: Atomic, Molecular and Optical Physics*, vol. 44, p. 184013, Sept. 2011.

[59] J. Castro, P. McQuillen, and T. C. Killian, “Ion Acoustic Waves in Ultracold Neutral Plasmas,” *Physical Review Letters*, vol. 105, p. 065004, Aug. 2010.

[60] T. C. Killian, P. McQuillen, T. M. O’Neil, and J. Castro, “Creating and studying ion acoustic waves in ultracold neutral plasmas,” *Physics of Plasmas*, vol. 19, p. 055701, Mar. 2012. Publisher: American Institute of Physics.

[61] J. Castro, G. Bannasch, P. McQuillen, T. Pohl, T. C. Killian, P. K. Shukla, J. T. Mendonça, B. Eliasson, and D. Resedes, “Creating non-Maxwellian velocity distributions in ultracold plasmas,” pp. 31–43, 2012.

[62] T. Strickler, T. Langin, P. McQuillen, J. Daligault, and T. Killian, “Experimental Measurement of Self-Diffusion in a Strongly Coupled Plasma,” *Physical Review X*, vol. 6, p. 021021, May 2016. Publisher: American Physical Society.

[63] J. Daligault and S. D. Baalrud, “Plasma transport theory spanning weak to strong coupling,” (Takamatsu, Japan), p. 040002, 2015.

[64] S. D. Baalrud and J. Daligault, “Effective potential kinetic theory for strongly coupled plasmas,” (Victoria, BC, Canada), p. 130001, 2016.

[65] S. D. Baalrud and J. Daligault, “Extending plasma transport theory to strong coupling through the concept of an effective interaction potential,” *Physics of Plasmas*, vol. 21, p. 055707, May 2014.

[66] J.-P. Hansen and I. McDonald, “Theory of Simple Liquids - 3rd Edition,” 2006.

[67] M. E. Glinsky and T. M. O’Neil, “Guiding center atoms: Three-body recombination in a strongly magnetized plasma,” *Physics of Fluids B: Plasma Physics*, vol. 3, pp. 1279–1293, May 1991.

[68] X. L. Zhang, R. S. Fletcher, S. L. Rolston, P. N. Guzdar, and M. Swisdak, "Ultracold Plasma Expansion in a Magnetic Field," *Physical Review Letters*, vol. 100, p. 235002, June 2008.

[69] J. Simpson, J. Lane, C. Immer, and R. Youngquist, "Simple Analytic Expressions for the Magnetic Field of a Circular Current Loop," 2001.

[70] H. J. Metcalf and P. van der Straten, "Laser Cooling and Trapping of Neutral Atoms," in *The Optics Encyclopedia*, American Cancer Society, 2007. _eprint: https://onlinelibrary.wiley.com/doi/pdf/10.1002/9783527600441.oe005.

[71] S. B. Nagel, C. E. Simien, S. Laha, P. Gupta, V. S. Ashoka, and T. C. Killian, "Magnetic trapping of metastable 3 P 2 atomic strontium," *Physical Review A*, vol. 67, p. 011401, Jan. 2003.

[72] K. J. Weatherill, J. D. Pritchard, P. F. Griffin, U. Dammalapati, C. S. Adams, and E. Riis, "A versatile and reliably reusable ultrahigh vacuum viewport," *Review of Scientific Instruments*, vol. 80, p. 026105, Feb. 2009.

[73] J. E. Sansonetti and G. Nave, "Wavelengths, Transition Probabilities, and Energy Levels for the Spectrum of Neutral Strontium (SrI)," *Journal of Physical and Chemical Reference Data*, vol. 39, p. 033103, Sept. 2010.

[74] H. Salami and A. J. Ross, "A molecular iodine atlas in ascii format," *Journal of Molecular Spectroscopy*, vol. 233, pp. 157–159, Sept. 2005.

[75] T. Nakajima and N. Yonekura, "Electron spin-polarized alkaline-earth ions produced by multiphoton ionization," *The Journal of Chemical Physics*, vol. 117, pp. 2112–2119, Aug. 2002.

[76] N. Yonekura, T. Nakajima, Y. Matsuo, T. Kobayashi, and Y. Fukuyama, “Electron-spin polarization of photoions produced through photoionization from the laser-excited triplet state of Sr,” *The Journal of Chemical Physics*, vol. 120, pp. 1806–1812, Jan. 2004.

[77] R. McWilliams and D. Edrich, “Laser-induced fluorescence diagnosis of plasma processing sources,” *Thin Solid Films*, vol. 435, pp. 1–4, July 2003.

[78] R. M. Magee, M. E. Galante, D. McCarren, E. E. Scime, R. L. Boivin, N. H. Brooks, R. J. Groebner, D. N. Hill, and G. D. Porter, “A two photon absorption laser induced fluorescence diagnostic for fusion plasmas,” *Review of Scientific Instruments*, vol. 83, p. 10D701, Oct. 2012.

[79] M. Krychowiak, P. Mertens, R. König, B. Schweer, S. Brezinsek, O. Schmitz, M. Brix, U. Samm, and T. Klinger, “LIF measurements on an atomic helium beam in the edge of a fusion plasma,” *Plasma Physics and Controlled Fusion*, vol. 50, p. 065015, June 2008.

[80] K. Muraoka and M. Maeda, “Application of laser-induced fluorescence to high-temperature plasmas,” *Plasma Physics and Controlled Fusion*, vol. 35, pp. 633–656, June 1993.

[81] R. F. Boivin and E. E. Scime, “Laser induced fluorescence in Ar and He plasmas with a tunable diode laser,” *Review of Scientific Instruments*, vol. 74, pp. 4352–4360, Oct. 2003.

[82] M. J. Goeckner, J. Goree, and T. E. Sheridan, “Laser-induced fluorescence characterization of ions in a magnetron plasma,” *Journal of Vacuum Science & Technology A: Vacuum, Surfaces, and Films*, vol. 8, pp. 3920–3924, Nov. 1990.

[83] F. Anderegg, X.-P. Huang, E. Sarid, and C. F. Driscoll, “A new pure ion plasma device with laser induced fluorescence diagnostic,” *Review of Scientific Instruments*, vol. 68, pp. 2367–2377, June 1997.

[84] R. S. Marshall and P. M. Bellan, “Laser-induced fluorescence measurement of very slow neutral flows in a dusty plasma experiment,” *Review of Scientific Instruments*, vol. 91, p. 063504, June 2020.

[85] T. Miksch and A. Melzer, “Fluorescent microspheres as tracer particles in dusty plasmas,” *Physical Review E*, vol. 75, p. 016404, Jan. 2007.

[86] G. M. Gorman, M. K. Warrens, S. J. Bradshaw, and T. C. Killian, “Laser-induced-fluorescence imaging of a spin-polarized ultracold neutral plasma in a magnetic field,” *Physical Review A*, vol. 105, p. 013108, Jan. 2022.

[87] J. E. Sansonetti, “Wavelengths, Transition Probabilities, and Energy Levels for the Spectra of Strontium Ions (Sr II through Sr XXXVIII),” *Journal of Physical and Chemical Reference Data*, vol. 41, pp. 013102–013102–119, Mar. 2012.

[88] P. Dirac, “The quantum theory of the emission and absorption of radiation,” vol. A114, no. 767, pp. 243–265, 1927.

[89] V. Weisskopf and E. Wigner, “Berechnung der nati˜rlichen Linienbreite auf Grund der Dirac schen Lichttheorie*,” vol. 63, pp. 54–73, 1930.

[90] C. J. Foot, *Atomic physics*. No. 7. Atomic, Optical, and laser physics in Oxford master series in physics, Oxford ; New York: Oxford University Press, 2005. OCLC: ocm57478010.

[91] B. E. King, “Angular Momentum Coupling and Rabi Frequencies for Simple Atomic Transitions,” *arXiv:0804.4528 [physics]*, Apr. 2008. arXiv: 0804.4528.

[92] J. J. Sakurai and J. Napolitano, *Modern quantum mechanics.* Boston: Addison-Wesley, 2nd ed ed., 2011.

[93] X. Li and H. F. Arnoldus, “Propagation of Electric Dipole Radiation through a Medium,” *ISRN Optics*, vol. 2012, pp. 1–7, Nov. 2012.

[94] D. A. Steck, *Quantum and Atom Optics.* 2021. Available online at http://steck.us/teaching revision 0.13.10.

[95] G. Dimonte and J. Daligault, “Molecular-Dynamics Simulations of Electron-Ion Temperature Relaxation in a Classical Coulomb Plasma,” *Physical Review Letters*, vol. 101, p. 135001, Sept. 2008.

[96] G. M. Gorman, “KillianRice/plasma-spectrum-model: LIF of Magnetized UCNP,” Dec. 2021. (Version v1.0), Zenodo, http://doi.org/10.5281/zenodo.5792367.

[97] J. Berkowitz, K. O. Friedrichs, H. Goertzel, H. Grad, J. Killeen, and E. Rubin, “Proceedings of the 2nd United Nations International Conference on the Peaceful Uses of Atomic Energy, held in Geneva, 1 September- 13 September 1958.,” vol. 31, p. 171, UN,, 1958.

[98] I. Spalding, *Advances in Plasma Physics*, vol. 4. New York: Ed. by A. Simon and W. B. Thompson. Interscience, 1971.

[99] R. F. Post, R. E. Ellis, F. C. Ford, and M. N. Rosenbluth, “Stable Confinement of A High-Temperature Plasma,” *Physical Review Letters*, vol. 4, pp. 166–170,

Feb. 1960.

[100] M. Haines, “Plasma containment in cusp-shaped magnetic fields,” *Nuclear Fusion*, vol. 17, pp. 811–858, Aug. 1977.

[101] A. Kitsunezaki, “Cusp confinement of high-beta plasmas produced by a laser pulse from a freely-falling deuterium ice pellet,” *Physics of Fluids*, vol. 17, no. 10, p. 1895, 1974.

[102] K. N. Leung, N. Hershkowitz, and K. R. MacKenzie, “Plasma confinement by localized cusps,” *Physics of Fluids*, vol. 19, no. 7, p. 1045, 1976.

[103] M. Carr, D. Gummersall, S. Cornish, and J. Khachan, “Low beta confinement in a Polywell modelled with conventional point cusp theories,” *Physics of Plasmas*, vol. 18, p. 112501, Nov. 2011.

[104] C. M. Cooper, D. B. Weisberg, I. Khalzov, J. Milhone, K. Flanagan, E. Peterson, C. Wahl, and C. B. Forest, “Direct measurement of the plasma loss width in an optimized, high ionization fraction, magnetic multi-dipole ring cusp,” *Physics of Plasmas*, vol. 23, p. 102505, Oct. 2016.

[105] A. A. Hubble, E. V. Barnat, B. R. Weatherford, and J. E. Foster, “The electron spatial distribution and leak width in a magnetic cusp,” *Plasma Sources Science and Technology*, vol. 23, p. 022001, Feb. 2014.

[106] C. Russell, “The solar wind interaction with the Earth’s magnetosphere: a tutorial,” *IEEE Transactions on Plasma Science*, vol. 28, pp. 1818–1830, Dec. 2000. Conference Name: IEEE Transactions on Plasma Science.

[107] S. Ichimaru, “Strongly coupled plasmas: high-density classical plasmas and degenerate electron liquids,” *Reviews of Modern Physics*, vol. 54, pp. 1017–1059, Oct. 1982.

[108] S. G. Kuzmin and T. M. O’Neil, “Numerical simulation of ultracold plasmas,” *Physics of Plasmas*, vol. 9, pp. 3743–3751, Sept. 2002. Publisher: American Institute of Physics.

[109] S. Mazevet, L. A. Collins, and J. D. Kress, “Evolution of Ultracold Neutral Plasmas,” *Physical Review Letters*, vol. 88, p. 055001, Jan. 2002. Publisher: American Physical Society.

[110] F. Robicheaux and J. D. Hanson, “Simulation of the Expansion of an Ultracold Neutral Plasma,” *Physical Review Letters*, vol. 88, p. 055002, Jan. 2002. Publisher: American Physical Society.

[111] P. Gupta, S. Laha, C. E. Simien, H. Gao, J. Castro, T. C. Killian, and T. Pohl, “Electron-Temperature Evolution in Expanding Ultracold Neutral Plasmas,” *Physical Review Letters*, vol. 99, p. 075005, Aug. 2007. Publisher: American Physical Society.

[112] W.-T. Chen, C. Witte, and J. L. Roberts, “Observation of a strong-coupling effect on electron-ion collisions in ultracold plasmas,” *Physical Review E*, vol. 96, p. 013203, July 2017.

[113] M. A. Lieberman, *Principles of Plasma Discharges and Materials Processing.* John Wiley and Sons, Inc., 2005.

[114] R. A. Bosch and R. L. Merlino, “Confinement properties of a low-beta discharge

in a spindle cusp magnetic field," *The Physics of Fluids*, vol. 29, pp. 1998–2006, June 1986. Publisher: American Institute of Physics.